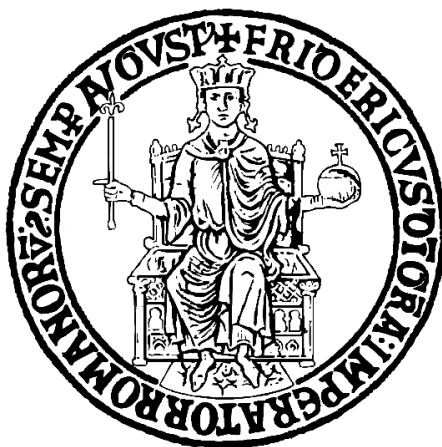


Università degli Studi di Napoli “Federico II”



SCUOLA POLITECNICA E DELLE SCIENZE DI BASE

DIPARTIMENTO DI INGEGNERIA INDUSTRIALE

DOCTORAL PROGRAMME IN INDUSTRIAL ENGINEERING

DISTRIBUTED ELECTRO-MECHANICAL ACTUATION AND SENSING SYSTEM DESIGN FOR MORPHING STRUCTURES

Doctoral Dissertation of:
Maurizio Arena

Supervisors:

Prof. Leonardo Lecce
Prof. Francesco Marulo
Prof. Rosario Pecora
Prof. Francesco Amoroso

External Tutor:

Prof. Michele Meo

The Chair of the Doctoral Program:

Prof. Michele Grassi

Academic year 2017/2018 – XXXI cycle

Contents

<i>Foreword</i>	4
1. Introduction to Smart Systems	6
<i>What does mean Smart System?</i>	6
<i>The Biomimetic wing concept</i>	7
<i>Actuation and Sensing Integrated Systems</i>	9
<i>Towards the ready-to-fly Intelligent Systems</i>	12
<i>Aims of the Thesis</i>	14
References	16
Awards	17
2. Dynamic Modelling of Electro-Mechanical Actuation	18
2.1 Framework	18
2.2 Reference Aileron System	19
2.3 Finite Element Model description	22
2.4 Experimental activities	24
2.4.1 Functionality tests	25
2.4.2 Ground Resonance Test and FE updating	26
2.5 Actuation performance in Wind Tunnel Test	36
2.6 Conclusions	38
Acknowledgments	38
References	38
3. Aero-Servo-Elasticity of Electro-Actuated Morphing devices	40
3.1 Introduction	40
3.2 Model Condensation	41
3.3 Aeroelastic Model	43
3.4 Aero-Servo-Elastic stability analysis	46
3.4.1 Anti-symmetric aeroelastic analysis	47
3.4.2 Symmetric aeroelastic analysis	49
3.5 Conclusions	53
Acknowledgments	55
References	55
4. Electro-Actuation System Strategy for a Morphing Flap	58
4.1 Clean Sky Challenge: JTI and Airgreen 2 frameworks	58
4.2 Robotized system architecture	60
4.2.1 Mechanical constraints	60

4.2.2	Actuation design	62
4.3	Morphing flap overview	65
4.3.1	Target shapes and specifications	65
4.4	Control Logic Strategy and Lab test on Iron Bird	66
4.4.1	System arrangement	66
4.5	Towards a Multi-Modal Morphing Flap: Clean Sky 2 upgrade	73
4.5.1	Design Loads	75
4.5.2	Actuation Concept Layout and Control Scheme	76
4.5.3	Compatibility with other electric devices	82
4.6	Conclusions and next activities	88
	References	88
5.	Self-sensing System for Compliant Morphing Tab	92
5.1	Research scenario	92
5.2	Materials and methods	94
5.3	Characterization of self-sensing resin	94
5.4	Integrated self-sensing coating	100
5.5	Conclusions and outlooks	104
	Acknowledgments	104
	References	104
	<i>Afterword</i>	108

Foreword

Smart structures, able to sense changes of their own state or variations of the environment they're in, and capable of intervening in order to improve their performance, find themselves in an ever-increasing use among numerous technology fields, opening new frontiers within advanced structural engineering and materials science. Smart structures represent of course a current challenge for the application on the aircrafts. A morphing structure can be considered as the result of the synergic integration of three main systems: the structural system, based on reliable kinematic mechanisms or on compliant elements enabling the shape modification, the actuation and control systems, characterized by embedded actuators and robust control strategies, and the sensing system, usually involving a network of sensors distributed along the structure to monitor its state parameters. Technologies with ever increasing maturity level are adopted to assure the consolidation of products in line with the aeronautical industry standards and fully compliant with the applicable airworthiness requirements. Until few years ago, morphing wing technology appeared an utopic solution. In the aeronautical field, airworthiness authorities demand a huge process of qualification, standardization, and verification. Essential components of an intelligent structure are sensors and actuators. The actual technological challenge, envisaged in the industrial scenario of "more electric aircraft", will be to replace the heavy conventional hydraulic actuators with a distributed strategy comprising smaller electro-mechanical actuators. This will bring several benefit at the aircraft level: firstly, fuel savings. Additionally, a full electrical system reduces classical drawbacks of hydraulic systems and overall complexity, yielding also weight and maintenance benefits. At the same time, a morphing structure needs a real-time strain monitoring system: a nano-engineered polymer capable of densely distributed strain sensing can be a suitable solution for this kind of flying systems. Piezoresistive carbon nanotubes can be integrated as thin films coated and integrated with composite to form deformable self-sensing materials. The materials actually become sensors themselves without using external devices, embedded or attached.

This doctoral thesis proposes a multi-disciplinary investigation of the most modern actuation and sensing technologies for variable-shaped devices mainly intended for large commercial aircraft. The personal involvement in several research projects with numerous international partners - during the last three years - allowed for exploiting engineering outcomes in view of potential certification and industrialization of the studied solutions. Moving from a conceptual survey of the smart systems that introduces the idea of adaptive aerodynamic surfaces and main research challenges, the thesis presents (Chapter 1) the current worldwide status of morphing technologies as well as industrial development expectations. The Ph.D. programme falls within the design of some of the most promising and potentially flyable solutions for performance improvement of green regional aircrafts. A camber-morphing aileron and a multi-modal flap are herein analysed and assessed as subcomponents involved for the realization of a morphing wing.

An innovative camber-morphing aileron was proposed in CRIAQ MD0-505, a joint Canadian and Italian research project. Relying upon the experimental evidence within the present research, the issue appeared concerns the critical importance of considering the dynamic modelling of the actuators in the design phase of a smart device. The higher number of actuators involved makes de facto the morphing structure much more complex. In this context (Chapter 2), the action of the actuators has been modelled within the numerical model of the aileron: the comparison between the modal characteristics of numerical predictions and testing activities has shown a high level of correlation.

Morphing structures are characterized by many more degrees of freedom and increased modal density, introducing new paradigms about modelling strategies and aeroelastic approaches. These aspects affect and modify many aspects of the traditional aeronautical engineering process, like simulation activity, design criteria assessment, and interpretation of the dynamic response (Chapter 3). With respect the aforementioned aileron, sensitivity studies were carried out in compliance with EASA airworthiness requirements to evaluate the aero-servo-elastic stability of global system with respect to single and combined failures of the actuators enabling morphing. Moreover, the jamming event, which is one of the

main drawbacks associated with the use of electro-mechanical actuators, has been duly analyzed to observe any dynamic criticalities. Fault & Hazard Analysis (FHA) have been therefore performed as the basis for application of these devices to real aircraft.

Nevertheless, the implementation of an electro-mechanical system implies several challenges related to the integration at aircraft system level: the practical need for real-time monitoring of morphing devices, power absorption levels and dynamic performance under aircraft operating conditions, suggest the use of a ground-based engineering tool, i.e. “iron bird”, for the physical integration of systems. Looking in this perspective, the Chapter 4 deals with the description of an innovative multi-modal flap idealized in the Clean Sky - Joint Technology Initiative research scenario. A distributed gear-drive electro-mechanical actuation has been fully studied and validated by an experimental campaign. Relying upon the experience gained, the encouraging outcomes led to the second stage of the project, Clean Sky 2 - Airgreen 2, encompassing the development of a more robotized flap for next regional aircraft. Numerical and experimental activities have been carried out to support the health management process in order to check the EMAs compatibility with other electrical systems too.

A smart structure as a morphing wing needs an embedded sensing system in order to measure the actual deformation state as well as to “monitor” the structural conditions. A new possible approach in order to have a distributed light-weight system consists in the development of polymer-based materials filled with conductive smart fillers such as carbon nanotubes (CNTs). The thesis ends with a feasibility study about the incorporation of carbon nanomaterials into flexible coatings for composite structures (Chapter 5). Coupons made of MWCNTs embedded in typical aeronautic epoxy formulation were prepared and tested under different conditions in order to better characterize their sensing performance. Strain sensing properties were compared to commercially available strain gages and fiber optics. The results were obtained in the last training year following the involvement of the author in research activities at the University of Salerno and Materials and Structures Centre - University of Bath.

One of the issues for the next developments is to consolidate these novel technologies in the current and future European projects where the smart structures topic is considered as one of the priorities for the new generation aircrafts. It is remarkable that scientists and aeronautical engineers community does not stop trying to create an intelligent machine that is increasingly inspired by nature. The spirit of research, the desire to overcome limits and a little bit of imagination are surely the elements that can guide in achieving such an ambitious goal.

1. Introduction to Smart Systems

What does mean smart system?

A structure is smart if it is able to modify its characteristics, adapting itself to the external conditions in which it operates. The term "Intelligent Structure" derives from the idea of integrating active elements into the structure, thanks also to the development of innovative materials, and began to materialize starting from the 90s with the significant scientific activity carried out by researchers such as Crawley, de Luis, Wada and Fanson, [1-2]. It is therefore necessary to monitor the instantaneous "state" variables of the system so that its response can be controlled accordingly: this capability can be implemented by combining a sensory network and actuators, implemented with the minimum level of invasiveness. This last requirement stimulates the search for increasingly advanced structural design concepts based on the "embedded system" design logic, able to manage the infinite degrees of freedom of real structures with the lowest possible number of transducers. Sun J. *et al.* proposes in [3] a recent review a logical scheme which well describes the smart system concept, Figure 1.1. Smart materials and structures can obtain information from the environment around the skin (*sensing*), they then produce an internal chemical or physical effect delivered to the brain for decision making (*control*), and finally, they implement actions through the muscles (*actuation*). The information passes through the nerves, and each part is linked by tendons and fibrous bands (*skeletons*).

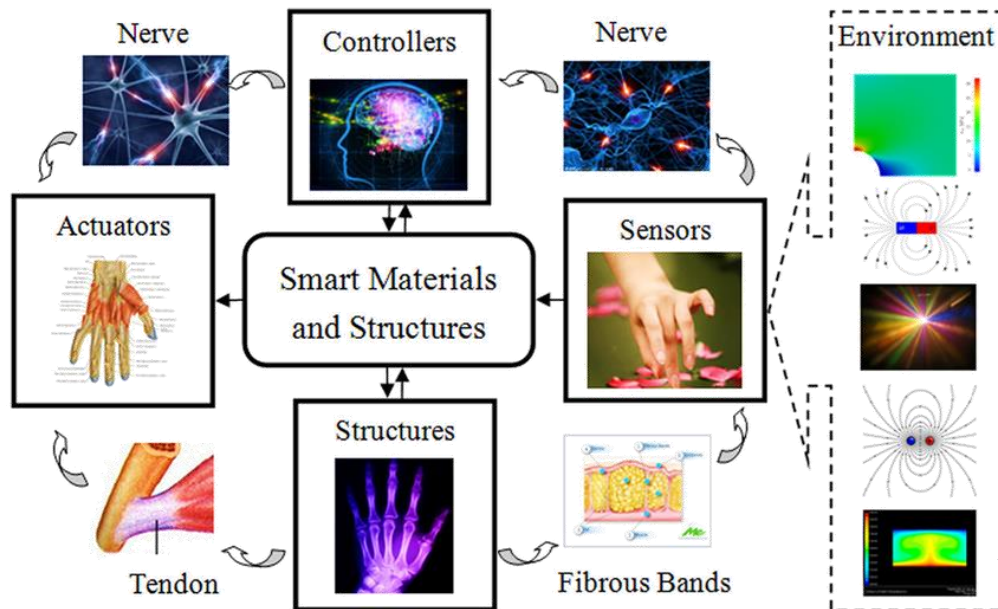


Figure 1.1. Synoptic layout of the smart structures and materials, [3].

An interesting exposition on the field of smart materials and structures dates back to the 90s thanks to Thompson B.S., Gandhi M.V. and Kasiviswanathan S.. The salient features of this biomimetic eclectic discipline have been highlighted outlining the ramifications on real engineering applications, [4]. Smart structures have demonstrated a broad range of potential applications for performance enhancement of the aerospace industry. Several research and practical applications projects conducted by government agencies, aerospace industries, and universities addressing numerous target applications such as flutter suppression, buffet control, vibro-acoustic control, adaptive structures and self-sensing systems, [5]. The Airbus airframe development strategy is based on the "Airbus Intelligent Airframe" approach, which targets on development and implementation of intelligent solutions and smart structures with intelligent characteristics, Figure 1.2. When evaluating the potential of new structural solutions and new technologies, Airbus has both in mind: the benefit in upgrading existing models and new programmes, [6-7].

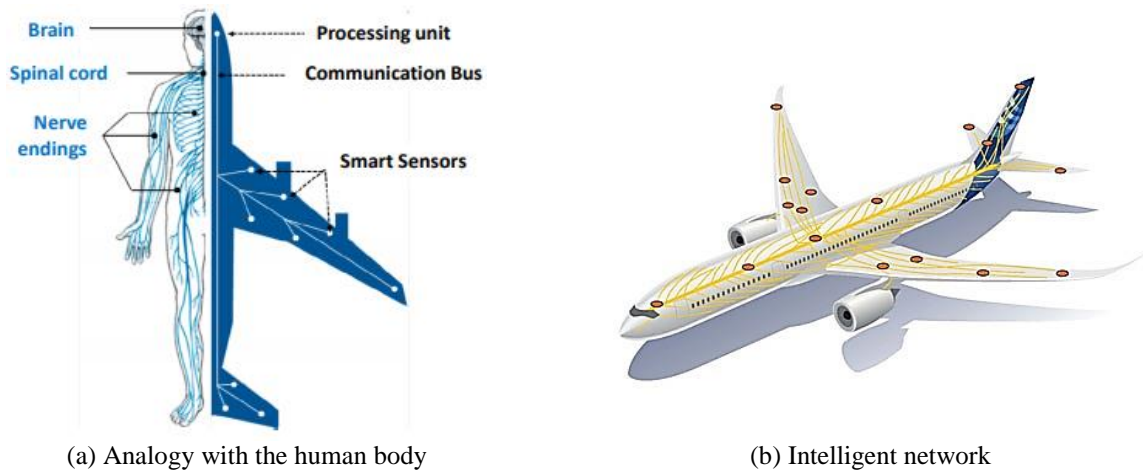


Figure 1.2. Airbus challenges: human nervous system based intelligent airframe.

The biomimetic wing concept

Nature is surely the most striking example for the design of a more fascinating idea: in the aeronautical and aerospace scenario, the emulation of the birds' flight is the true challenge of a morphing wing, Figure 1.3. Morph is a word descending from ancient Greek, *μορφή* or "morfé," and indicates shape, figure, or other synonyms, [8]. Therefore, morphing is something related to shaping, the modification of the original aspect of a certain entity. The integration of increasingly innovative technologies as reliable kinematic mechanisms, embedded servo-actuation and smart materials systems, are designed in order to assure new devices, fully compatible with the more and more stringent airworthiness requirements. Over the next few years the aviation industry will face the challenge to develop a new generation of air vehicles characterised by high aerodynamic efficiency and low environmental impact; still, the technologies currently available are inadequate to meet the demanding performance requirements and to comply with the stringent regulations in terms of polluting emissions: each of these reasons could suggest to a company to replace its fleet with new aircrafts. Next generation aircraft requires wings able to reconfigure their self in multiple shapes, in order to be optimal in every specific flight condition and reduce the waste of fuel resulting from a not commensurate flight dynamic.



Figure 1.3. Natural shaping control: flexible variable camber bird wing.

Looking at a generic aircraft morphing architecture, whether designed or realized, it is easy to imagine that the natural evolution of these systems is to expand the deformability regions and increase the macroscopic degrees of freedom of the reference structure. It could be stated that this tendency aims at emulating biological flight (like the bird one) more and more, even trying to move beyond that boundary. From these considerations, aircraft morphing systems can be classified as real Smart Structures as well as suitable candidates as part of a new category of robots, [9]. A robot is a mechanical or virtual artificial agent, as an electro-mechanical machine, driven through the support of devoted computer codes or electronic circuitry. The word is derived from the Czech “robota”, meaning heavy duty, in turn descended from the ecclesiastic Slavic “rabota” meaning servitude or servants. Exoskeletons or anthropomorphic autonomous or remote driven mechanical systems are classical examples of robots. Computer systems should be included in this definition as main elements of the control and sensor systems, including associated data processing and information feedback. Indeed, standard drones, currently available on the mass market, are basic examples of robots. In the actual opinion, morphing systems are to evolve towards machines capable of multiple degrees of freedom that can resemble the behaviour of living flying animals (ornitomorphic), as they move to higher, complex levels. The fact that these systems could be conceived for low to high speeds up to super and hypersonic velocities as well as for space missions, makes the future very close to science fiction. On the other hand, some prototypic versions of these concepts are already available, while a lot of movies try to envision far more prospects. The control systems should govern the behaviour of this futuristic machine, preventing general instabilities or strain excess, while an autonomous system or a human pilot drives it at a macroscopic level. In detail, these innovative concepts are applied to wings, enabling limited changes of their geometry and preserving their capability to bear external and internal loads, Figure 1.4.

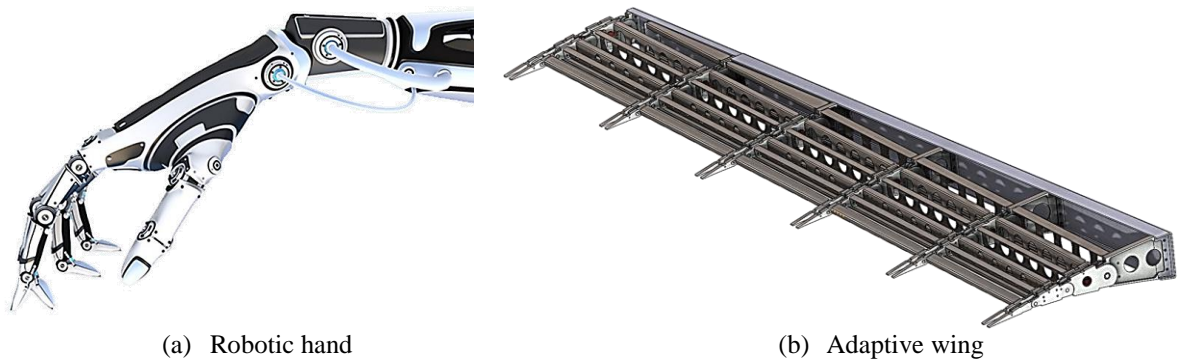


Figure 1.4. Smart Intelligent Structures: cybernetic analogy.

Smart Intelligent Structures may be introduced if the former concept is combined with recent achievements in information technology, signal processing, and cybernetics. A classical definition of cybernetics comes from N. Wiener, that explained the terms as the “scientific study of control and communication in the animal and the machine” (1948), [10]. The etymology of the word comes from Greek *κυβερνητική* (kybernetike), meaning governance or guidance. It may be seen as an interdisciplinary matter that links together control systems, electronics and electronic networks, informatics, neuroscience, logics, evolutionary biology and psychology, both human and animal. Autonomous decision-making and experience-based learning capabilities are traditionally linked to the development of information data processing and management systems that are at the base of biomimetic robot intelligence, [11]. Analogously, robotics is the fusion of some specialized mechanic, materials, electric, electronic, systems, and information engineering technology branches, dealing with the design, construction, operation, and application of robots, [12]. The morphing system should be able to deform itself, as it is sufficiently rigid to resist the action of several forces. Of course, these general principles can be specialized in many ways when the real application occurs. A typical scheme of a morphing system may be seen in Figure 1.5, where the main elements are reported with their logical collocation and links.

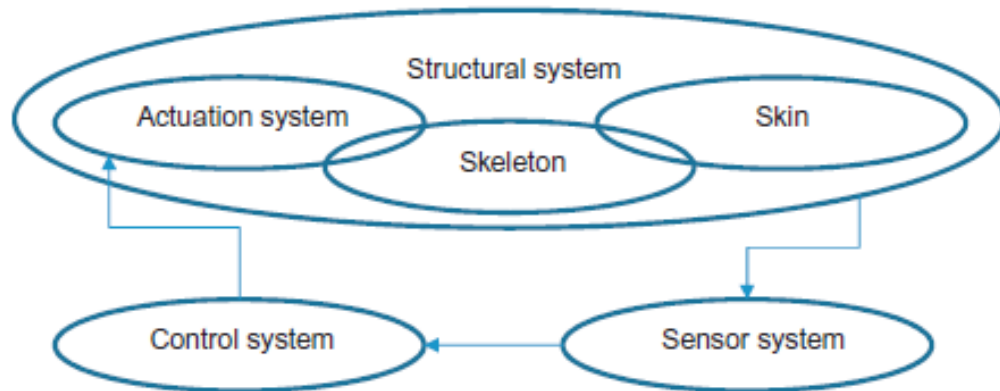


Figure 1.5. Core components of an adaptive system.

Actuation and sensing integrated systems

A biomimetic system is then imagined, commanded by an artificial or a natural intelligence. These are defined as integrated load-bearing architectures that can adapt themselves to variations of external environments, enlarging their operational domain while maintaining optimal performance levels. Adjustments follow mutated needs and try to maintain the structure into the best possible configuration while new occurrences arise and evolve with time. Such structural systems exhibit additional DOF that allows continuous transformation. Their design does not refer to a single reference point but to an extended domain. Structural kinematic adaptive systems bring important deals with respect to safety, [13]. First of all, because of the higher number of parts, the probability of failure increases for a complex system. A key point is then the capability of reducing the number of parts, classically a good index of the system fragility (or, on the contrary, its inverse is a good measure of the system robustness). Classical kinematic solutions are therefore consolidated on one side and are complex on the other. Fully compliant systems are instead structural components, forced to continuous deformation along an established path by relatively simple actuation architectures.

This philosophy was addressed by the joint teams of Flexsys, NASA, and Gulfstream. It has shown its major disadvantage in being strongly exposed to very severe aeroelastic behaviour by increasing its eigenmodes, [14]. It should also be added that mechanical devices are more rigid and their behaviour is better known in literature and in the aeronautical field, as a simple evolution of the flap, aileron, slat, etc. It is also worthwhile to discuss mass contribution. In principle, it shall be higher for kinematic chains than compliant structures. Still in this condition, the modal density is expected to be larger for the latter than the former, meaning very low rigidity levels for those architectures. This can also be an issue for the static response. Motors themselves are worth some dedicated statements. A kinematic actuation requires distributed active devices to achieve the required performance. A compliant architecture could rely on a smaller number of actuators because the driven structure is conceived as a continuous system. Please note that, the larger the actuators number, generally, the higher the stiffness. Now, from the point of view of maintenance, costs, operability, and hazards, the larger the number of motors, the higher the risk of failure, and the higher the complete system price. It should be added that a system with many devices can sometimes be attributed with a certain level of redundancy and safety (as each component is less significant with respect to the whole).

In any case, the reduction of the installed motors may be a design indication for the future. Generally, from the certification point of view, a kinematic system is more acceptable than a compliant system because it derives from very large experience on similar architectures. In other words, it is already in the *forma mentis* of the engineers and regulation public officers. Compliant systems have a long way to go before they can be fully accepted. Figure 1.6 shows a practical comparison between the aircraft torque shaft configuration and a distributed actuation arrangement suitable for a morphing trailing edge device.

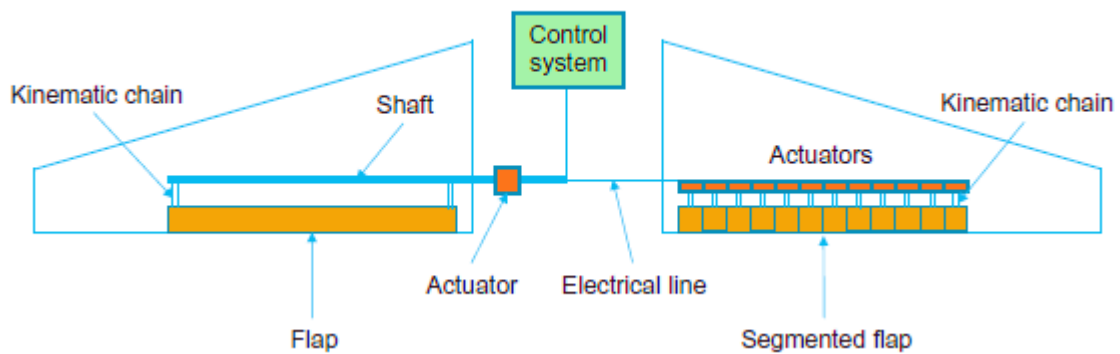


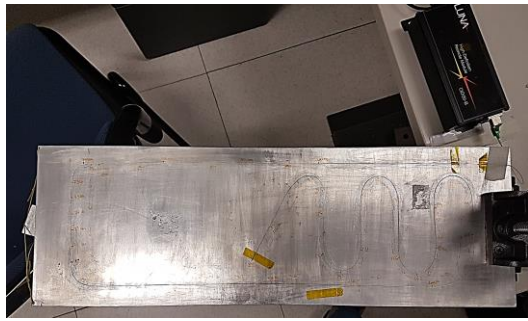
Figure 1.6. Comparison between distributed and concentrated actuation concept.

In the shafted configuration, all actuators are mechanically linked by the torque shaft controlled by the power distribution unit whereas in a distributed arrangement, no more torque shaft is needed. However, the implementation of an electrical system implies many challenges related to the integration at aircraft system level. In particular, it must be demonstrated their reliability in harsh environment, moreover their safety and types of failures with an aim to reconfiguration enhancement.

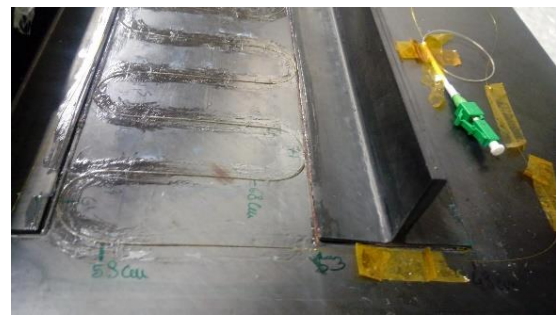
Driven by the demand to optimize aircraft performance, decrease operating and maintenance costs, increase dispatch reliability, and reduce gas emissions - have underscored the aircraft industry's renewed push toward the concept of more electric aircraft (MEA), and ultimately an all-electric aircraft.

Specifically, the MEA concept provides for the utilization of electric power for all non-propulsive systems. Traditionally these non-propulsive systems are driven by a combination of different secondary power sources such as hydraulic, pneumatic, mechanical and electrical. Recent technological advances in the field of power electronics, fault-tolerant architecture, electro-hydrostatic actuators, flight control systems, high density electric motors, power generation and conversion systems have ushered the era of the MEA. This trend is accelerating, as aircraft OEMs collaborate with their suppliers to design new systems and implement new electrical-intensive architectures. Adoption of the MEA concept is seen as critical enabler for the aircraft industry to unlock significant improvements in terms of aircraft weight, fuel consumption, total life cycle costs, maintainability and aircraft reliability. An advanced high lift actuation system architecture with distributed active controlled flap actuators offers the capability for implementation of additional functionalities for the trailing edge with benefits on aircraft level and improvements at manufacture and assembly level. Thus, the distributed high lift system architecture is to be regarded as an enabler of the above-mentioned benefits, [15-20]. The important consequences in operation and maintenance following the issue of complex actuation networks, are amplified with the implementation of the sensor network, [21].

The high number of DOF, nearly infinite, is an immediate problem to manage when dealing with unconventional systems. A suitable sensor network aimed at monitoring morphing architectures should have a relevant extension and considerable density, suitable of catching the various shapes that are achieved during operation. This fact implies the deployment of a huge quantity of transducers that can reveal needed information on a suitable number of points. Accelerometers are widely used in common practice, both in lab and in flight, but have some features that suggest that other kinds of detection elements should be employed. Generally speaking, strain devices are more appropriate than displacement (velocity, acceleration) sensors because they avoid rigid motion contributions (coming from taxing, maneuver, and so on) that can disturb measurement output. Usually, they are also lighter. Moving from the former to the latter is just a matter of installation. Examples are strain gauges or optical fiber-based devices (Fiber Bragg's Gratings for instance, FBG), Figure 1.7.



(a) Metallic panel



(b) Composite panel

Figure 1.7. Distributed fiber optic sensing.

In recent years, much more attention has been turned to the design of nano filler for polymer materials to harness the exceptional electrical properties of CNTs. In particular, polymers with the incorporation of CNTs show great potential for microelectronic applications such as highly sensitive strain sensors for aeronautical smart systems. For such application, the direct current (DC) properties of nanocomposites are used. Currently, numerous experimental studies aimed to well characterize the electrical properties of nanocomposites, made from insulating polymers filled by CNTs, are being carried out. In this work, the research has been focus on assessing the resistivity properties of nanocomposites for potential aeronautical applications and in particular for smart structures. An intelligent structure must be able to measure in real time its deformation state: the example of a morphing wing is certainly useful to understand the ambitious realization of a sensing system for detecting strain variations under the action of the external load. Polymer-based composite materials belong to the family of ultra-light structural materials, which have been introduced massively in the recent years in aeronautical applications, but also in other fields like civil and automotive engineering as well. Moreover, the anisotropy of the elastic properties allows optimizing the performance of the structural materials, offering countless new design possibilities. Non-destructive testing and surveillance techniques have been developed over the years, mainly encouraged by the constant search of enhanced safety in the aeronautical industry and in civil engineering applications. However, the standard methods currently used are far from being optimal for these novel materials, and potential improvements in the continuous monitoring techniques are constantly being investigated. From this perspective, new Structural Health Monitoring (SHM) systems have thus emerged during the last years as an interesting option. To meet the demand, especially of the aerospace field, of more and more advanced materials, more intense studies are being carried out on carbon-fiber reinforced composite materials. CNTs reinforcements allow for modulating the characteristics of a polymer matrix composite making it also suitable for more extreme operating conditions and resistant to environmental damage. The advantages of carbon nanotube reinforcement are many. They allow to improve the mechanical characteristics of the composite. The most relevant aspect, however, lies in the electrical properties that make these composites suitable for the design of self-sensing materials. In other words, composite materials reinforced with CNTs are used as sensors as well as structural materials and this is a highly sought after goal in recent times. Electrical techniques are the non-destructive way to monitor damage in composites subjected to static and dynamic loads. However, this approach is not applicable to composites where the fibers are non-conductive, such as glass and aramid fibers. Damage detection through conductivity measurements offers many advantages when compared to traditional glass fiber optic sensors. In fact, because of their high cost, it is not possible to create a dense network of these fibers to inspect large parts of the composite and especially if the damage spreads in the material without crossing the fiber could also not be detected. Therefore, the reinforcement with carbon nanotubes is the among best candidates to go under the many aspects described.

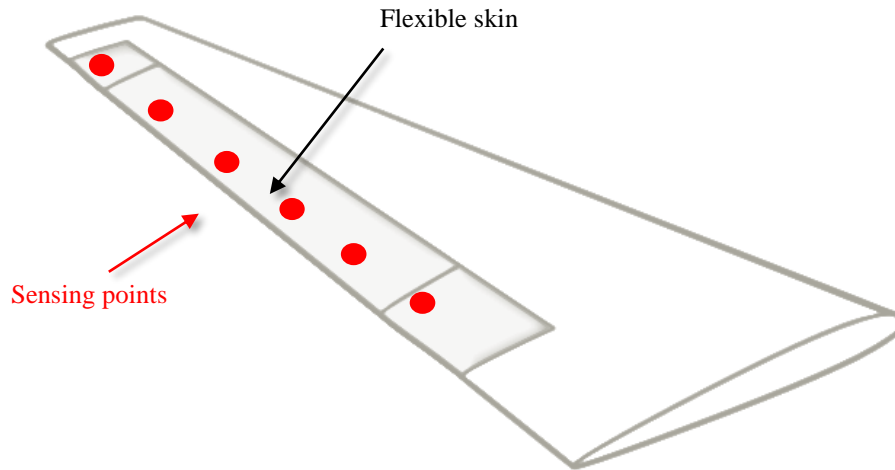


Figure 1.8. Smart sensing for adaptive wings, [21].

A successful development of nanotechnology and its implementation attracted the attention within several NASA missions. NASA's Langley Research Center explored the real feasibility to embed CNT-based sensors in structures of all geometries to monitor conditions both inside and at the surface of the structure to continuously sense changes. Global, real-time structural health monitoring systems for air and space vehicles require new strategies for the development of extremely small and lightweight sensors that are embeddable and scalable to arrays. Geometries with very thin regions (e.g., leading edges), sharp changes (e.g., wing/fuselage junctions) or areas of extremely high curvature are often impossible to instrument. NASA solves this issue with a flexible CNT-based structural health monitoring sensor for measuring the induced strain, pressure, and temperature both within and at the surface of a structure--an attractive candidate for smart skin technologies, [22-25]. The sensing capabilities of mechanical stress and strain for the SWCNT/polyimide nanocomposite were demonstrated via piezoelectric, piezoresistance and piezocapacitance response.

Towards the ready-to-fly intelligent systems

The interest toward the environmental impact of transports is gaining more and more attention, due to the various consequences it entails, such as climate changes. Inside the European Community, the ACARE reports some data, [26], regarding air transport contribution to climate change which represents 2% of the total CO₂ emissions (and the 12% of all transport sources). The objectives of the next twenty years regard a more environmental-friendly approach to the design and management of the aircraft, generally referred to a substantial reduction in emissions, both chemical and acoustic, and a reduction in consumption. These macro objectives are converted into many research topics including the development of innovative architectures able to optimize the configuration of the aircraft in various flight conditions, or able to adapt in the various phases of the mission. Significant improvements can be achieved by the implementation of novel configurations (shapes and architectural layout), propulsion systems improvement, integrated optimization and drag reduction, [27]. The design and optimization of high lift systems is one of the most complex task in aircraft design. It involves a close combination of aerodynamics, structures and kinematics. The evolutionary trend of the High-Lift Devices has been strongly driven by the dramatic improvement in aerodynamic tools for optimization, [28], and structural computational systems like elastic and rigid multi-body coupling simulations. Through this approach, satisfactory performance were attained with penalties in structural complexity and weight and therefore in costs. Later on, computational fluid dynamics (CFD) improvements permitted optimizing flap systems in 2D flow with a clear advantage for Fowler mechanisms that allowed reaching higher values of maximum lift, [29]. Such devices, on the other side, required even more complex kinematic actuation systems. Those flap systems used in fact massive mechanisms made of linear or curved tracks (translation) in conjunction with revolute joints (rotation), leading to significant weight penalties. The high weight drawbacks were principally due to the incidence of the aerodynamic loads, requiring stiff kinematic structures. High performance (C_{Lmax}) was achieved by means of multi-

slotted bi-dimensional flap design and experimental validation, [30]. Aircraft producers have participated for a long time to incorporate innovative technologies into their design process to attain innovative concepts for conventional structures. Among these concept, variable camber LE and TE, as depicted in Figure 1.9. In recent times, this target has been referred to as the development of “Morphing Wing Technology”, [31-32].

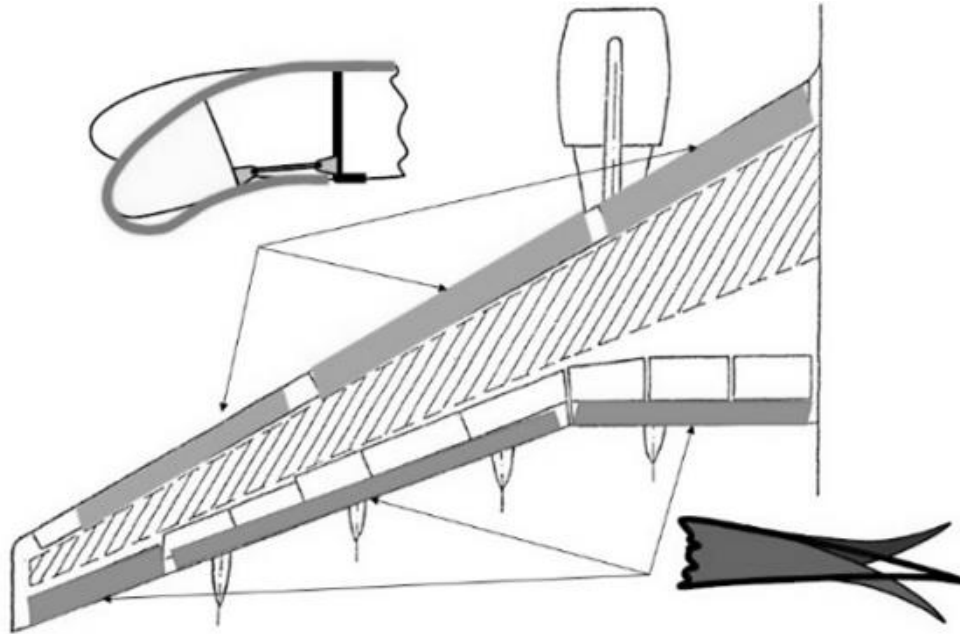


Figure 1.9. Variable camber LE and TE on an aircraft wing, [30].

The idea of changing the wing shape or geometry starts form the “inspiration from nature”. Early design is covered extensively in [33]. Compliant, variable camber devices appeared in a number of countries, as evidenced by the wide variety of patents issued in Great Britain, Germany and the United States. Otto Schmidt patented a variable camber device in Germany in 1895, Figure 1.10(a), [34]. The Wright brothers built the first heavier- than-air aircraft with engine with a twisted wing for roll control. Holle and Judge patented a variable camber device in Great Britain in 1917, Figure 1.10(b), [35] and Parker in 1920 in USA, Figure 1.11, [36].

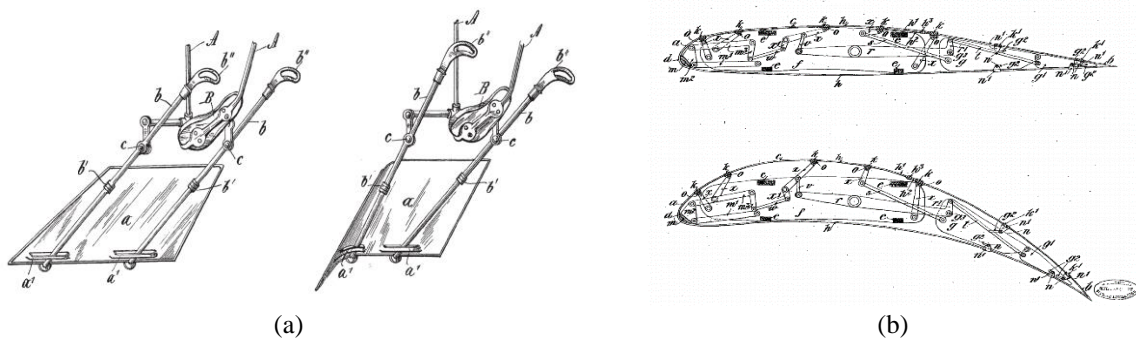


Figure 1.10. An earlier concept of control surface (a), [34], and a variable camber device (b), [35].

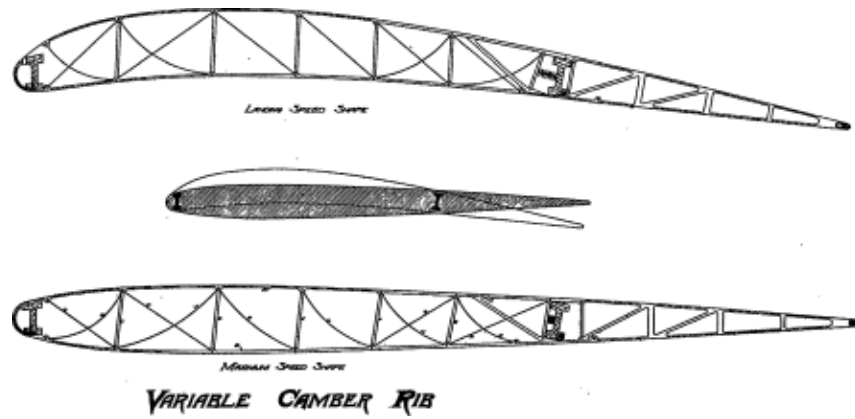


Figure 1.11. Parker morphing rib design, [36].

It is then noticeable that variable camber devices have been studied and investigated for long times, but only in recent year they found a practical application. Both in military (F-111 experiment, [37]) and commercial aviation (*FlexSys* flight test, [38]), morphing is turning into a breakthrough technology. In light of those successful developments, also in Europe, many research project were launched in order to develop innovative aircraft structure based on morphing devices. Among these, the most important research activities are SARISTU, [39], and CleanSky, [40], projects. In the framework of SARISTU project, a full-scale wing prototype equipped with three morphing architectures (trailing edge, leading edge and winglet) was developed and tested in wind tunnel, [41]. The design of the morphing trailing edge is widely described in [42]. The research project CRIAQ-MDO505, born by an intense Canadian and Italian synergy comprising industries, research centers and universities has allowed for investigating morphing structures potentials through the design and manufacturing of a variable camber aileron tailored for new regional aircrafts, [32]. In the Clean Sky scenario, an innovative flap morphing full-scale prototype has been realized for application on next generation green regional aircraft (CS-25 category). The first studies were limited to a portion of the flap element, [43], and then extended to a full-scale prototype as described in [44-45].

Aims of the thesis

The work discussed in this manuscript was developed as part of international collaborations and the personal contribution was specifically aimed at the design of the actuation, control and sensing systems for adaptive structures. The demand for augmented functionality, inevitably leads to more complex design arrangements which require a fully transversal and multi-disciplinary design approach: aeronautical sciences, robotics, biomechanics concepts must converge to a single technically satisfactory outcome. The focus activity of the doctorate was placed within the European Project Clean Sky 2, oriented towards the executive development of a multi-functional morphing flap for the next generation regional aircraft. Anyway, the scientific surveys were carried out on experimental platforms already available at the Smart Structures Lab (University of Naples “Federico II” – Aerospace Section). In such a way, different actuation and control strategies were investigated in order to face the greater complexity represented by the morphing flap end application. Numerical and experimental methods have been implemented looking always at the potential industrialization of these flyable solutions, meeting so the compliance with the current airworthiness requirements. The logical-temporal flow of the activities is schematized in the Figure 1.12. The overall research trend pursued by the author is in full agreement with the current needs for a “more electrical aircraft”. Design methodologies of robotic systems based on EMAs and distributed sensors have been carefully implemented to define systems with multiple degrees of freedom. The solving approach has been structured on several key aspects, but all interconnected to guarantee finally a robust system. The research path took place with investigations for the validation of the motion system of a camber-morphing aileron within the Italian-Canadian collaboration (CRIAQ-MDO505). The author's work has been encompassed in the design and modelling activities, contributing to a better identification of the dynamic effect (elasticity, damping and mass) of the actuators on the overall response of the system. Experimental evidence allowed to validate the approaches adopted (Chapter 2). Furthermore, rational approaches have been performed forecasting the impact of a distributed actuation system on the whole aircraft. Effects of aero-servo-elastic

instability as well as critical scenarios (failure and jamming of actuators) have been extensively studied with reference to reliability issues (Chapter 3). The results achieved on a small platform (morphing aileron) have been duly extended to the flap region. As part of the Clean Sky framework, an innovative actuation system has been developed that comprises electro-mechanical modules. A challenging key aspect was the ability to get and preserve desired target wing shapes within a certain tolerance, allowing optimal aerodynamic performance in operative conditions and loads. In the Chapter 4, the strategies followed to define the electro-actuation and control system of a morphing flap have been therefore outlined with emphasis on both numerically and experimental methodologies that have been implemented. The design choices were also conditioned by the presence of other devices that further complicate the layout of the flap. It was in fact envisaged that the final device will be equipped with plasma synthetic jets (PSJ) for the optimization of the aerodynamic performances. The operation of these devices could represent a possible source of disturbance for the control system conceived. Electro-magnetic interferences of the actuators with the other electronic equipment of the flap have been assessed according to EMC (Electro-Magnetic Compatibility) specification, crucial for the safety of modern electric aircraft. The additional operative modes of morphing flap consist in symmetrically deflecting and twisting the tab segment: it is supposed to be activated in cruise condition only, when the flap is stowed in the wing. Because of the progress in research of advanced composites, flexible wing parts are maturing and becoming more attractive for application in the aviation industry. In the particular case of the morphing tab, the possibility of developing a single compliant composite segment is being analysed. The author has investigated a potential sensing system useful for identifying the structural deformation state when the external skin could be stretched under the aerodynamic load (Chapter 5). The main steps of the activities related to each project are summarized in the Table 1.1.



Figure 1.12. Ph.D. Research International Framework.

Table 1.1. Summary of Ph.D. Research activities.

CRIAQ MD0-505 <i>Morphing Aileron</i>	Dynamic modelling of actuators
	Aero-servo-elastic effects of actuators
	Numerical-experimental correlation
	Validation of actuation performances
Clean Sky - JTI <i>Bi-Modal Morphing Flap</i>	Distributed actuation design
	Control logic implementation
	Experimental activities on an «iron bird»
Clean Sky 2 - Airgreen 2 <i>Multi-Modal Morphing Flap</i>	Distributed actuation design
	Control logic strategy
	EMC analysis with PSJ system
	Integrated sensing system design

References

- [1] Crawley, E.F. and de Luis, J.: Piezoelectric actuators as elements of intelligent structures, *AIAA Journal* 25(10), 327–343 (1987).
- [2] Wada, B.K., Fanson, J.L. and Crawley, E.F.: Adaptive structures, *Journal of Intelligent Material Systems and Structures* 1(2), 157–174 (1990).
- [3] Sun, J., Guan, Q., Liu, Y. and Leng, J.: Morphing aircraft based on smart materials and structures: A state-of-the-art review, *Journal of Intelligent Material Systems and Structures* 27(17), 2289–2312 (2016).
- [4] Thompson B.S., Gandhi M.V. and Kasiviswanathan S.: An introduction to smart materials and structures, *Materials & Design* 13(1), 1–9 (1992).
- [5] Yousefi-Koma, A. and Zimcik, D.G.: Applications of Smart Structures to Aircraft for Performance Enhancement, *Canadian Aeronautics and Space Journal* 49(4), 163–172 (2003).
- [6] Speckmann, H.: Structural Health Monitoring with Smart Sensors Approach to a New NDI Method, *Proc. SPIE Conference on Smart Structures and Materials and NDE for Health Monitoring and Diagnostics*, 17-21 March 2002, San Diego, California.
- [7] Speckmann, H.: Structural Health Monitoring (SHM): One Technology of the Airbus Intelligent-Airframe philosophy, *Proc. Of the Asia-Pacific Workshop of Structural Health Monitoring Yokoama/Japan* (Ed.: A. Mita).
- [8] Concilio, A. and Lecce, L.: *Morphing Wing Technologies Large Commercial Aircraft and Civil Helicopters, Historical Background and Current Scenario* (Elsevier Book), 3–84 (2018).
- [9] Srinivasan, A.V. and McFarland, D.M.: *Smart Structures: Analysis and Design*, Cambridge University Press, Cambridge (2001).
- [10] Wiener, N.: *Cybernetics or Control and Communication in the Animal and the Machine*, The MIT Press, Cambridge, MA, ISBN 978-0-262-73009-9 (1961).
- [11] Kim, J. H., Matson, E. T., Myung, H. and Xu P. (eds): *Robot Intelligence Technology and Applications 2012 - An Edition of the Presented Papers from the 1st International Conference on Robot Intelligence Technology and Applications*, Springer Science & Business Media, Berlin Heidelberg, ISBN 978-3-642-37374-9 (2013).
- [12] Kalkan, S., IEEE Staff (ed): *2015 International Conference on Advanced Robotics (ICAR)*, IEEE Publishing, New York, NY, ISBN 978-1-467-37510-8 (2015).
- [13] Rushby, J.: A safety-case approach for certifying adaptive systems, *AIAA Infotech@Aerospace Conference*, Seattle, WA, April 6-9 (2009).
- [14] Herrera, C. Y., Lung, S. F., Ervin, G. and Flick, P.: Aeroelastic airworthiness assessment of the adaptive compliant trailing edge flaps, *46th International Symposium of the Society of Flight Test Engineers*, Lancaster, CA, September 14-17 (2015).
- [15] Wheeler, P. and Bozhko, S.: The More Electric Aircraft: Technology and challenges, *IEEE Electrification Magazine*, 2(4), 6–12 (2014).
- [16] Sarlioglu, B. and Morris, C.T.: More Electric Aircraft: Review, Challenges, and Opportunities for Commercial Transport Aircraft, *IEEE Transactions on Transportation Electrification*, 1(1), 54–64 (2015).
- [17] Wheeler, P.W., Clare, J.C., Trentin, A. and Bozhko, S.: An overview of the more electrical aircraft, *227(4)*, 578–585 (2012).
- [18] Castellini, L., D’Andrea, M. and Borgarelli, N.: Analysis and design of a linear electro-mechanical actuator for a high lift system, In: *2014 international symposium on power electronics, electrical drives, automation and motion*, Ischia, Italy, 18-20 June 2014, 243–247.
- [19] Bennett, J. W.: *Fault Tolerant Electromechanical Actuators for Aircraft*, Ph. D. thesis, Newcastle University (2010).
- [20] Qiao, G., Liu, G., Shi, Z., Wang, Y., Ma, S. and Lim, T.C.: A review of electromechanical actuators for More/All Electric aircraft systems, *Proc IMechE Part C: J Mechanical Engineering Science*, 232(22), 4128–4151 (2018).
- [21] Mukhopadhyay, S.C. (Ed.): *New Developments in Sensing Technology for Structural Health Monitoring*, *Lecture Notes in Electrical Engineering*, Springer-Verlag, Berlin, Heidelberg, ISBN 978-3-642-21099-0 (2011).
- [22] Viscardi, M., Arena, M., Barra, G., Vertuccio, L., Ciminello, M. and Guadagno, L.: Piezoresistive strain sensing of carbon nanotubes-based composite skin for aeronautical morphing structures, *Proc. SPIE 10599, Nondestructive Characterization and Monitoring of Advanced Materials, Aerospace, Civil Infrastructure, and Transportation XII*, 105991C (2018).

- [23] Trigweil, S., Snyderl, S., Hatfield, W., Dervishi, E. and Biris, A. S.: Carbon nanotube coatings as used in strain sensors for composite tanks, NASA Technical Report (2011).
- [24] Kang, J.H., Sauti, G., Park, C., Scholl, J.A., Lowther, S.E. and Harrison, J.S.: Carbon Nanotube/Polymer Nanocomposites Flexible Stress and Strain Sensors. Symposium M: Materials and Technology for Flexible, Conformable, and Stretchable Sensors and Transistors MRS Spring Meeting (2008).
- [25] Samareh, J.A. and Siochi, E.J.: Systems analysis of carbon nanotubes: opportunities and challenges for space applications, *Nanotechnology* 28(37) (2017).
- [26] ACARE official site: <http://www.acare4europe.com/>
- [27] Goldhammer, M.: The Next Decade in Commercial Aircraft Aerodynamics – A Boeing Perspective, ROI 2009-0501-1167, Aerodays March 2011, Madrid (Spain).
- [28] Strüber, H.: The Aerodynamic Design of the A350 XWB-900 High Lift System, proceeding of ICAS 2014, St. Petersburg, Russia, 7-12 September (2014).
- [29] Rudolph, P.K.C.: High Lift Systems on Commercial Subsonic Airliners, NASA Contractor Report 4746, September (1996).
- [30] Reckzeh, D.: Flying Community Friendly – The Role of High-Lift Aerodynamics, Design concepts & solution for the future, KATnet II conference 2009, Bremen (Germany).
- [31] Peter, F. and Stumpf, E.: Morphing Wing Technologies Large Commercial Aircraft and Civil Helicopters – The Development of Morphing Aircraft Benefit Assessment, 103-121, Elsevier Book (2018).
- [32] Amendola, G., Dimino, I., Concilio, A., Pecora, R., Amoroso, F. and Arena, M.: Morphing Wing Technologies Large Commercial Aircraft and Civil Helicopters – Morphing Aileron, 547–582, Elsevier Book (2018).
- [33] Wagg, D., Bond, I., Weaver, P., and Friswell, M.: Chapter Four: Lightweight Shape-Adaptable Airfoils: A New Challenge for and Old Dream, *Adaptive Structures: Engineering Applications*, edited by Campanile, L.F., Wiley, New York, 89–129 (2007).
- [34] Schmidt, O.: Steuerapparat für Flugmaschinen, Schmidt Patent No. 84532 (1895).
- [35] Holle, A.A., and Judge, A.W., U.K. Patent No. 103400, 25 Jan. (1917).
- [36] Parker, H.F., The Parker Variable Camber Wing, NACA Fifth Annual Rept. 77 (1920).
- [37] F-111 Mission Adaptive Wing, Advanced Fighter Technology Integration, NASA CP-3055 (1990).
- [38] FlexSys Technology Fact Sheets: www.flxsys.com.
- [39] Official site of SARISTU consortium: www.saristu.eu.
- [40] Official site of Clean Sky consortium: <http://www.cleansky.eu>.
- [41] Pecora, R., Concilio, A., Dimino, I., Amoroso, F. and Ciminello, M.: Structural Design of an Adaptive Wing Trailing Edge for Enhanced Cruise Performance, 24th AIAA/AHS Adaptive Structures Conference, AIAA SciTech, 4-8 Jan (2016).
- [42] Pecora, R., Amoroso, F., Magnifico, M., Dimino, I. and Concilio, A.: KRISTINA: Kinematic Rib based Structural system for Innovative Adaptive trailing edge, SPIE Smart Structures/NDE, Las Vegas, Nevada (USA) March 2016. Proc. SPIE 9801, Industrial and Commercial Applications of Smart Structures Technologies 2016, 980107 (2016); 10.1117/12.2218516.
- [43] Pecora, R., Amoroso, F., Amendola, G. and Concilio, A.: Validation of a smart structural concept for wing-flap camber morphing, *Smart Structures and Systems*, 14(4), 659–679, October (2014); <http://dx.doi.org/10.12989/sss.2014.14.4.659>.
- [44] Pecora, R., Amoroso, F. and Magnifico, M.: Toward the bi-modal camber morphing of large aircraft wing flaps: The CleanSky experience, Proc. SPIE 9801, Industrial and Commercial Applications of Smart Structures Technologies 2016, 980106 (2016); 10.1117/12.2218415.
- [45] Pecora, R., Amoroso, F., Arena, M., Noviello, M.C., and Rea, F.: Experimental validation of a true-scale morphing flap for large civil aircraft applications, Proceedings Volume 10166, Industrial and Commercial Applications of Smart Structures Technologies 2017; 101660L (2017); <https://doi.org/10.1117/12.2259878>.

Awards

- [1] May 2015 Award: “Premio Venezia,” Category “Scientific and Academic” for the CRIAQ MDO 505 project, “Morphing Architectures and Related Technologies for Wing Efficiency Improvement” <http://www.italchamber.qc.ca/fr/documents/programme2015.pdf>.
- [2] April 2016, Morphing Flap Project, Nomination for the Best Clean Sky Project Award in 2016.
- [3] July 2017, Best Oral Presentation Award, The 2nd International Conference on Energy Engineering and Smart Materials, ICEESM 2017, Lyon, France, July 7-9, 2017.

2. Dynamic Modelling of Electro-Mechanical Actuation

The research project CRIAQ-MDO505, Canadian-European cooperation project on smart technologies, has investigated morphing structures potential through the design and the manufacturing of a variable camber aileron tailored to CS-25 category aircraft applications. The ailerons typically constitute crucial elements for the aerodynamic forces equilibrium of the wing. Therefore, compared to the traditional architectures, the need of studying the dynamic performance is, in the specific case of servo-actuated variable-shaped systems, higher. Relying upon the experimental evidence within the present research, the issue appeared concerns the critical importance of considering the dynamic modelling of the actuators in the design phase of a smart device. The higher number of actuators involved makes de facto the morphing structure much more complex. In this context, the action of the actuators has been modelled within the numerical model of the aileron: the comparison between the modal characteristics of numerical predictions and testing activities has shown a high level of correlation. Moreover, the compliance of the device with the design morphing shapes has been proved by wind tunnel test. The outcomes are expected to be key insights for future designers to better comprehend the dynamic response of a morphing aileron, primary knowledge for safety analyses.

2.1 Framework

Nowadays, in the international greening research framework, the morphing technology is playing an important role among the smart structures for the many benefits concerning the reduction of the fuel burn and noise emitted. Adaptive structures may in fact contribute to a significant improvement of the aerodynamic and structural performance over conventional architectures. Morphing research projects will revolutionize the costs of building and operating aircraft. Research team had the interest to verify the applicability of those concepts to the aileron region in order to understand the applicability of the morphing technology while preserving the standard functionality of the control surface. In fact, the aileron zone is very complex from the aeroelastic point of view because instability events, due to the reduced stiffness and the complex aerodynamic field. In addition, the aileron constitutes a primary control surface which failure can be dramatic for the aircraft safety. On the other side, this zone showed the better potentialities for the implementation of the adaptive devices. A morphing aileron adds new functionalities to classical aircraft systems. While keeping its classical function (roll, manoeuvre), it implements camber morphing during cruise, to accomplish aircraft weight variations following fuel consumption or to redistribute span-wise loads to reduce the Root Bending Moment (RBM). It was developed inside the research project CRIAQ-MDO505, a cooperation between Italian and Canadian teams, [1-2]. The objective of that research was to design, manufacture and test in wind tunnel conditions, a smart wing section of a CS-25 aircraft, (Figure 2.1(a)) made of an adaptive box with flexible skin (conceived, designed and developed by the Canadian team) and a morphing aileron (Figure 2.1(b)).

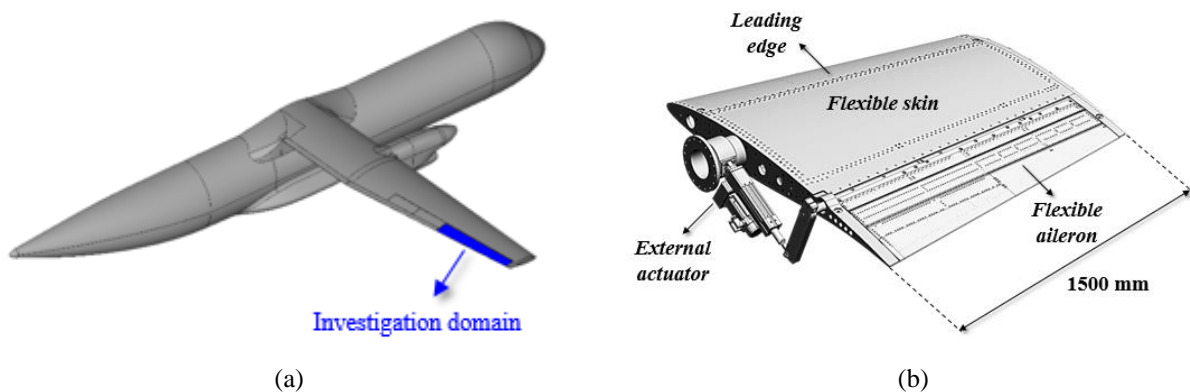


Figure 2.1. A schematic view of the reference wing (a) and the developed morphing devices (b), CRIAQ-MDO505 project.

Due to the particular unconventional design of the aileron, the author focused on carrying out several experimental activities addressed to substantiate the design strategies. For its greater complexity, a more “robotized” structure requires an even more in-depth study compared to a classical configuration. The effect of the actuation systems is certainly an example parameter to be duly taken into account during the design and verification phases. Changes in dynamic characteristics such as modal mass, stiffness and damping following the actuators activation can influence, also significantly, the dynamic response of an adaptive system. In literature there are just few references regarding the vibrational behavior of a multi-actuated morphing wing. A first investigation was conducted by H. Yuanyuan and G. Shijun in [3] to model and evaluate a morphing wing with an innovative actuation system integrated into the seamless control surface. Vibration tests were performed to validate the first three elastic modes (first two flexional and torsional). Several papers were instead published with regards to the design of actuation systems and their respective control laws. A general algorithm was developed by Austin et al. for static shape control of structures with internal actuators. The shape-control theoretical method was validated by tests conducted on a real model, [4]. Studies for optimal placement of the actuators with a focus on activities aimed at practical implementation were presented in a review, [5]. The design, simulation, and control of the miniature linear actuator used in the actuation mechanism of the morphing wing was presented in [6]. The same authors studied in addition two control methods for obtaining optimized airfoil configurations for fixed wind flow conditions. Both CFD simulations and wind tunnel tests results were combined, [7]. The main purpose of the present work is to identify the modal behavior of the morphing aileron with particular regard to the influence of servo-actuators on the global response. Vibration analyses highlighted an interesting result about the morphing mode shape, which characterize the adaptive wings. It should be theoretically a rigid mode having so a null natural frequency. Nevertheless, the experimental activities have shown that this particular frequency is much higher and increases of about 20% when the actuators are fully activated. This outcome required that this aspect must be taken into account within the numerical modelling phase of the system then an engineering-based method to simulate the effect of the actuators was developed by the author in this chapter. The validated model representative of the fully operative condition (actuators activated) will be then matched with the aircraft aeroelastic scheme for future flutter analyses with respect to relevant operative configurations. Furthermore, the robustness of the adopted mass balancing as well as the persistence of the flutter clearance in case of relevant failures/malfunctions of the morphing system components will be proved according to EASA CS-25 regulations, [8]. The present scenario shows the main results arising in the final phase of the morphing aileron design. All the lab tests were preparatory for the wind tunnel campaign. The chapter presents finally the experimental campaigns conducted in wind tunnel, aimed at correlating the morphing shapes under external load as well as to evaluate the aerodynamic performance of the aileron. The data therefore clarifies the good geometrical correlation between the target analytical shapes and the wind tunnel actual shapes. The effects induced by the technology at aircraft level will be then analyzed in perspective of potential certification and industrialization processes.

2.2 Reference Aileron System

Aileron morphing shapes

The design of a morphing aileron and hence, more in general, of an adaptive device, starts from the definition of the external aerodynamic shapes. They include the baseline and the two morphed configurations (up and down). The shapes are computed on the base of an aerodynamic optimization procedure with the objective to delay transition from laminar to turbulent flow, [9]. Such target contours should be matched by a proper internal structural configuration (rigid-mechanism or compliant) under the effects of the external loads. In fact, the aileron is based on a tailored kinematics driven by an appropriate actuation system in accordance with structural constraints such as:

- aileron tip deflection, computed as the angle between the original and the modified chord, fixed in the design range $[-7^\circ; +7^\circ]$;
- continuous monotonic curvature of the morphed camber lines (no changes in the sign of the slope of aileron camber);
- no chord line variation induced by morphing.

In accordance with the specifications, the aileron main hinge axis remains unmodified and it is located at 70% of the chord as typical position for a 78-seats regional aircraft which is the reference plane of such device. In Figure 2.2 is depicted the aileron trailing edge segment, from 70% to tip, for all the target configurations.

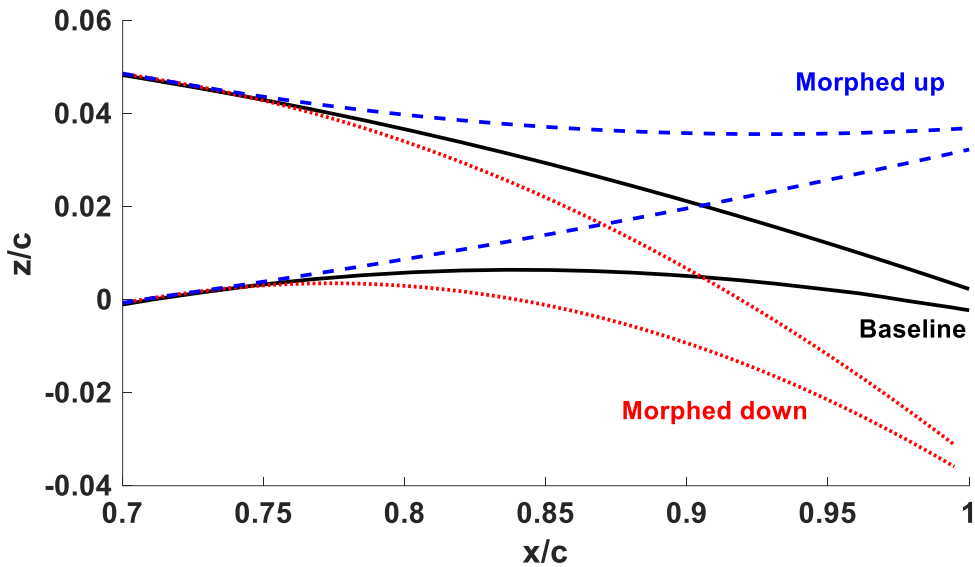


Figure 2.2. Morphing aileron aerodynamic shapes.

The adaptive rib

The proposed aileron rib architecture was based on the well-known *finger-like* mechanism properly tailored to enable camber morphing. The rib mechanism uses a three segment polygonal line to approximate the camber of the airfoil and to morph it into the desired configuration while keeping practically unchanged the airfoil thickness distribution. Each rib was assumed to be segmented into three consecutive blocks (B0, B1, B2, Figure 2.3(a)) connected by means of hinges located on the airfoil camber line (A, B), Figure 2.3(b). The rib structure is a multi-degree-of-freedom mechanism where each block can be moved by a dedicated actuator. However, it is not feasible to have two drivers for each rib, because of the clear drawback in terms of excessive weight and number of components with significant impact on the maintenance and the reliability. B0 and B2 are then connected through a namely rigid linking rod element (L, Figure 2.3(a)) which reduce the kinematics to an SDOF system. The actuator must supply the required torque (or force) necessary to equilibrate the aerodynamic moment and also to surmount external load in order to move in morphed up and down the aileron ribs.

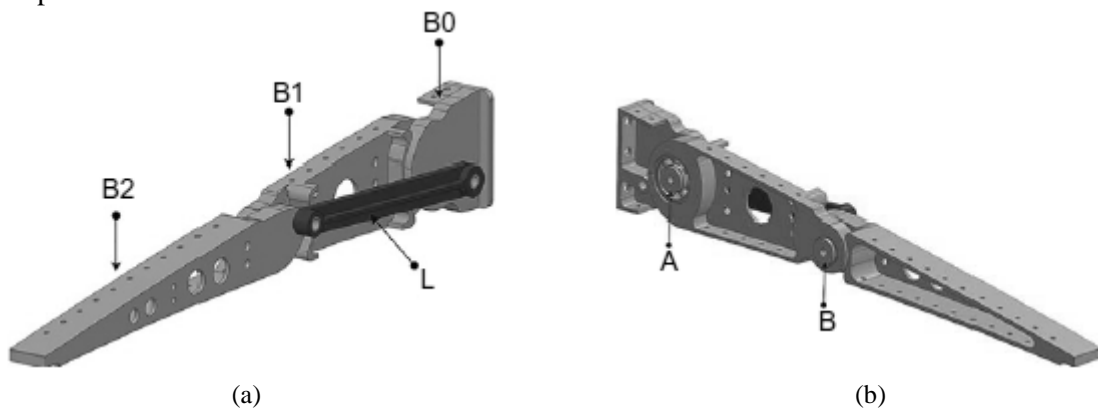


Figure 2.3. Morphing rib architecture: (a) blocks and hinges, (b) link.

Skin

For typical camber morphing applications, it is necessary to substitute the conventional skin with a flexible one, adequately deformable along the longitudinal direction to allow structural shape change and on the contrary, robust enough in the traverse path to withstand aerodynamic pressure. In literature, many design solutions can be found, based on innovative materials such polymeric foams or flexible matrix composites, [10-12]. Inside the SARISTU project, in particular, a skin was proposed, made of a sequence of flexible and stiff segments, covered with adhesive silicone layer used to protect the system and guarantee a certain continuity among foam and aluminum parts. The skin design results truly dependent on the target application; for the aileron, an intermediate design between conventional and innovative skin was developed. A multi-module skin was considered (Figure 2.4, conformal to the multi-box segmentation: in detail, the three blocks were covered with a standard aluminum skin. They were shaped in such a way to reduce the gaps at a minimum and to rotate with respect to each other like sequential meniscuses. Airflow leakage at the segments interfaces was minimized through low-friction silicone seals. However, the segmented skin dynamics does not provide a significant impact over the aileron torsional stiffness; actually, the torsional frequencies between a conventional single-layer skin and a multi-block solution, have been numerically compared by the author on the same reference model. The natural frequency of the observed mode, assuming an alloy single skin, resulted slightly higher than a segmented one, by 14%. In any case, such vibration frequency does not represent a risk for the aeroelastic stability of a potential vehicle, being at the borderline of the [0; 60 Hz] spectral range, generally adopted within flutter investigations for CS-25 aircraft category.

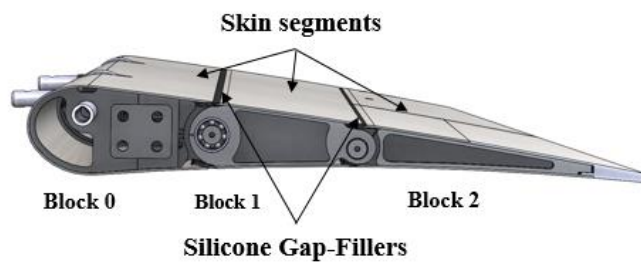


Figure 2.4. Morphing Aileron CAD with detail on the Aluminum skin segments and silicone seals.

The actuation system

The aileron was then equipped with a dedicated and self-contained actuation system. Due to the very small thickness, only two bays were actuated; the others moved as constrained to the second bay actuator, (slave ribs). The conceptual scheme of the actuation system was widely discussed in [11], both analytically and numerically. In synthesis, it is based on a “direct-drive” oscillating glyph mechanism which components are recapped in Figure 2.5 below.

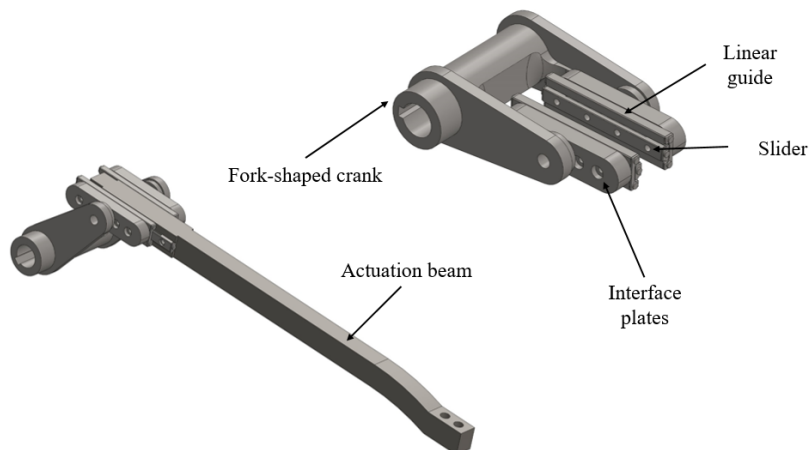


Figure 2.5. Actuation system layout on the morphing aileron.

Many types of linear guides may be found on the market, on the base of maximum allowable load, mass, sliding mechanism characteristics, overall dimensions, etc. Due to the aileron limited room, only miniaturized linear guides were taken into account in a sort of inverse design process. In fact, at first, size requirements were satisfied in order to avoid any interference with the upper and lower skins during the system operation. Considering actuator specs and individual performances, the Bental RSA-06 actuator has been selected due to its contained weight (less than 0.5 Kg) and dimensions with respect to the other candidates that satisfy the same specifications (Torque: 6.5 Nm, Operating Voltage: 28 V DC).

Overview of the integrated aileron

The aileron structural components have been integrated; in fact, ribs are connected by means of a *multi-box* arrangement, as shown in Figure 2.6. The main geometrical dimensions are herein also reported. The multi-box configuration consists of connecting each span-wise rib with longitudinal stiffeners, namely called spars or stringers, in order to create a closed box as indicated in Figure 2.6(a). The mechanics was designed for synchronous actuation, i.e. no differential motion is namely allowed for consecutive chord-wise segments even if a non-synchronous actuation (structural torsion) could bring to interesting benefits, like the capability of modulating the span-wise load; however, several other issues should have been considered. For instance, the necessity of giving some more degrees of freedom, longitudinally, would have brought to a less stiff architecture, with consequent limits in absorbing external loads. The aileron airfoil maximum thickness percentage is 15% representative of 66 mm at root section and 49 mm at tip. Such tiny dimensions drive the design of the kinematic because the actuators and leverages must be contained into the aileron shape without any structural interferences during morphing. For this reason, it has been difficult to actuate each ribs due to restricted space, in fact the last part of the aileron, as indicated in Figure 2.6(b), are considered passive and its movement is driven by the active segment. Such a passive region is bounded by deformable, non-actuated ribs and is detached from the remaining part of the wing. In synthesis, three actuator systems were deployed on the structure, one for each of the first three ribs towards the wing root. The other two ribs are moved by the third, inner actuator. This device absorbs therefore by itself the incoming load on the external bay.

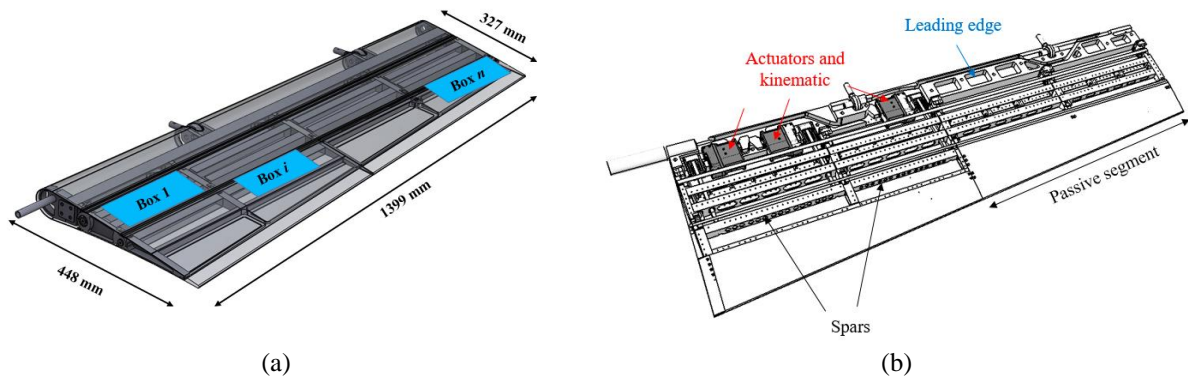


Figure 2.6. Morphing aileron structure: multi-box arrangement (a) and internal layout (b).

2.3 Finite Element Model description

In order to verify the modal behavior of the referred morphing architecture and to correlate the experimental data, a very refined finite element model was carried out. The structural model has been realized with one dimensional (*rod* and *cbush*), plane (*cquad*) and solid (*ctetra*) finite elements, [14]. Figure 2.7 shows the aileron finite element model. Two-dimensional mesh was used to model spars, skin and trailing edge, while, on the other hand, aileron ribs were modelled with three-dimensional finite elements.

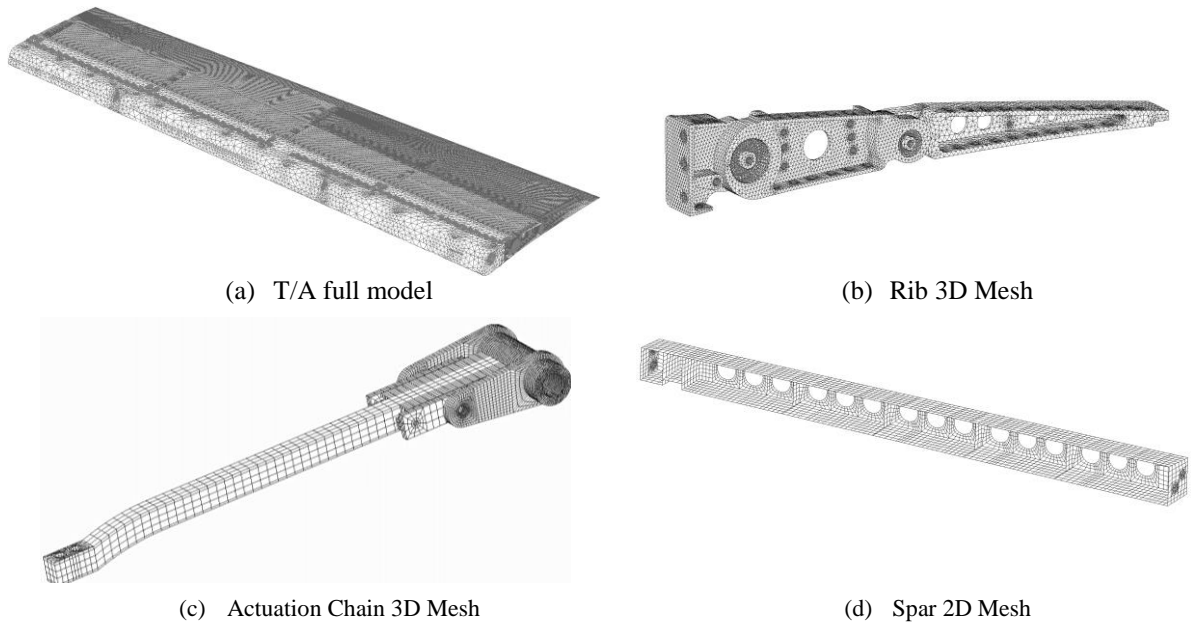


Figure 2.7. Morphing aileron, finite element model.

The link between rib block 0 and 2, which essentially absorbs normal stress, can be modelled with a 1D *cro*d connected to the corresponding rib through *cbeam* with pin flags imposed at the end-nodes of such elements to allow the relative rotation between the connecting items, Figure 2.8. For each fastener or screw hole, a master node was generated at the centre and connected to all the nodes on the edge by a *RBE2* element. The fastener was then modelled with a spring, namely a *cbush* element, joining the master nodes at the centre of each hole.

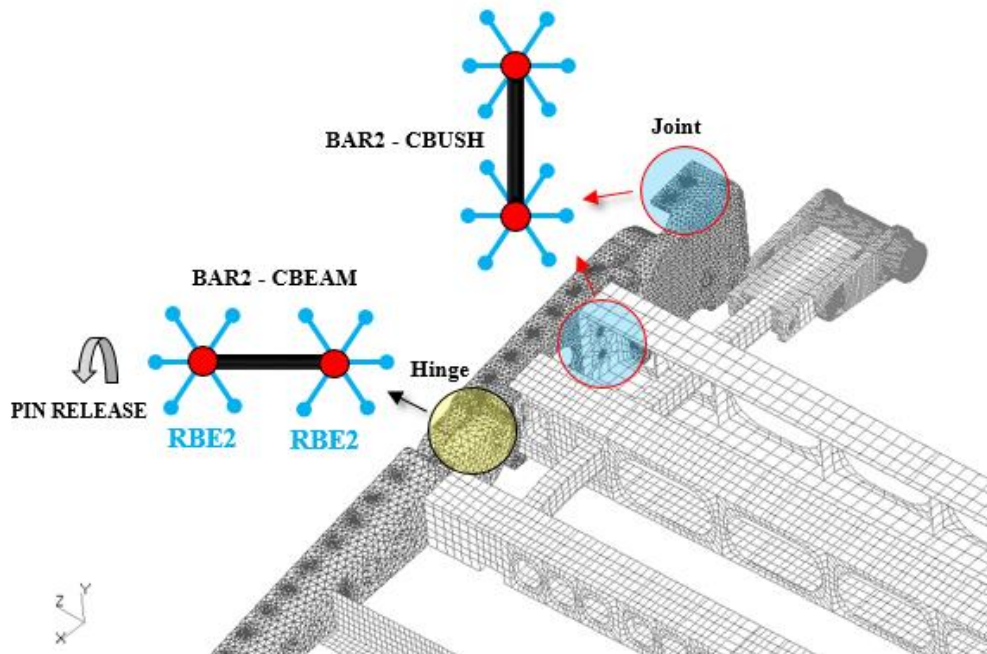


Figure 2.8. Hinge simulation and fastener modelling.

Table 2.1 reports the main characteristics of the model. The current finite element model consists of a high number of nodes and elements, properly necessary to best fit the aileron geometrical CAD. Notwithstanding

the forgoing considerations, the same model is also addressed to estimate the dynamic behavior of the aileron in terms of normal modes.

Table 2.1. FEM characteristics.

FE Entity	N°
Nodes	567237
RBE2 (Rigid Beam Element Type N.2)	1354
CTETRA (Connection Tetrahedral Element): • Ribs & Leading edge	440043
CHEXA (Connection Hexahedral Element): • Actuation chain	89748
CQUAD (Connection Quadrilateral Element): • Skin, trailing edge	149117
CBAR (Connection Bar): • Fasteners, Pin	1019

All the components of the morphing aileron, apart from the steel links, are made of aluminium (Type code Al2024-T351). Therefore, this was the material assigned to all the elements. The materials properties are listed in Table 2.2. In particular, as first way to verify the numerical model consistency, the global structural mass of the aileron FE model was estimated around 19 kg (about 10 kg for the only leading edge) which is close to the value of 19.2 kg of the weighted manufactured prototype. This measure is coherent with the fact that rivets and other joints were not considered in the computation. In this analysis, targeting the tests in WT on a very rigid structure, this variation was not considered important. On the other side, modal analysis, static response, and dynamic response did match well the experimental results. If a flyable or more compliant demonstrator (for instance, an aileron deployed on a long-span wing), these contributions should be evidently taken into account.

Table 2.2. Aileron materials.

Material	E [GPa]	ρ [kg/m ³]	ν	Items
Steel C50	220	7850	0.3	Actuation system beam; Linear guide features; crank and rib links
Al 2024-T351	70	2768	0.33	All other items

2.4 Experimental activities

A prototype of the aileron was manufactured and tested for the experimental campaign before the wind tunnel assessment. The lab tests were aimed at:

- demonstrating the morphing capability of the conceived structural layout by means of its functionality;

- estimate the real aerodynamic shapes in order to evaluate CAD deviation due to the manufacturing and assembly process;
- characterizing the dynamic behavior of the morphing structure through the identification of the most significant normal modes. This task is necessary for the future aeroelastic computation and related FHA analysis.

The experimental tests herein shown are carried out with traditional methodologies, well-assessed within the working group and are applied to the original structural configuration herein presented to verify its static and dynamic properties and validate the numerical models.

2.4.1 Functionality tests

The functionality test consisted in characterizing the aileron kinematic in terms of actuator rotation and rib deflection. This is analytically expressed by Eq. (2.1). It allows for calculating the actuator shaft rotation (β) needed to achieve a given morphing angle (φ). It allows the designer to estimate the actuator rotation range to obtain the morphing deflection between -7° to $+7^\circ$. The parameter L represents the distance from actuator shaft to kinematic rotation center. These tests were carried out to demonstrate that the flap was able to reproduce target morphed shapes in a controlled and repeatable manner. The aileron was morphed up and down, as in Figure 2.9. For each morphing angle, within the effective range $[-7; +7]$ deg expected from the wind tunnel test matrix, a given actuator shaft rotation was imposed and the tip displacement was measured as shown in Figure 2.10. In each position for the considered range, the tip displacement was measured and is graphically reported as a function of the actuator rotation. A good match with the numerical results is shown. The very small deviations observed can be largely explained with the measurement method that was implemented, based on images elaboration. The morphing aileron prototype was used as technological demonstrator to prove the adequacy of the adopted solutions with respect to design requirements and system specifications.

$$\cot\varphi = \frac{L}{R\sin\beta} \cot\beta \quad (2.1)$$

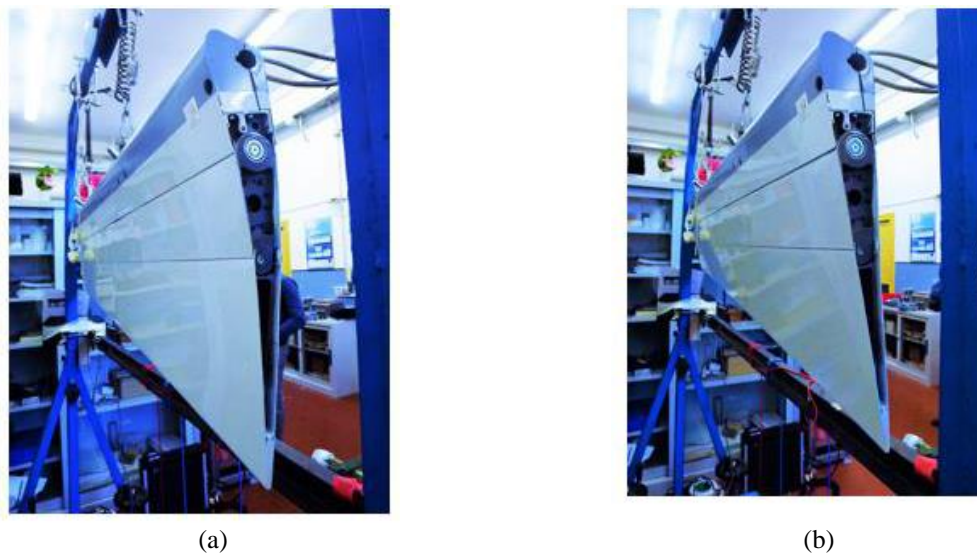


Figure 2.9. Powerplant functionality test: morphed down (a), morphed up (b).

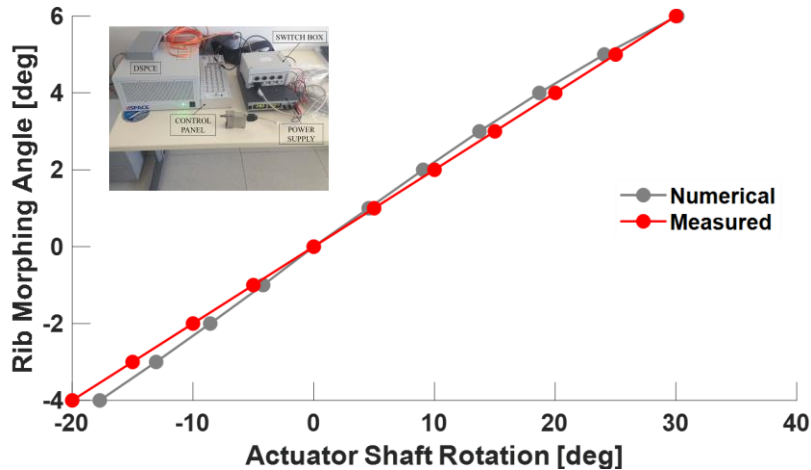


Figure 2.10. Correlation between numerical and experimental: actuator rotation vs morphing rib deflection.

2.4.2 Ground Resonance Test and FE updating

The Ground Vibration Test (GVT) was carried out in order to validate the dynamic FE model of the morphing aileron. In such manner, a proved finite element model will generate good results for the upcoming aeroelastic analysis (flutter instability) and FHA assessment [15], leading to a safe wind tunnel tests. The structural dynamic response and excitation loads were measured respectively by means of a tri-axial piezoelectric accelerometer, positioned in a characteristic point of the T/A and hence, a load cell connected to the electro-dynamic actuator through a light-weight metallic stringer. In order to simulate the free-free condition, the prototype was suspended by means of two low-stiffness springs to an aluminum test rig (T/R) with the aim to get a proper frequency separation between pendulum oscillation and structural elastic modes. The experimental set-up details are represented in the following Figure 2.11.

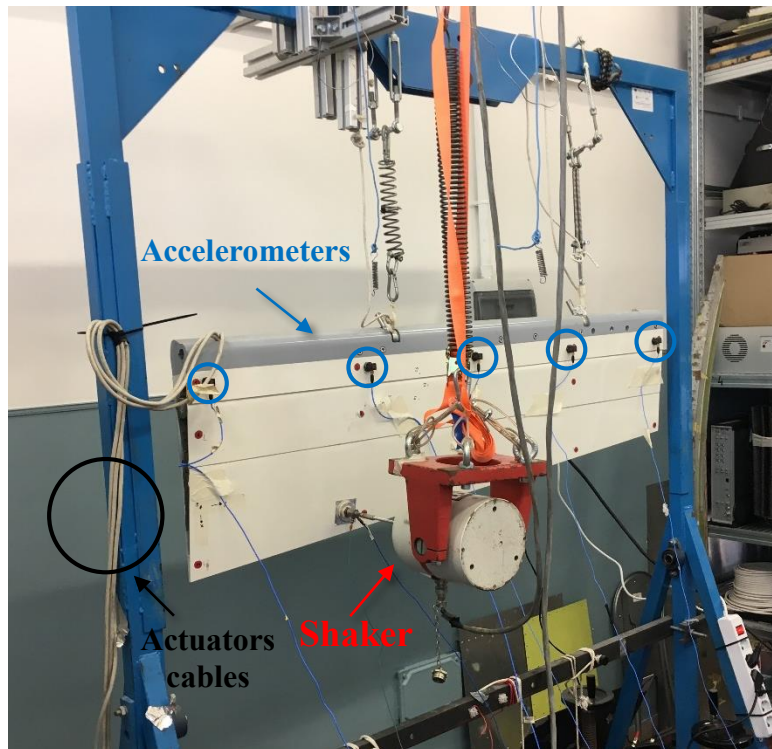


Figure 2.11. Test-article suspended with low frequency springs.

The electro-dynamic shaker was suspended on an independent rig to prevent again an undesired coupling with the test article. It provided a sine force peak of 98 N and a peak-to-peak stroke of 17.6 mm. Fifteen acquisition points have been defined for this test as shown in Figure 2.12.

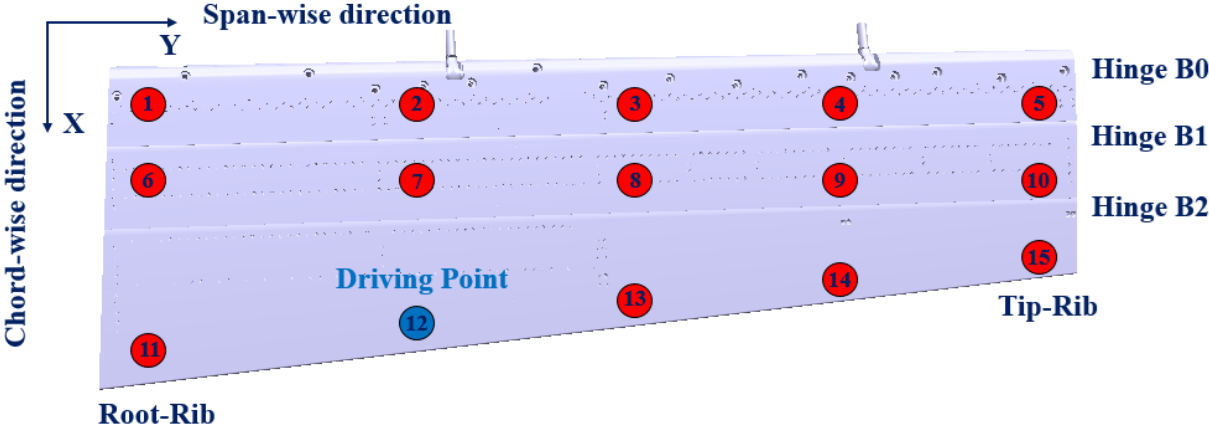


Figure 2.12. T/A grid points: geometric layout.

The modal parameters achieved within the Frequency Response Functions (FRF) analysis were estimated by means of a LMS DAQ system which procedure is represented in Figure 2.13. The post-processing step evolved within Matlab® environment allowed for characterize the following information:

- The T/A resonance frequencies;
- The mode shapes;
- The modal damping.

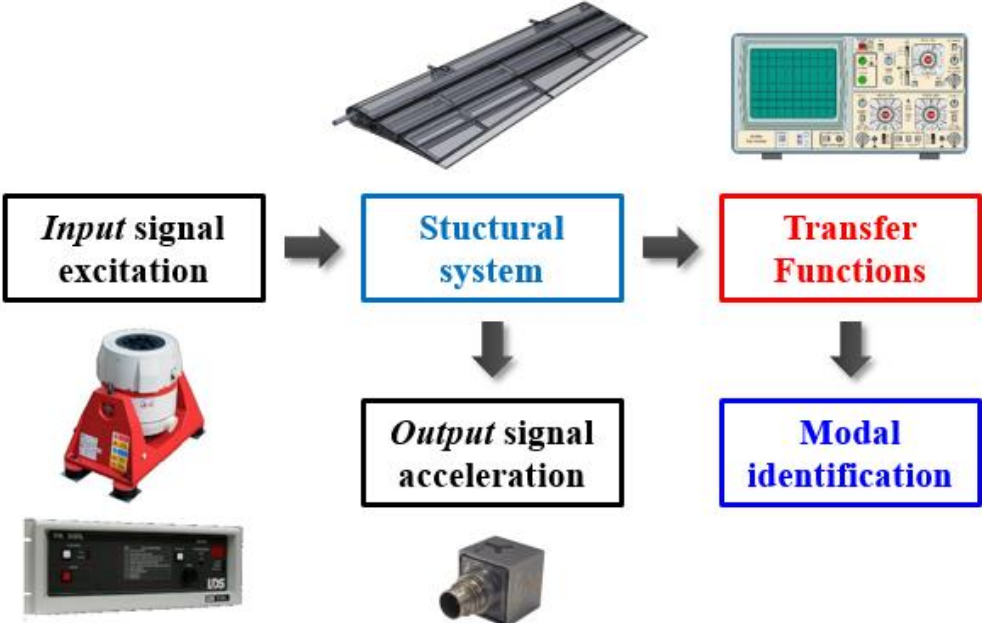


Figure 2.13. Conceptual scheme of the modal parameter estimation strategy in Ground Vibration Testing.

The GVT were carried out according to the following test-matrix reported in Table 2.3.

Table 2.3. Ground Vibration Test matrix.

GVT	T/A Configuration	GVT Objective
A-1	Unmorphed, Actuators disabled (Power OFF – Failure simulation)	<i>Normal Modes Identification</i> (0-200 Hz)
A-2	Unmorphed, Actuators enabled (Power ON – Operational condition)	

The experimental modes have been identified both for the A-1 and A-2 tests. They were conducted in power-off and power-on conditions, respectively. These states refer to the actuator system that is in charge of modifying the shape of the aileron along its chord, which works independently on the main actuator responsible for the aileron rigid rotation around its main hinge axis. The former configuration aims at simulating the effects of the actuators failure condition (less stiffness in correspondence of the actuator shaft) while the latter, is the usual operative condition. The dynamic response of the aileron in both operating conditions is represented in Figure 2.14.

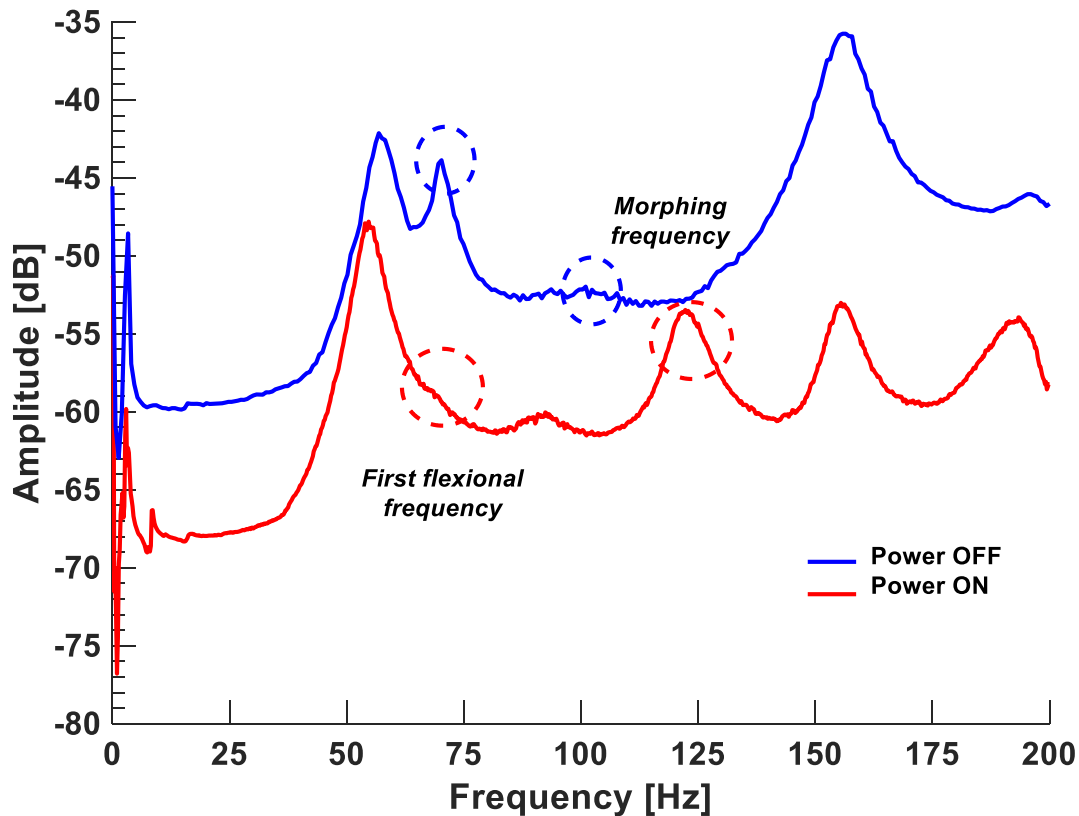


Figure 2.14. Frequency Response Function (FRF), effect of servo-actuators activation.

Power OFF

The curves above in Figure 2.14 show an interesting behaviour of the morphing aileron. When the actuators are off, the structure exhibits a low generalised stiffness that leads to a large displacement field. This behaviour is constant overall the investigated range. At the same time, the associated damping is significant, as the shaped peaks reveal; it is an index of a dissipation that can sometimes achieve a magnitude around 10% and more. The associated large displacements confirm this point: they are mainly linked to free rotations and movements, associated to hinges distribution. It is indeed notable how the "morphing" mode

(the mode that resembles the uniform kinematic motion of the adaptive part of the structure) has an own stiffness also in the "free motors" case, when it should instead have a pure free-play motion. This is mainly linked to the contribution associated to the intrinsic stiffness of the actuators, they exhibit also in this case. Theoretically, in the assumption of actuation system full failure and hence, in total absence of dry friction in the hinges, this motion would be representative of a rigid mode ($f = 0$ Hz), evolving according to specific gear ratios among each block.

Power ON

When the morphing actuation system is activated, the stiffness increase affects the global aileron dynamic response, leading to about 20 dB response reduction in the investigated interval, Figure 2.15. In the same graph, a significant reduction of damping does appear; exiting rigid movements, friction conditions are avoided. Generally, it is seen a remarkable eigenvalues stability that represents a fundamental goal especially in the design of movable surfaces. This surprising frequency stability may be explained by the simple consideration that the associated mass is different: when the actuators are ON, all the structure contributes to the movement, while as the actuators are OFF, the main displacement is mainly associated with the morphing element. The different masses compensate therefore the different stiffness. All these effects appear in any driven shape (reference, morphed up, morphed down, Figure 2.2); in other words, changes of geometry do not seem to affect the modal characteristics, significantly. A remarkable difference verifies with the "morphing" mode, a kinematic-based one that undergo an about 20 Hz shift, moving from almost 100 to 120 Hz. Because of the induced activated actuator stiffness, particularly important in that frame, damping reduced for more than a half, moving from around 8 to 3.5%.

Considerations

These occurrences arise some interesting problems. It is important to underline that the "actuators-off" condition simulates an ill-functioning of the system, as a consequence of a damage or other bad event. Therefore, the analysis of its behaviour is important from the point of view of the safety. The experimental evidence, provides some good expectations from this specific point of view. On the other side, the actuators that have been implemented should not work in power off conditions: the structural stiffness is low and this could bring to complex underdamped aeroelastic phenomena (morphing mode). The devices should be always ON that would mean higher energy consumption and shorter life or inspection times. The sequence of the modal frequencies and the associated modal damping are shown in Table 2.4.

Table 2.4. GVT measurements summary.

Mode n°	Frequency [Hz]	Modal Damping [%]	Description
1	57.13 (OFF)	4.52 (OFF)	<i>1st Torsional Mode</i>
	54.49 (ON)	4.75 (ON)	
2	66.12 (OFF)	1.21 (OFF)	<i>1st Flexural Mode</i>
	67.48 (ON)	1.40 (ON)	
3	91.98 (OFF)	9.28 (OFF)	<i>2nd Flexural Mode</i>
	91.33 (ON)	8.79 (ON)	
4	99.75 (OFF)	7.62 (OFF)	<i>Morphing Mode</i>
	122.15 (ON)	3.50 (ON)	
5	155.68 (OFF)	2.45 (OFF)	<i>3rd Flexural Mode</i>
	155.32 (ON)	2.59 (ON)	

6	195.78 (OFF)	2.87 (OFF)	<i>2nd Torsional Mode</i>
	194.07 (ON)	4.42 (ON)	

The FRF shows that a very appreciable vibration level reduction (V.R., computed as by Eq. (2.2)) is observable with respect to the activated servo-actuators configuration: max decrease is estimated and reported in Figure 2.15, up to a maximum value of more than 17 dB (mode 5, 3rd flexural mode). The largest value is achieved for the flexural modes, meaning that the actuators effect is particularly evident for those shapes. In the representation of Figure 2.16-2.21, they are clearly associated to large deformations of the structure in the actuation region, justifying the abovementioned result.

$$V.R. (dB) = 10 * \log_{10} \left(\frac{g_{ON}}{g_{OFF}} \right) \quad (2.2)$$

Where g is the normalized acceleration respectively with internal motors enabled and disabled.

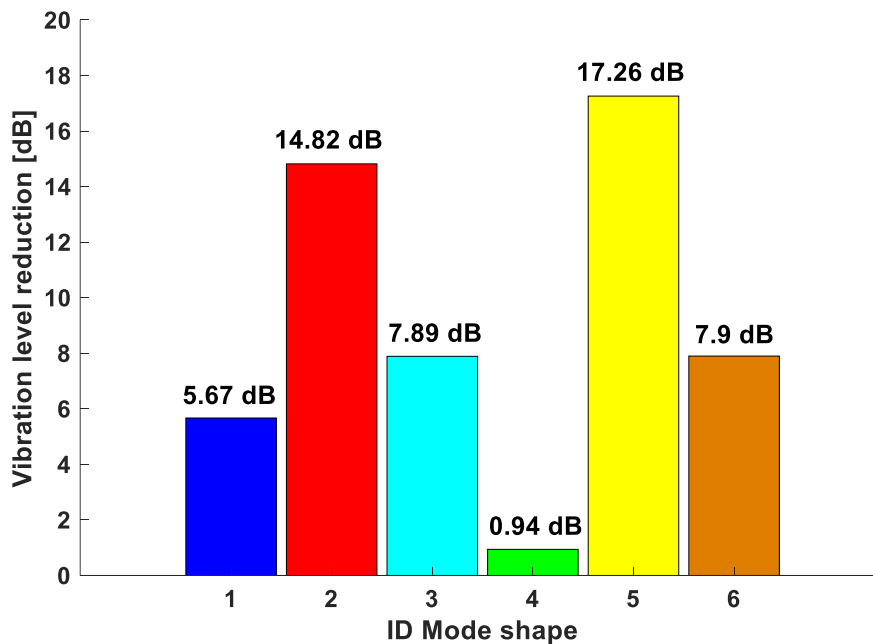


Figure 2.15. Vibration level reduction: power actuators effect.

FE model validation

These tests were mainly addressed to identify normal modes, with particular focus to the morphing one, in order to validate and tune the numerical model and prepare the ground to estimate the impact on the aeroelastic stability of this kind of devices. Figure 2.16 to Figure 2.21 report both experimental and numerical mode shapes for the power OFF configuration. The correlation was carried out by comparing the experimental modal analysis results (modal frequencies and shapes), achieved by implementing the Lanczos' method, [16]. As already mentioned, the experimental analysis highlighted the stiffening of the morphing mode as the actuator system is on, mainly due to the effect of the localized added stiffness of the working motors on the global structural response. This effect modifies significantly the related eigenvector, as it is shown in Figure 2.22.

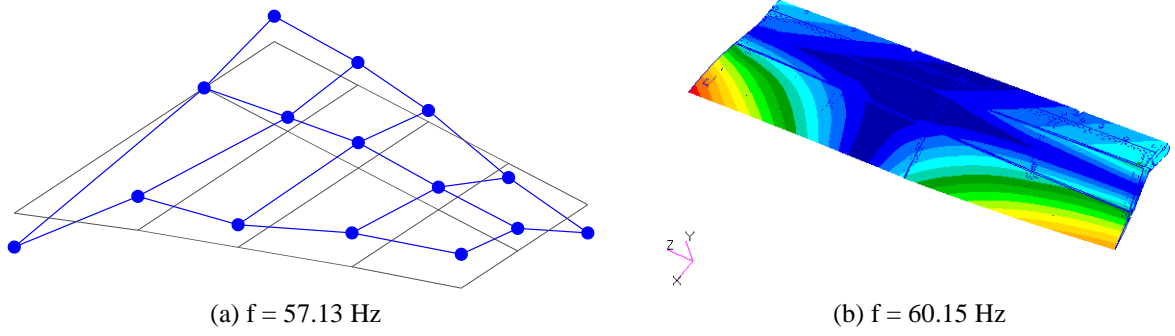


Figure 2.16. First torsional mode: experimental (a), FEM (b), Power OFF.

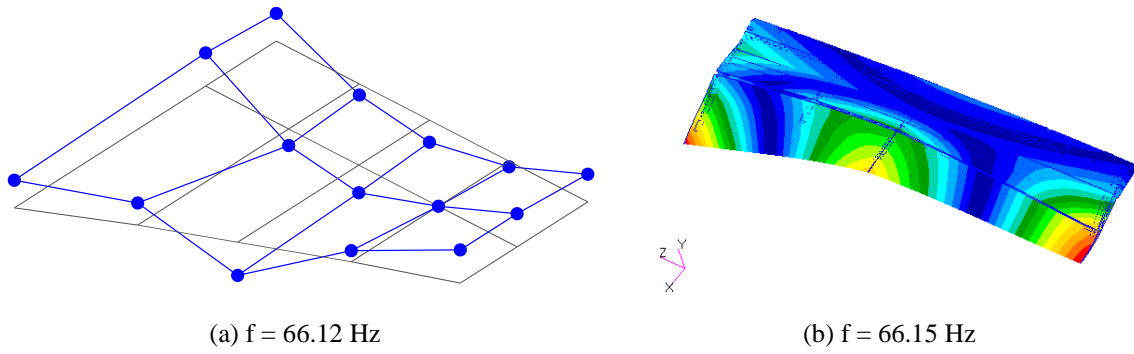


Figure 2.17. First flexural mode: experimental (a), FEM (b), Power OFF.

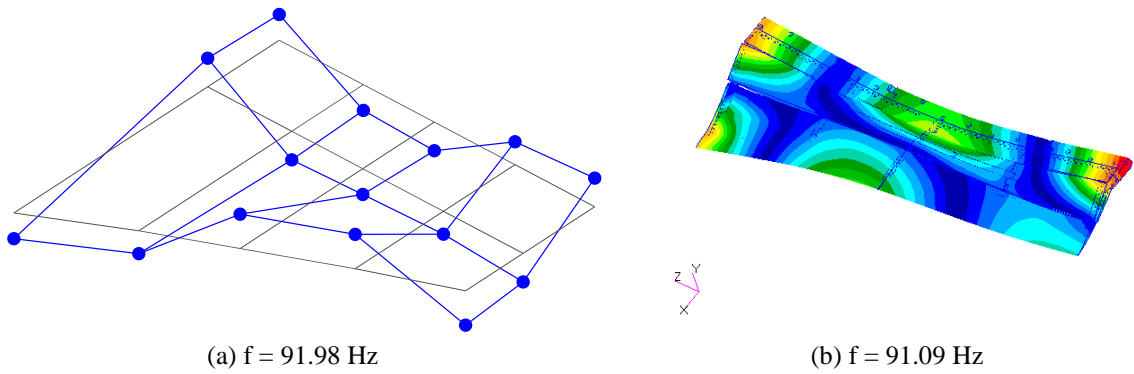


Figure 2.18. Second flexural mode: experimental (a), FEM (b), Power OFF.

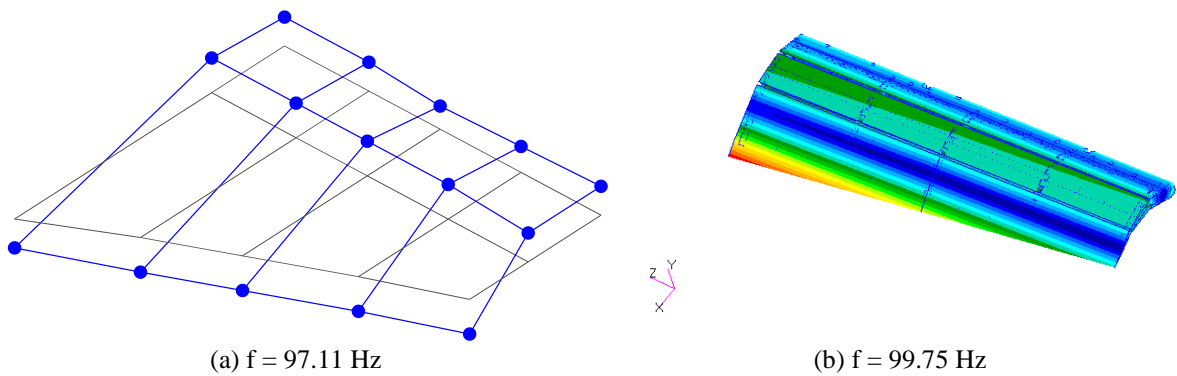


Figure 2.19. Morphing mode: experimental (a), FEM (b), Power OFF.

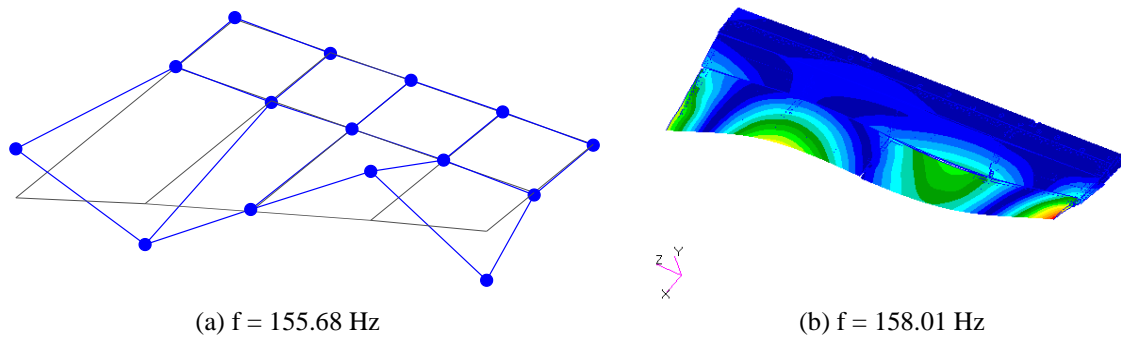


Figure 2.20. Third flexural mode: experimental (a), FEM (b), Power OFF.

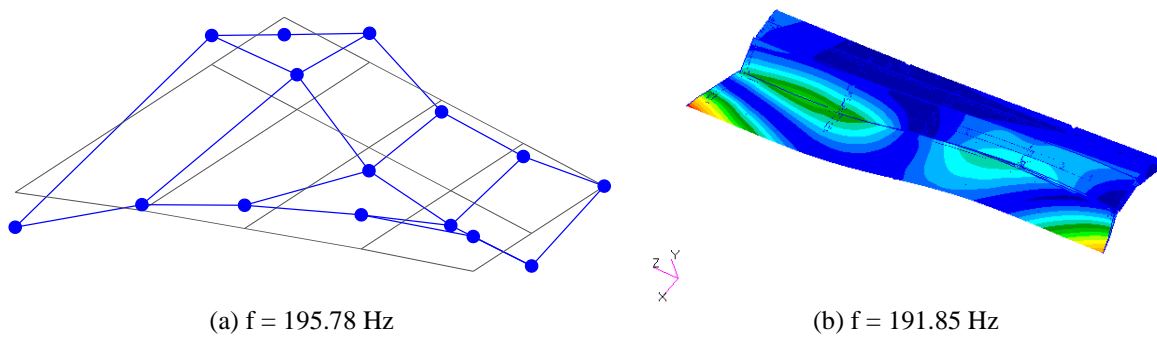


Figure 2.21. Second torsional mode: experimental (a), FEM (b), Power OFF.

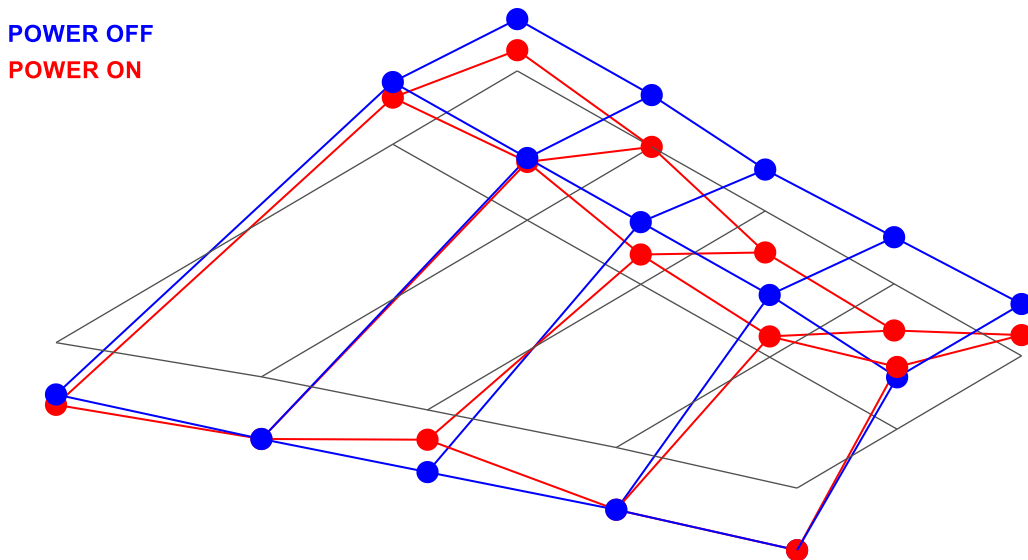


Figure 2.22. Morphing mode shape change, $f = 122.15$ Hz, $\zeta = 3.5\%$, Power ON.

The classical “quasi-rigid” motion transforms into a more complex shape, involving partial flexural behavior: in other words, constraining the actuator beams (connected to motor action, now ON), augments the local stiffness and move the deformability to other regions of the structure. The other modes are not considerably affected by the activation of the actuator system. FE model update was then carried out to

improve the match with the measured modes. This step has been achieved without significantly modifying the dynamic model properties: the fork-shaped crack mechanism has been coupled to a torsional spring coaxial with the actuator shaft, Figure 2.23. The actual stiffness K_a of each actuator can be treated as the sum of two main contributions: a “hard” stiffness k_a intrinsically present in the actuator even when it is disabled and another one Δk_a due to an increase once it is power supplied. As cited before, the morphing motion should be theoretically a rigid-body mode among the structural blocks with elastic energy of deformation null, then exhibiting an oscillating frequency equal at 0 Hz, Figure 2.24. Nevertheless, the experimental evidence shows how this frequency is far from being null, therefore it demonstrated that the actuation system integrated in the morphing aileron plays a great part of the structural stiffness.

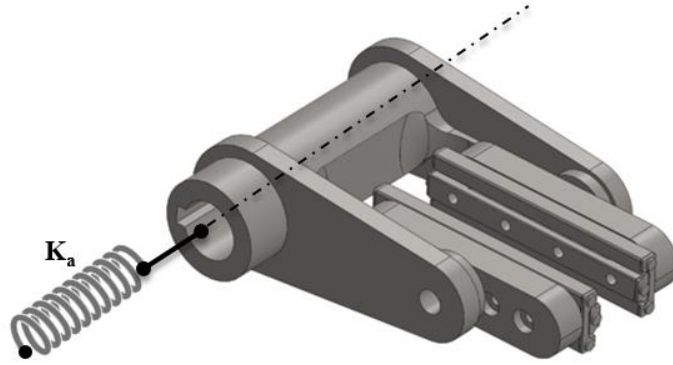


Figure 2.23. Numerical modelling of the servo-actuator.

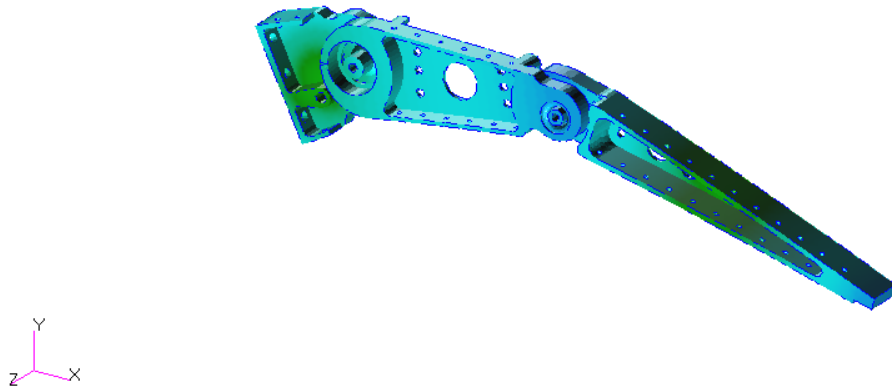


Figure 2.24. Rigid morphing mode of the single rib, $f = 0$ Hz.

One way to evaluate the stiffness constant based on the vibration test results may be to consider the three actuators in a parallel configuration, therefore according to Eq. (4.3):

$$K_{a_{tot}} = \sum_{i=1}^3 K_{a_i} = (2\pi f_m)^2 M_G \quad (4.3)$$

where f_m represents the morphing frequency while M_G the generalized mass associated to it. Relying upon the M_G of the un-actuated finite elements model and experimental morphing frequencies, the local stiffness of the actuator for the final numerical updating are about 8000 Nm/rad for power-off condition and 12000 Nm/rad for the power-on one. This approach is however based on the assumption that the theoretical modal shapes with respect to power-off configuration are in good agreement with the experimental ones and this verification has been achieved by a MAC index comparison as well as to consider the modal mass of the

structural morphing mode remains unchanged if the actuators are inserted. The modal mass of morphing mode estimated by numerical simulations is in each case quite close to 0.0204 Kgm².

Experimental-Numerical Correlation

In Figure 2.25 comparison of observed and predicted normal modes are reported: all the frequencies in the investigated spectral range (0-200 Hz) are very close to the bisector line (straight line with 45 degrees slope with respect to the axes), indicating a very good match between the values (regression coefficient, $R^2 = 0.97$). The same can be deduced for the power on configuration: the resonance frequencies do not deviate much from the former case, excepting for the morphing one.

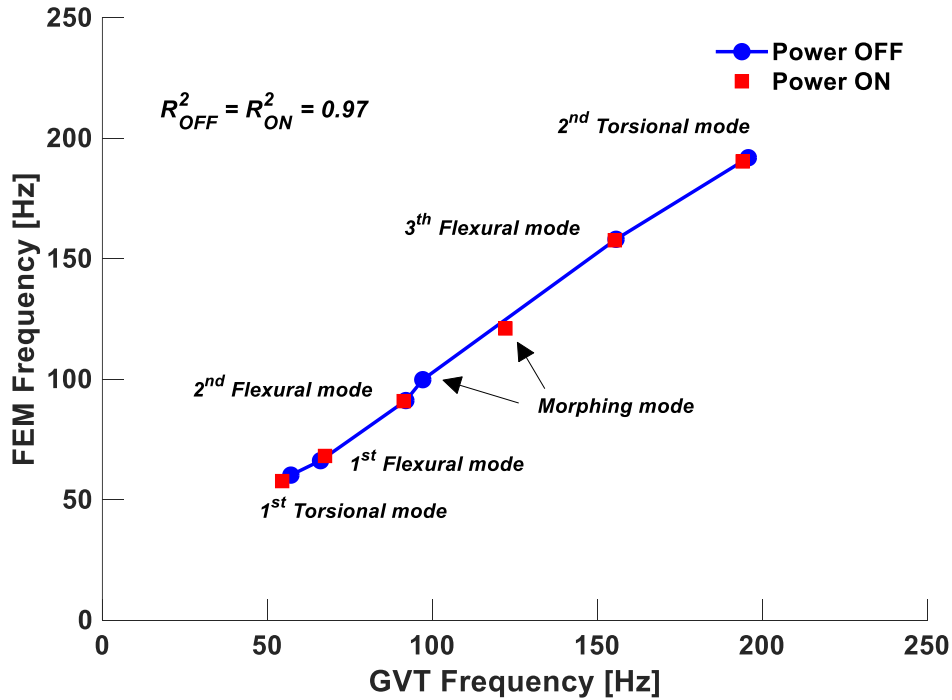


Figure 2.25. Experimental-FEM data correlation: natural frequencies comparison.

The mode shapes comparison in terms of *MAC* is summarized in Figure 2.26, following the numerical update process, previously described. *MAC* approach was used to verify the quality of the numerical modal shapes: values of this parameter close to one, shows a good agreement between theoretical and experimental data, Eq. (4.4).

$$MAC(num, exp) = \frac{|\{\psi\}_{num}^T \{\psi\}_{exp}|^2}{(\{\psi\}_{num}^T \{\psi\}_{num})(\{\psi\}_{exp}^T \{\psi\}_{exp})} \quad (4.4)$$

In the expression, ψ are the modal vectors, the pedex *num* means FE-predicted modes while *exp* indicates the experimental ones. The calculation was carried out by comparing the modal displacements (normalized to the maximum) then the eigenvectors of the numerical model with the experimental complex functions at the acquisition map points. For this purpose, the theoretical displacements referred to the master nodes of fifteen *rbe2* elements representing test markers on the aileron test article. *MAC* does not take into account frequency information and may show good correspondence between modes having remarkable range separation. Therefore, natural frequency comparison is also needed, Figure 2.25. Overall *MAC* values are next to 1 for each modal shapes in the power-off condition, Figure 2.26(a). Lower values are recorded for the 5th and 6th modes (*MAC* equal to 0.79 and 0.74, respectively); this result may be linked to the complexity of the modal deformations and to the need of extending the measurement points network. The correlation coefficient *MAC* was calculated again with respect to the updated numerical model. Also in this case the

trend confirms a good level of correlation between numerical and experimental forms, Figure 2.26(b). As expected, the elastic deformations remain almost unchanged even in the case of actuators activated contrary to what happens for the morphing mode, which results at a higher frequency.

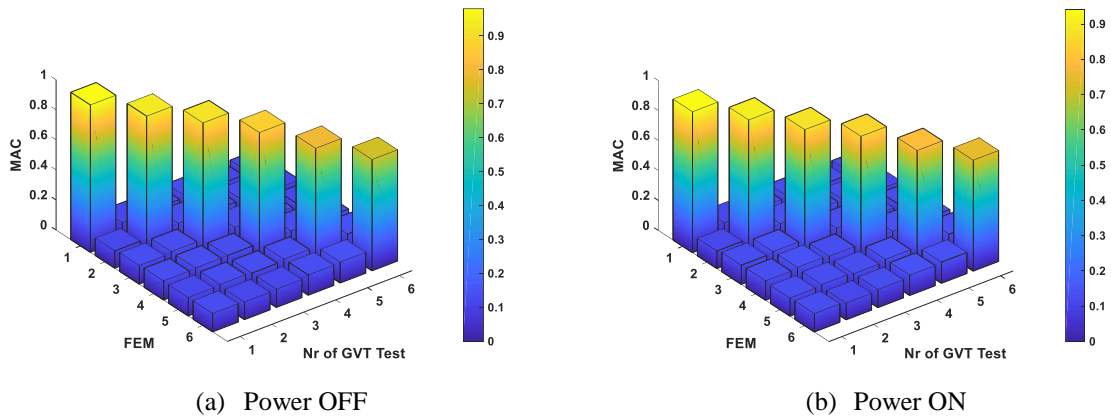


Figure 2.26. Experimental-FEM data correlation: MAC.

Linearity Analysis

The overall input load level, given the aileron in this analysis by an electro-mechanical shaker system, can be obtained by integrating the area under the power spectral density curve, Figure 2.27(a), and computing its root square. The peak at the very low frequency is due to a coupling mechanism between the shaker and the structure dynamics, both in free-free conditions. The impedance match emerges when two systems are coupled: in this case exciter and excited items. When the structure tends to move according to a pendulum mode (rigid mode, at very low frequency) and the shaker keeps up with the structural acceleration, a large energy transfer does occur, and the peak reported in Figure 2.27(a) arises. In order to avoid that, the driving point is typically moved to other suitable locations, where the structure is less compliant, yet still adequately exciting the bandwidth of interest. In this specific case, however, this did not seem necessary as the set-up allowed detecting the mode shapes of interest all over the investigated frequency range. Having assessed that issue, the behavior of the structure under the external excitation, in both the configurations ON and OFF, was studied. Figure 2.27(b) shows the relation between the resonance frequency of the torsional normal mode (the 1st elastic mode) and the input force level in the two mentioned cases. If the analysed system were linear, such curve would be flat, i.e. the resonances would not be dependent on the external excitation modulus. A slight decrease is instead shown in the power-off configuration, as the input force grows (around 1-2%). A similar but inverted phenomenon occurs when the actuators are on: the structure exhibits a slight stiffness increase as the force level increases. Then, such analysis detected non-linear response characteristics that were associated to mechanical parts dry friction and couplings.

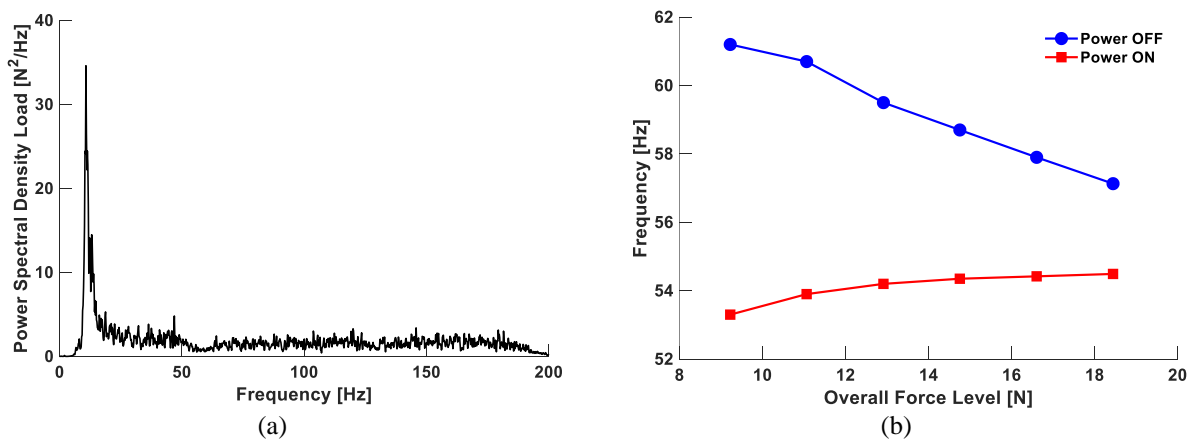


Figure 2.27. Load spectrum at maximum voltage level, (a) and Linearity test for Torsional Mode, (b).

2.5 Actuation Performance in Wind Tunnel Test

Aerodynamic benefits are very sensitive to the actual wing shapes achieved during the aircraft mission. For this reason, it is necessary to measure the actually attained shape with the target one, in order to measure the structural deviation arising during the phases of manufacturing and assembly. This information can be used in many ways: for instance, inserted into a feedback control loop, it could allow achieving the necessary information for an optimal actuator adjustment, so to minimize the error. In Figure 2.28, the reference CAD model forms are shown. Such target geometries were then approximated with a set of discrete points in order to have a proper comparison with the measured shapes according to the S1 reference system. The aileron is represented in both morphed down ($+5^\circ$) and morphed up (-5°) configurations.

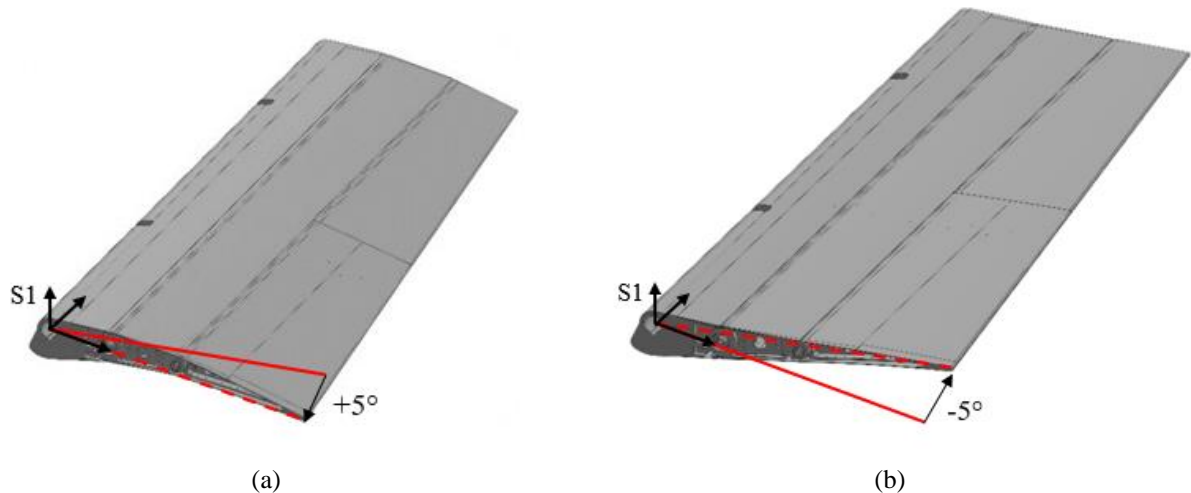
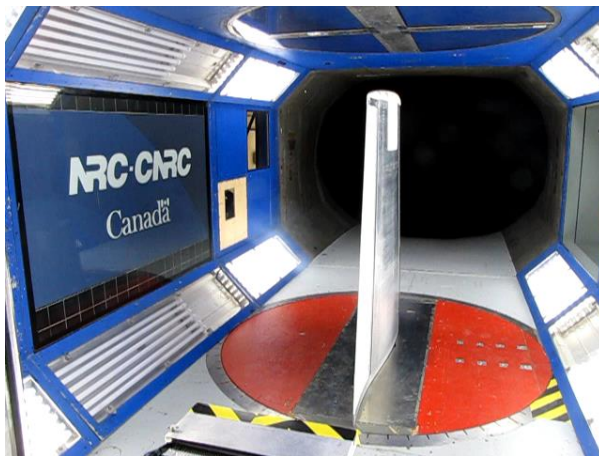
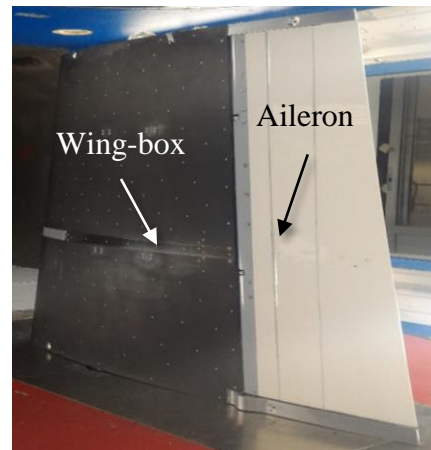


Figure 2.28. View of the aileron numerical morphed shapes: morphed down (a), morphed up (b).

During the experimental measure of the shapes, the upper aileron surface was instrumented with a set of circular retro-reflective markers, allowing direct image acquisition. The wind tunnel test sessions have covered 49 flight cases with different combinations of wing angles of attack (up to 3°), speed (from Mach 0.15 to 0.20) and aileron deflection from -3° to $+6^\circ$. For all these flight cases, the objectives of the measurement have been the delay of the flow transition from laminar to turbulent states and the validation of the morphing aileron technology from both the point of view of the functionality and the aerodynamic performance. Measures were performed by NRC (the National Research Council of Canada), Figure 2.29, via a high precision photogrammetry procedure using 3D-tracking cameras, [17]. CAD and measured shapes were overlapped as shown in Figure 2.30. White markers represent the experimental measurements points while the upper skin target geometry is represented as a continuous surface. The maximum deviation between the two shapes was computed using a least square approximation of the difference between numerical and experimental marker coordinate values. A synthetic report of the errors is reported in Table 2.5 for each configuration. Generally, a good match between the two shapes is revealed, with the exception of the TE points. The study therefore clarifies the good geometrical correlation between the target analytical shapes and the lab actual shapes. A comparison of the CFD computed aerodynamic performance, expected by a continuous and a segmented outline is planned to be performed in the next step of the research, in order to better increase the confidence with the proposed technology perspectives. However, in literature such kind of studies are widely reported and show as the two different systems behave similarly, with differences that may be assessed around 10%. In fact, it should be remarked that the region of interest is clearly turbulent and limited discontinuities cannot modify a lot the existing scenario. For instance, 0.5% c bubbles that can arise on a smooth morphing skin because of the pressure difference between the external and the internal environment have been demonstrated to produce no effect on the aerodynamic flow, [18].



(a) Subsonic wind tunnel



(b) Detail on the assembly model

Figure 2.29. Final test article with morphing wing and aileron.

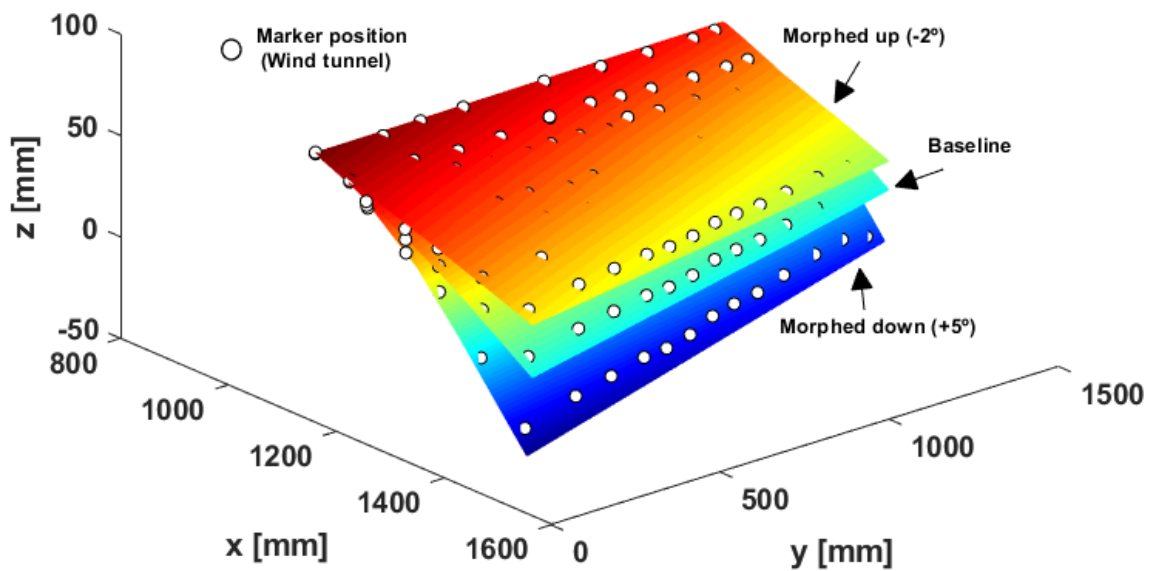


Figure 2.30. Comparison between numerical and experimental shapes (z-coordinate).

Table 2.5. Max deviation values between aileron shapes (numerical and experimental).

Configuration	Max Deviation [mm]	Locations
Morphed up	4.29	Tip Rib TE
Baseline	4.32	Tip Rib TE
Morphed down	5.65	Tip Rib TE

2.6 Conclusions

This chapter addresses the advanced design and the experimental validation of a camber morphing aileron based on electro-mechanical actuators. The morphing functionality enables more complex and efficient aerodynamic to finely control the wing lift distribution along the wing span. This leads to potential aerodynamic benefits in terms of aircraft fuel consumption throughout the flight envelope. The aileron design has involved an un-shafted servo-electro-mechanical actuation combined with a finger-like rib architecture based on double-sided guides and a fork-shaped crank. The adequacy of the adopted solution with respect to design requirements and system specifications has been proved by means of functionality and wind tunnel tests carried out on a ground demonstrator. These tests proved the device capability to reproduce target morphed shapes in a controlled manner with and without external load applied. During the design phase, the morphing system has been modelled to characterize the modal behaviour of the structure when its actuators were activated or disabled. Focus was given to the characterization of the dynamic behaviour of the device in force of the relevant impact expected to be brought to the aircraft aeroelastic stability. The analyses showed that several factors may affect the dynamic response of a morphing aileron: stiffness of the actuators, damping related to the dry friction, actuator failures, and so on. The effects induced by the power-plant activation have been also experimentally assessed in the modal shapes, highlighting an increasing of morphing modes frequencies and an overall reduction of vibration amplitudes. Generally, the remarkable amplitude reduction is linked to the increase of the generalized stiffness resulting from the blockage of the electric actuators in power on mode. The large displacements recorded in power-off mode confirms this point: they are mainly linked to quite unconstrained rotations of the rib segments around their hinges. The decrease of damping in power off mode is due to the reduction of the apparent shear forces among the elements in movement. The activation of the motors makes the structure prevents the free-movement of the consecutive rib-segments, thus magnifying the dissipation. The well-correlated modal base of the aileron can be used for further detailed aero-servo-elastic analysis targeting a thorough proof of compliance of the device with CS-25 airworthiness requirements on aeroelastic stability.

Acknowledgments

The team comprising UNINA and CIRA researchers acknowledges ETS (L'École de Technologie Supérieure), NRC (Canadian National Research Council), Bombardier Aerospace, Thales Aerospace and Finmeccanica Aircraft Division for their technical support as partners of the CRIAQ MDO-505 project.

References

- [1] Amendola, G., Dimino, I., Concilio, A., Pecora, R., Amoroso, F. and Arena, M.: *Morphing Wing Technologies Large Commercial Aircraft and Civil Helicopters – Morphing Aileron*, 547–582, Elsevier Book (2018).
- [2] Koreanschi, A., Gabor, O.S., Acotto, J., Brianchon, G., Portier, G. Botez, R.M., Mamou, M. and Mebarki, Y.: Optimization and design of an aircraft's morphing wing-tip demonstrator for drag reduction at low speeds, Part II - Experimental validation using Infra-Red transition measurement from Wind Tunnel tests, *Chinese Journal of Aeronautics*, 30(1), 164–174 (2017).
- [3] Yuanyuan, H. and Shijun, G.: Modeling and Experiment of a Morphing Wing Integrated with a Trailing Edge Control Actuation System, *Chinese Journal of Mechanical Engineering*, 25(2), 248–254 (2012).
- [4] Austin, F., Rossi, M.J., Van Nostrand, W. and Knowles, G.: Static Shape Control for Adaptive Wings, *AIAA Journal*, 32(9), 1895–1901 (1994).
- [5] Baier, H. and Datashvili, L.: Active and Morphing Aerospace Structures—A Synthesis between Advanced Materials, Structures and Mechanisms, *International Journal of Aeronautical and Space Science* 12(3), 225–240 (2011).
- [6] Botez, R.M., Tchatchueng Kammegne, M.J. and Grigorie, L.T.: Design, numerical simulation and experimental testing of a controlled electrical actuation system in a real aircraft morphing wing model, *The Aeronautical Journal*, 119(1219), 1047–1072 (2015).
- [7] Popov, A.V., Grigorie, T.L., Botez, R.M., Mamou M. and Mébarki, Y., Closed-Loop Control Validation of a Morphing Wing Using Wind Tunnel Tests, *Journal of Aircraft*, 47(4), 1309–1317 (2010).
- [8] European Aviation Safety Agency (EASA), Certification Specifications and Acceptable Means of Compliance for Large Aeroplanes – CS-25, Amendment 11, July (2011).

- [9] Botez, R.M., Koreanschi, A., Gabor, O.S., Mebarki, Y., Mamou, M., Tondji, Y., Amoroso, F., Pecora, R., Lecce, L., Amendola, G., Dimino, I. and Concilio, A.: Numerical and Experimental Testing of a Morphing Upper Surface Wing Equipped with Conventional and Morphing Ailerons, 55th AIAA Aerospace Sciences Meeting (9 - 13 January 2017 Grapevine, Texas).
- [10] Callister, W., D., J.: *Materials Science and Engineering: An introduction*, Wiley, Seventh edition, (2006).
- [11] Murray, G., Gandhi, F., and Vakis, C.: Flexible matrix composites skins for one-dimensional wing morphing, AIAA/ASME/ASHE/AHS/ASC Structure, Structural Dynamics and Materials Conference, AIAA J.2007-1737, (2007).
- [12] Viscardi, M., Arena, M., Barra, G., Vertuccio, L., Ciminello, M. and Guadagno, L.: Piezoresistive strain sensing of carbon nanotubes-based composite skin for aeronautical morphing structures, Proc. SPIE 10599, Nondestructive Characterization and Monitoring of Advanced Materials, Aerospace, Civil Infrastructure, and Transportation XII, 105991C (2018).
- [13] Amendola, G., Dimino, I., Magnifico, M. and Pecora R.: Distributed actuation concepts for a morphing aileron device, *The Aeronautical Journal*, 120(1231), 1365–1385 (2016).
- [14] MSC-Nastran®, Software Package, Ver. 2017, Reference Manual.
- [15] Arena, M., Noviello, M. C., Rea, F., Amoroso, F., Pecora, R. and Amendola, G.: Modal stability assessment of a morphing aileron subjected to actuation system failures: numerical analysis supported by test evidence, Proceedings of 2016 7th International Conference on Mechanical and Aerospace Engineering, 437–442, July 2016.
- [16] Arena M., Amoroso, F., Pecora, R., Amendola, G., Dimino, I. and Concilio, A.: Numerical and experimental validation of a full scale servo-actuated morphing aileron model, *Smart Materials and Structures*, 27(10), (2018).
- [17] Le Sant, Y., Deleglise, B. and Mebarki, Y.: An automatic image alignment method applied to pressure sensitive paint measurements, International Congress on Instrumentation in Aerospace Simulation Facilities, 1997. ICIASF '97.
- [18] Peter, F., Stumpf, E., Carossa, G. M., Kintscher, M., Dimino, I., Concilio, A., Pecora, R. and Wildschek, A., Morphing Value Assessment on Overall Aircraft Level, *Smart Intelligent Aircraft Structures (SARISTU)*, 859–871.

3. Aero-servo-elasticity of Electro-Actuated Morphing Devices

When dealing with adaptive lifting surfaces, the level of complexity of the design naturally increases as a consequence of the augmented functionality of the resulting system. For the increased elasticity and embedded electro-mechanical actuators, they are more sensitive to aero-servo-elastic issues and more likely to affect the flutter stability at A/C level. The aim of the present chapter is to detail engineering-oriented methods useful to predict the dynamic stability of servo-actuated morphing devices since the preliminary design phase. The flying system is modelled using dynamic sub-structuring: the morphing system is treated as a substructure and its modes and generalized parameters are isolated from those related the rest of the A/C which is in turn regarded as the basic system. Finally, a case-study is reported to practically show the application of the extra-modes method to the flutter clearance in the presence of critical scenarios related to malfunctions of the actuation system. The assessment of morphing wings aero-servo-elastic behaviour is a key-factor for the definition of suitable arrangements for embedded actuators.

3.1 Introduction

Within the adaptive surfaces design processes, the aeroelastic stability assessment have attracted increasingly considerable attention by many research and industrial teams. Prof. Eli Livne began his paper in 2003 writing that the aeroelasticity was still dynamic, challenging, and a key part of cutting-edge airplane technology, [1]. This is true even today, especially in the ambitious scenario of research that focuses on the design up to the actual implementation of unconventional structures on the aircraft, [2-3]. Next-generation flight technology will be actually based on “more electric” concepts to ensure benefits in terms of efficiency, weight and maintenance. Although electro-mechanical actuators are an element of innovation in next aeronautical architectures, the strategy of decentralizing the actuation systems in several areas of the structure involves carefully characterizing their effect on the dynamic stability of the entire aircraft. Recently, several studies have been addressed to investigate the aeroelastic behavior of span morphing wings. An interesting review of the progress performed in aerodynamic and aeroelastic analysis of flapping wings was presented by Shyy W., Aono H. and Chimakurthi S.K. in [4]. A variable-shaped structure in view of the fact that is characterized by a higher flexibility, certainly requires a careful study of aeroelastic performance, even greater than traditional configurations. Several basic theoretical schemes were implemented in literature to study the aeroelastic phenomena of adaptive structures. A time-domain based dynamic model has been developed by Ajaj R. M. and Friswell M. to analyse the aeroelastic behavior of compliant span morphing wings, [5]. A sensitivity study between two potential span morphing concepts was carried out: Zigzag Wingbox and the GNATSpur wing, [6-7]. The study described in [8-9] addresses flutter instability for novel morphing wing at low speed considering different morphing wing configurations for UAV. Ren H. and Zhiping Q. proposed a first-order state-space aeroelastic model to forecast transient aeroelastic responses and flutter characteristics of a variable-span wing during the morphing process, [10]. In [11], both experimental and numerical activities aimed at flutter margin evaluation were discussed for a wing demonstrator with a morphing composite upper surface as possible and fast implementation on an already existing structure. Murua J., Palacios R. and Peiro J. explored the effects of chord-wise flexibility on the dynamic stability of compliant airfoils approaching with classical two-dimensional aeroelastic model, suitably modified in order to capture time-varying camber deformations, [12]. Important both aerodynamic and aeroelastic investigations were performed in [13], achieving some key results for wing design with conformal control surfaces. A fundamental issue highlighted in [4] for further research is need to be develop bio-inspired mechanisms for the flapping wing. These mechanisms should include joints and distributed actuation to enable flapping and morphing. Most importantly, these mechanisms should be capable of mitigating wind gust. In the light of these outlooks, novel variable-shaped structures were investigated by UNINA and CIRA research teams to enable the controlled modification of the trailing edge shape for large civil aircraft applications, [14-16]. Literature works focus on 2D airfoil or deal with limited investigations on complete wings, yet simple-shaped like rectangular planforms. In the recent past, the Italian staff carried out extensive studies on dynamic aeroelastic characterisation, yet confined to full-scale wing sections for wind tunnel tests. In the current work, moving from the previous experience, the investigations are expanded to a complete wing, representative of a CS-25 class aircraft. The bio-mechanical concept, which has been described in Chapter 2, adopted to induce camber variations

encompassed segmented adaptive ribs consisting of *finger-like* segments covered by a segmented skin. The research is then developed to include safety issues, namely emphasizing the effects of failures, affecting some actuator system reference components or involving more devices. Aero-servo-elastic studies are therefore mandatory to confirm the reliability of the selected architecture as a potential candidate for a real flyable application. Engineering-oriented approaches were properly implemented, simulating the effects induced by variations of trailing edge actuators' stiffness on the aeroelastic behavior of the wing, also in correspondence of different dynamic characteristics of the trailing edge component, [17], [18]. The case study has been modelled using extra-modes method, in which the adaptive surface is treated as substructure hosted on a basic system, i.e. the aircraft, [19-20]. Morphing modes peculiar of substructure unconventional nature may be added to the extra-mode vector and their impact on the aeroelastic behavior of the overall system may be rapidly simulated. A stick-equivalent model of the reference structure was then generated in SANDY 3.0, proprietary and not yet commercially distributed set of Fortran/Matlab routine, which has been adopted for the definition of the coupled aero-structural model as well as for the solution of aeroelastic stability equations by means of theoretical modes association in frequency domain. Doublet Lattice Method was implemented for the evaluation of the unsteady aerodynamic coefficients: a suitable 2D paneling was implemented for such a purpose. Linear splines were used to interpolate modal displacements along the centers of the aerodynamic panels and generalized aerodynamic forces were evaluated with reference to the airflow conditions expected during flight envelope. Servo-actuation line malfunction scenarios were simulated to define the safety range within the certification envelope, [20]. Although the use of electro-mechanical actuators is coherent with a "more electric approach" for next-generation aircraft design, the most important drawback is associated with the actuators susceptibility to jamming. Numerical results showed that -in nominal working conditions- the aileron has no impact on aircraft aeroelastic stability. Failure checks have been then performed in order to support FHA (Fault and Hazard Analysis) specifications. Aeroelastic studies confirmed the reliability of the device, in sense that the selected architecture was demonstrated to be safe at this design stage, within the design flight conditions. Conclusions for future guidance are outlined with particular reference to design of morphing control surfaces: the results may be regarded as general guidelines the definition of the actuation chain including actuators and control lines. Because of the originality of the technological concept, there is currently not so much guidance literature on a safety-driven design of a morphing system. Moreover, for completeness, a general description of solving routine has been provided within the chapter.

3.2 Model Condensation

Even ordinary operations such as a matrix inversion can be difficult to carry out for high-order matrices, [22]. Furthermore, the dynamic characteristics of a structure are global, meaning that they refer to the overall structure configuration. In contrast, static analyses evaluate local behaviors, such as the stress concentration. Therefore, while a finite element model for static analyses requires a high number of degrees of freedom to observe local behaviors, it is appropriate to introduce a reduced model for dynamic analyses. Clearly, a reduced dynamic model should preserve a significant precision in comparison to the complete model. For this reason, its natural frequencies have to exhibit limited differences (small percentages) from those that characterize the detailed model. The condensation nodes of the morphing aileron reduced model are positioned in the same locations as the acquisition points used in the Ground Resonance Test, previously carried out within CRIAQ MD0-505 workflow. They define the geometry of the whole structure: the first row of reduction nodes is located between Hinge B0 line and Hinge B1 line, the second row between the Hinge B1 and Hinge B2 lines, and the third one is on the trailing edge tapered direction. Nodes 16 and 17, respectively located at the root and the tip of the aileron's main hinge line, were introduced to link the aileron condensed model to the wing elastic axis for the purpose of aeroelastic analysis. Figure 3.1 reports the geometric nodes in the local reference system. Regarding the z -coordinates, they all lie on the middle plane of the aileron. Each of the condensation nodes is rigidly connected to a cube of slave nodes around it by means of MPC (Multi Point Constraint) - *rbe2*, whose base is about 10 mm x 10 mm (wider dimensions could have affected the global stiffness of the aileron, increasing the frequencies of its natural modes). Usually, the dynamic analysis of an aerospace structural system is carried out by sub-structuring the system itself into many subsystems through model condensation methods, [23]. In the present work, the DMIG

matrices evaluated in the seventeen condensation nodes of the aileron's model are fully representative of the morphing aileron itself.

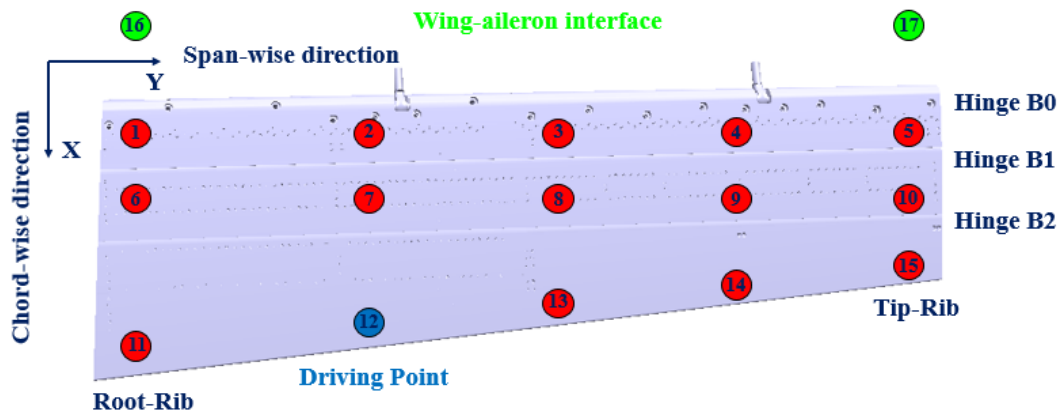


Figure 3.1. Condensation of the aileron FE model in seventeen master nodes.

The results of the numerical modal analysis that was carried out on the condensed model agree with the expectations: the morphing mode frequency is quite high, around 100 Hz. Figure 3.2 shows the first four elastic mode shapes of the condensed model, in free-free boundary conditions. Since the master condensation nodes are in the same location as the monitoring points used in the GVT, the results show that not only is the condensed model a good description of the more detailed one, but also that it agrees perfectly with the experimental results, Table 3.1.

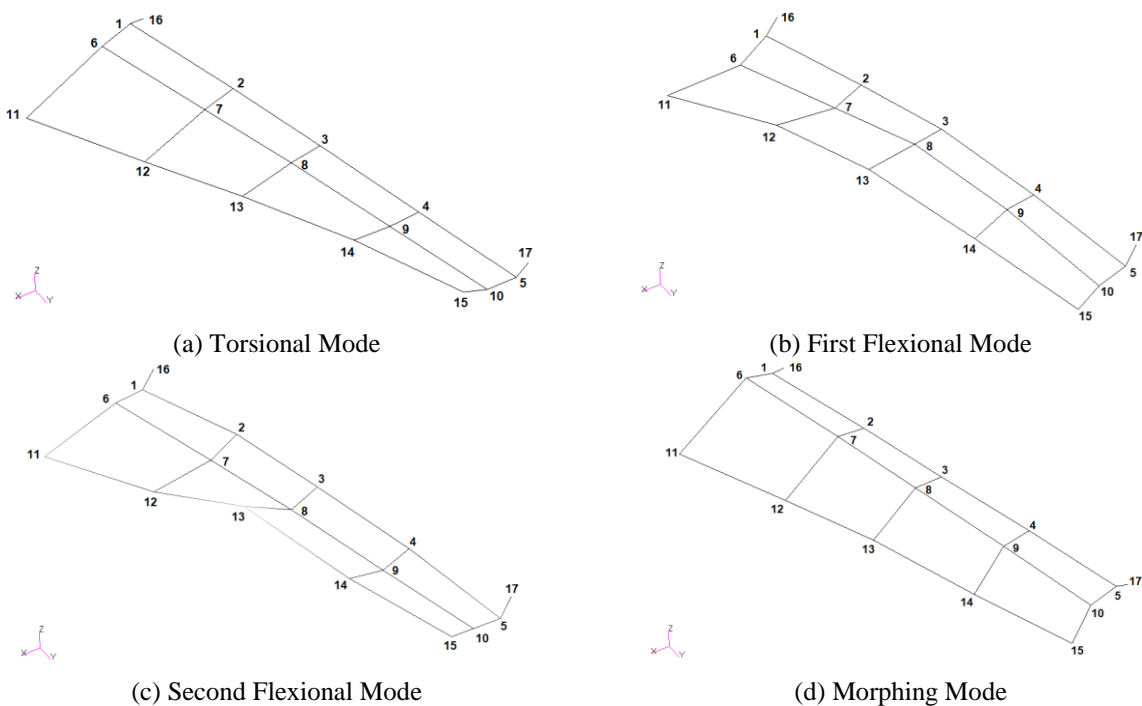


Figure 3.2. Elastic mode shapes of the aileron.

Table 3.1. Experimental-numerical frequencies correlation.

ID Mode	DMIG, f [Hz]	Test, f [Hz]	Damping [%]	Description
---------	--------------	--------------	-------------	-------------

1	60.55	57.13	4.52	<i>Torsional Mode</i>
2	68.31	66.12	1.21	<i>1st Flexural Mode</i>
3	94.30	91.98	9.28	<i>2nd Flexural Mode</i>
4	100.39	99.75	7.62	<i>Morphing Mode</i>

3.3 Aeroelastic Model

An extensive investigation was carried out to assess the impacts of the morphing aileron device on the dynamic aeroelastic stability of a reference CS-25 aircraft. The reference wing used for the aeroelastic analyses was a CS-25 aircraft wing descending from previous investigations performed in SARISTU project (Sep. 2011 – Aug. 2015) for a trade-off flutter analysis of an Adaptive Trailing Edge Device (ATED). The ATED was set up in accordance with a stick-equivalent configuration with stiffness and inertial properties condensed into lumped elements, [17]. In CRIAQ-MDO505, no aeroelastic model of the reference aircraft was elaborated due to confidentiality issues. On the other hand, within the SARISTU project, the author generated a quite complex aeroelastic model with reference to an aircraft very similar to the one addressed by CRIAQ-MDO 505; since the “SARISTU” aircraft model was not confidential, [17], [24], it was used to host the aeroleastic model of the CRIAQ aileron. In particular, studies on the aero-servo-elastic stability of the ATED were performed by the author in the framework of his Master Degree Thesis, thus opening his interest to extend the acquired methodologies to other adaptive architectures, [25]. The morphing aileron was then regarded as the substructure and the remaining part of the model as the basic system. In other terms, in order to address the impact of morphing aileron on the aeroelastic stability of a CS-25 category aircraft, the conventional aileron included in SARISTU A/C model was replaced with the morphing aileron model coming from CRIAQ-MDO505. Finally, only the right half-wing was analyzed, and two separate analyses were carried out:

- an anti-symmetric mode analysis;
- a symmetric mode analysis.

Wing dynamic model

In the SARISTU project, the stick model of wing and ATED refers to an equivalent beam representation, being all the elastic and inertial properties of the wing known (Figure 3.3). Equivalent lumped mass (/inertia) distributions were evaluated for all the structural items of the wing. Fuselage and empennages were neglected since irrelevant for the assessment of flutter instabilities potentially involving the wing; for a proper evaluation of wing elastic modes in free-free condition, their inertial contribute was however considered by means of a lumped mass. For a generic item, the inertial properties of each bay were evaluated according to the finite element model data; such properties were then assigned to a *conm2* (Concentrated Mass) element located at the centre of gravity of the bay. The *conm2* elements were rigidly connected to the closest grid of the beam-equivalent model of the relative item. Right- and left-hand models were linked to a central node (on the aircraft symmetry plane) by means of DMIG elements, which allowed to simulate the wing-fuselage interface. A *conm2* element lumping mass and plunge inertia of the aircraft body was placed at the central node. In the original model, the hinge lines of the morphing trailing edge were linked to the elastic axis of the wing by means of beam elements; pin flags were originally imposed at the end-nodes of such elements to release the rotation around the hinge lines. In the new model, the ATED is just an inertial entity and the motion of the lumped masses of its movable blocks follows solidly the rotation of Block 0 around the main hinge line.

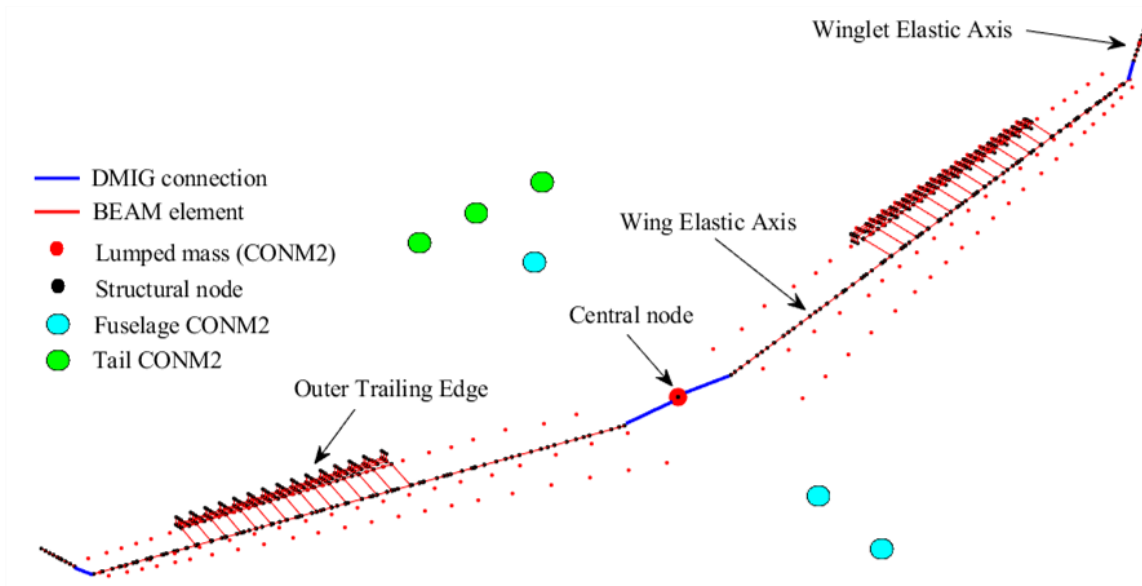


Figure 3.3. Equivalent structural model of the wing, SARISTU project.

Aileron dynamic model

As previously mentioned, the structural model representing the aileron consists of DMIG elements evaluated in the seventeen condensation nodes. This whole set of nodes is linked to specific ones on the wing elastic axis through nodes 16 and 17 (Figure 3.4), which are located at the two ends of the aileron hinge line. Therefore:

- two nodes (16* and 17*) were identified on the wing elastic axis as the closest to the orthogonal projection of (respectively) nodes 16 and 17 on the axis itself;
- two beam elements connect nodes 16 and 16*, 17 and 17*;
- bending and normal stiffness assigned to nodes 16 and 17 are equal to ten times the corresponding values in nodes 16* and 17*. Furthermore, zero torsional stiffness was assigned to nodes 16 and 17. Finally, a pin flag was imposed to release the rotational degree of freedom around the hinge line;
- a grounded spring element was applied in node 16 to simulate the torsional stiffness of the aileron around the direction of its hinge axis: such element is representative of the control circuit stiffness for the actuation of control surface.

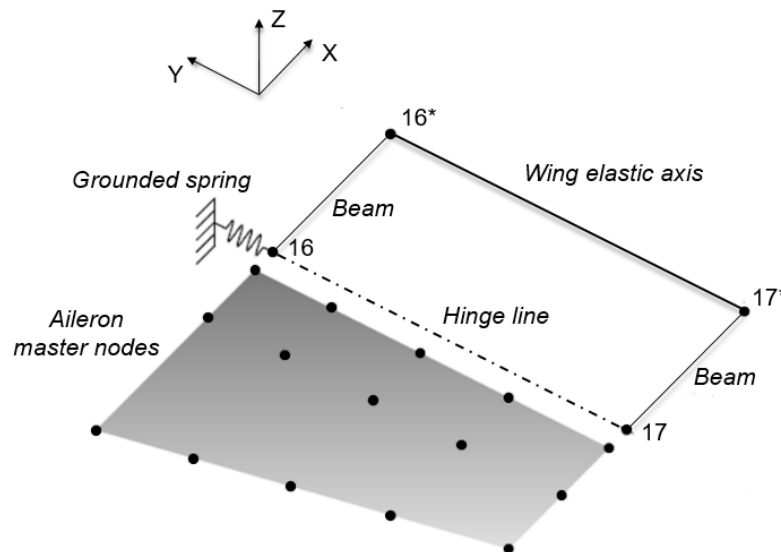


Figure 3.4. Aileron structural model: pin flags connection of the aileron hinge line to the wing elastic axis.

At each bay, support grids were added in correspondence of the hinges between blocks 1–2 and 2–3, their movement was slaved to the rotation of the grid on the primary hinge through an extra-mode accounting for the gear ratios between the rib blocks. In other terms a *multitab-like* mode was imposed at the aileron to reproduce morphing induced displacements at each rib block. The blocks 2 and 3 follow therefore the block 1 rotation according to specific kinematic gear ratios, [14]. A sketch of those connections is shown in Figure 3.5, where:

- β is the block B_i rotation;
- δ_R is the rigid rotation of B_{i+1} with respect to B_i ;
- $N = \delta_R/\beta$ is the geared ratio of B_{i+1} with respect to B_i ;
- δ_E is the elastic rotation of B_{i+1} with respect to B_i .

The total rotation δ of B_{i+1} with respect to x-axis is therefore equal to:

$$\delta = \beta + \delta_R + \delta_e \quad (3.1)$$

The deformation energy of the spring K is:

$$u = \frac{1}{2} K \delta_e^2 \quad (3.2)$$

being for (3.1):

$$\delta_e = \delta - \beta - \delta_R = \delta - \beta - N\beta = \delta - \beta(1 + N) \quad (3.3)$$

the (3.2) gives:

$$u = \frac{1}{2} K [\delta - \beta(1 + N)]^2 = \frac{1}{2} K \delta^2 - K \delta \beta (1 + N) + \frac{1}{2} K \beta^2 (1 + N)^2 \quad (3.4)$$

and the stiffness matrix of the elastic geared connection is finally obtained, as:

$$\begin{bmatrix} \frac{\partial u}{\partial \beta} \\ \frac{\partial u}{\partial \delta} \end{bmatrix} = K \begin{bmatrix} (1 + N)^2 & -(1 + N) \\ -(1 + N) & 1 \end{bmatrix} \begin{bmatrix} \beta \\ \delta \end{bmatrix} \quad (3.5)$$

This matrix has been determined according to design approach of spring-tabs applied to elevator controls of large airplanes, largely discussed by Phillips H. W. in [26]. Adjacent blocks have geared rotations due to the single-degree-of-freedom system layout. Therefore, connections between each block were made by DMIG elements built according to the geared elasto-kinematic matrix description.

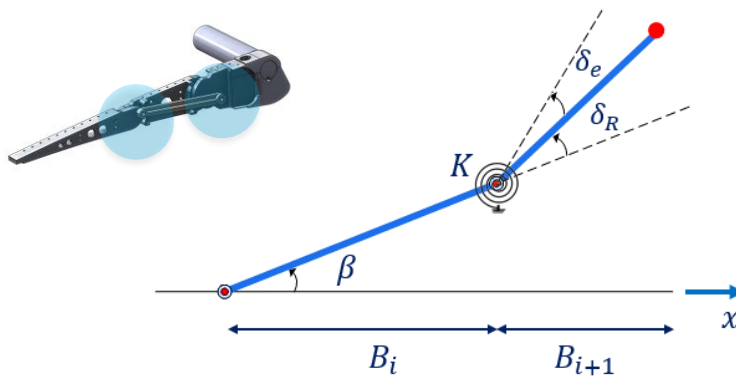


Figure 3.5. Elastic geared connection scheme.

Aerodynamic and interpolation models

The unsteady AICs (Aerodynamic Influence Coefficients) matrices were evaluated by means of the DLM (Doublet Lattice Method). The wing aerodynamic lattice was generated by meshing the wing middle plane with eight macro-panels for each half-wing, while the macro-panels themselves were meshed into elementary boxes. Higher box density was applied to the movable trailing edge, assuring mesh congruency with the structural hinged blocks of the movable trailing edge, Figure 3.6. Elastic modes of basic structure and extra-mode displacements at the center of aerodynamic boxes were obtained by means of linear spline functions attached to support-nodes of the structural model. The maximum size ΔX of the boxes along the freestream direction has been set in compliance with the Rodden's Criterion (also reported in MSC-Nastran[®] theoretical guide as a rule of good-practice to generate accurate aerodynamic mesh for doublet lattice method). Basically the adopted aero-mesh is characterized by:

$$\Delta X \ll 0.08 \frac{V_{max}}{f_{max}} \quad (3.6)$$

V_{max} and f_{max} being the maximum speed and modal frequency covered by the flutter analyses.

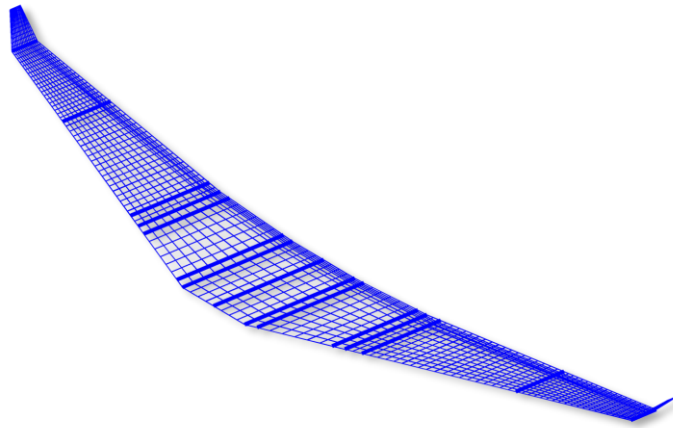


Figure 3.6. Full wing aerodynamic model.

Surface spline functions were adopted to interpolate modal displacements of the structural model grids along the centres of the aerodynamic boxes. In order to carry out the analysis on the half-wing, the aerodynamic and structural models of SARISTU wing were split in two taking advantage of the symmetry of the aircraft, and only the right half-wing models were taken into account. Therefore, symmetric and anti-symmetric modes were analyzed separately.

3.4 Aero-servo-elastic stability analysis

Aircraft flutter analysis assumptions

Flutter analyses were performed in compliance with EASA CS-25 airworthiness requirements [27], under the following assumptions:

- PK-English method, [28], with rationalization of generalized aerodynamic forces, [19], for the evaluation of modal frequencies and damping trends versus flight speed (V - g diagrams);
- Theoretical elastic modes association in the frequency range [0 – 60] Hz - elastic modes being pertinent to free-free aircraft, with only *plunge* (symmetric analysis) and *roll* (anti-symmetric analysis) motions allowed (Figure 3.7). As regards the wing, all flexional modes up to the torsional one have been considered for these analyses;
- Modal viscous damping equal conservatively to 0.015 for all the elastic modes taking into account that the most participating aileron modes are characterized by high damping values, as confirmed by GVT;

- Sea-level altitude (Density, $\rho = 1.225 \text{ Kg/m}^3$);
- Flight speed range: 0 - $1.2V_D$ ($1.2V_D = 250 \text{ m/s}$; $V_D = 206 \text{ m/s}$) in fully operative conditions; 0 - V_D ($V_D = 206 \text{ m/s}$) in case of control line failures and actuators malfunction.

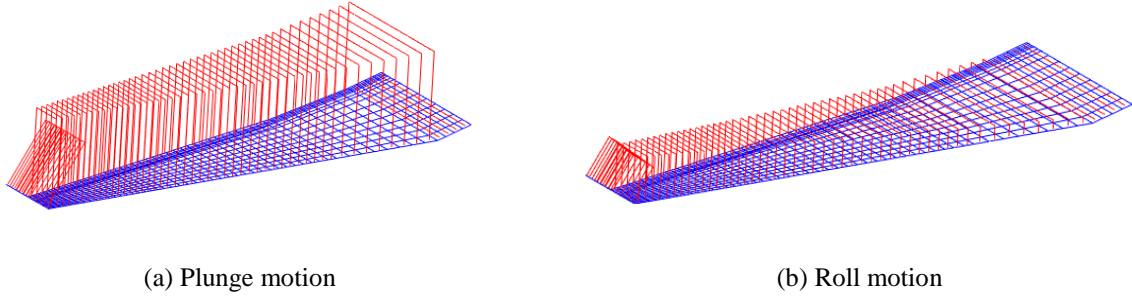


Figure 3.7. Wing rigid mode shapes.

3.4.1 Anti-symmetric aeroelastic analysis

Several cases of flutter analysis by means of in-house code were investigated, in order to comply the safety requirements imposed by the applicable aviation regulations:

- Control-line failure;
- Fully operative system;
- Actuators malfunction - failure;
- Actuators malfunction - jamming.

The analysis of the above cases is outlined in detail in the following sections.

Control-line failure

The roll-control line failure case was simulated by removing the torsional spring in node 16 (see Figure 3.4). As expected, the first modal shape (at nearly 0 Hz) represents the aileron's failure mode, shown in Figure 3.8(a). It clearly represents the fundamental mode of a control surface, which freely rotates around its own hinge axis. Figure 3.8(a) represents the displacements induced by the morphing extra-mode along the aero-mesh boxes. Therefore, this analysis may be a verification of the model goodness with respect to the right way of simulating the kinematics. On the other side, Figure 3.8(b) shows the resulting *V-g* plot, in which frequency and damping for each mode are plotted as a function of the speed. At the right of the graph, the frequencies of the first eleven modes are listed. Clearly, the speed at which one of the damping curves becomes positive identifies a flutter condition. Examining the curves, flutter occurs at 202.4 m/s (81% of $1.2V_D$) in the control-line failure condition. In this case, the instability was generated by a typical coupling mechanism between the aileron fundamental mode with the wing bending mode. This configuration could not be accepted, since the relative flutter speed was smaller than $1.2V_D$, and for such reason the aileron needed to be balanced. A control surface is said to be 100% balanced if, in absence of any friction, its horizontal position is of stable equilibrium. Or alternatively, for any little deflection imposed, a 100% balanced control surface deflects back to a horizontal position.

The unbalancing static moment of the single aileron S is:

$$S = m_{tot} * d = 1.693 \text{ Kgm} \quad (3.2)$$

Two balancing masses were added on nodes 16 and 17 and positioned beyond the hinge line (Figure 3.9) in such a way that the distance from it was fixed to $d_{bal} = 0.20 \text{ m}$ (slightly more than the aileron's half chord length). Since:

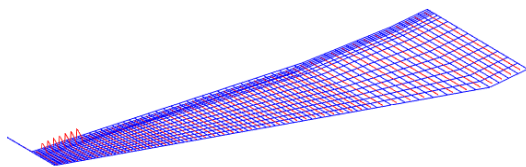
$$\chi * m_{tot} * d = m_{bal} * d_{bal} \quad (3.3)$$

$$\chi = \frac{m_{bal} * d_{bal}}{m_{tot} * d} \quad (3.4)$$

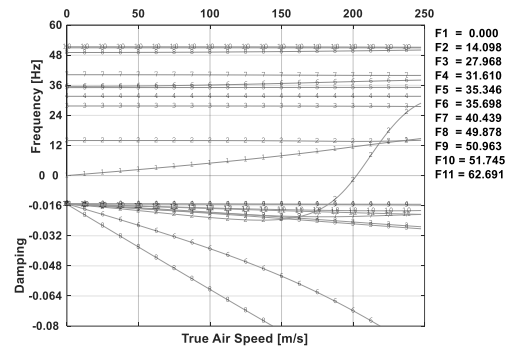
it was found that for a degree of balance χ equal to 47% (balancing mass equal to 2*2.0 Kg) no flutter occurs in the range of velocities of interest. A first estimation of the torsional spring stiffness was performed considering that:

$$f = \frac{1}{2\pi} \sqrt{\frac{K_G}{I}} \quad (3.5)$$

and setting the aileron harmonic frequency at $f = 20$ Hz, which is an usual value for the addressed transportation aircraft category. I stands for the inertia of the movable trailing edge around its hinge line, corresponding to the generalized mass of its fundamental mode. The latter (M_G) was known from a modal analysis carried out beforehand and it resulted to be about 0.67 Kg m^2 . The condition $f = 0$ Hz was taken in account to simulate actuators failure; in such a case the aileron harmonic coincides with its fundamental (free rigid rotation around the hinge line).



(a) Fundamental aileron mode



(b) V-g plot

Figure 3.8. Control-line failure case.

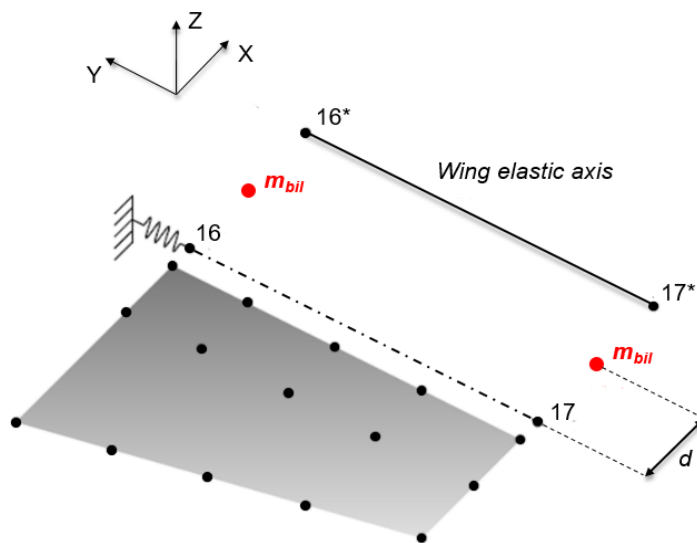


Figure 3.9. Aileron structural model - Balancing: $\chi = 47\%$; $m_{bil} = 2*2.0$ Kg, $d = 0.20$ m.

Nominal condition

In the fully operative configuration, aileron stick-fixed harmonic exhibits an elastic frequency due to the torsional stiffness of the command line. Figure 3.10(a) shows the aileron harmonic mode interpolated on the aerodynamic lattice, while Figure 3.10(b) reports the V - g plot in this condition. The plot shows that flutter occurs in the range of velocities of interest, even though the corresponding speed results to be very close to the upper limit of the range. Therefore, it was necessary to increase the degree of mass balance up to 105%, corresponding to $m_{bil} = 2 * 3.55 \text{ Kg}$ and $d = 0.25 \text{ m}$. In this way, flutter was shifted outside the range of interest.

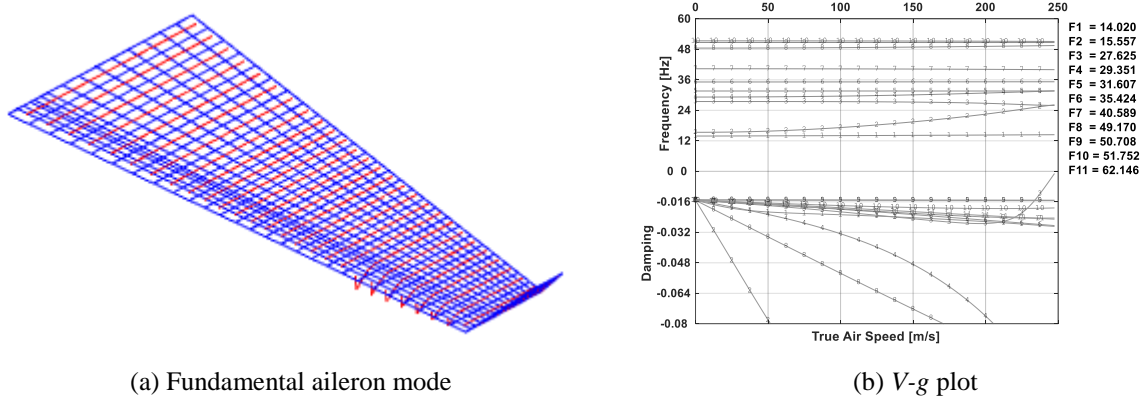


Figure 3.10. Aileron structural model - Balancing: $\chi = 47\%$; $m_{bil} = 2 * 2.0 \text{ Kg}$, $d = 0.20 \text{ m}$.

3.4.2 Symmetric aeroelastic analysis

The same cases have been investigated concerning the symmetric modes analysis. Clearly, the roll-control line failure case was not considered, since it is a not physical condition: in case of failure of the control-line, right and left ailerons deflect always in an anti-symmetric way.

Nominal condition

The analysis was performed on the balanced aileron (degree of balance = 105%), with the control-line torsional spring stiffness equal to $K_c = 2 * 10^4 \text{ Nm/rad}$. The harmonic frequency has been detected about 15.5 Hz, with a generalized mass equal to 0.228 Kg m^2 (Figure 3.11(a)). This harmonic mode couples with the wing second flexion one ($f = 21.6 \text{ Hz}$, Figure 3.11(b)) at a speed of 152.6 m/s thus generating flutter at 61% of $1.2V_D$ (Figure 3.12). As a result of an iterative analysis carried out in order to shift the detected flutter outside the range of velocities of interest, the torsional spring stiffness was decreased to $1.2 * 10^4 \text{ Nm/rad}$ (which caused a reduction in the harmonic frequency to 13.3 Hz), while the degree of balance was increased to 136% (meaning two masses of 4.6 Kg with a fixed distance from the hinge line equal to 0.25 m). No flutter up to $1.2V_D$ was detected after these changes were applied, Figure 3.13. In this case, a decrease in stiffness was required to have a positive impact on flutter. In fact, a more rigid system can be unstable from the aeroelastic standpoint. The command harmonic always increases in frequency with the increase in speed. Since in fully operative condition it couples with a bending mode at a frequency $f_b = 21.6 \text{ Hz}$, the gap between harmonic and bending frequency was enlarged by shifting the first one towards smaller values. Another solution could have been the shifting of the harmonic frequency towards a value higher than f_b . However, this could be dangerous in the morphing aileron case, since by increasing the torsional spring stiffness, new pseudo-harmonic modes of rotation around the secondary hinges may appear. Finally, having modified the degree of balance, it was necessary to verify that flutter was still not occurring considering the *anti-symmetric mode association* in nominal conditions, Figure 3.14.

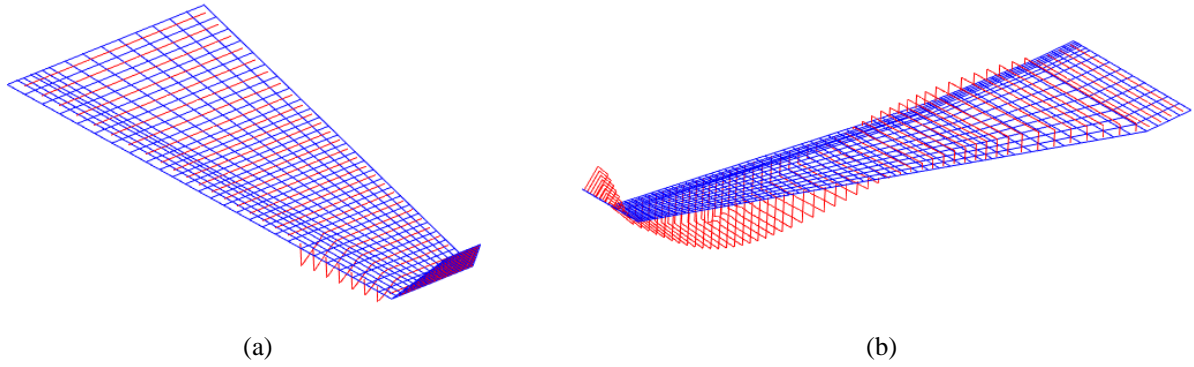


Figure 3.11. Modal coupling, nominal condition: (a) Aileron harmonic ($f = 15.5$ Hz, $M_G = 0.228$ Kg·m²), (b) Wing second bending ($f = 21.6$ Hz, $M_G = 6.06$ Kg·m²).

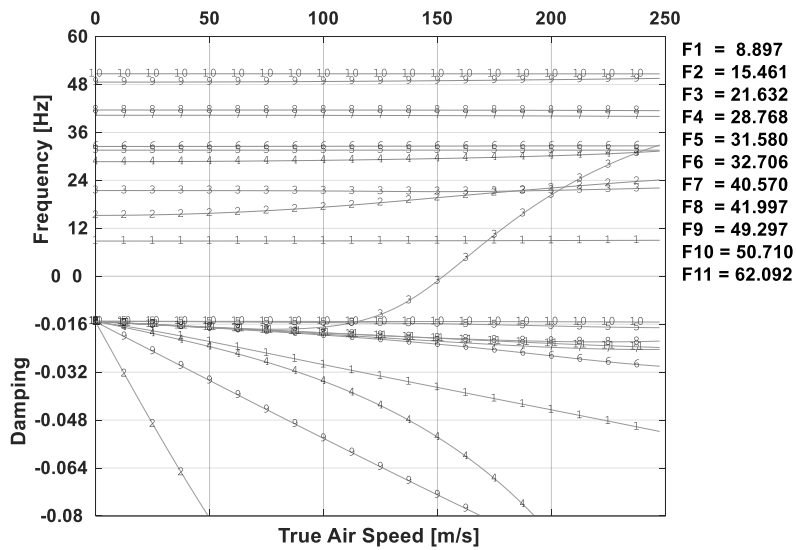


Figure 3.12. Fully operative condition, symmetric modes association, V-g plot.

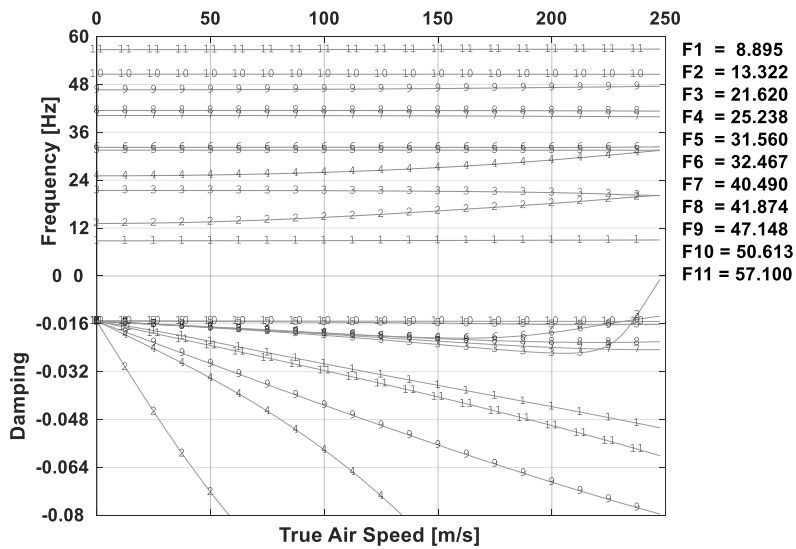


Figure 3.13. Fully operative condition, symmetric modes association, V-g plot, $\chi = 136\%$.

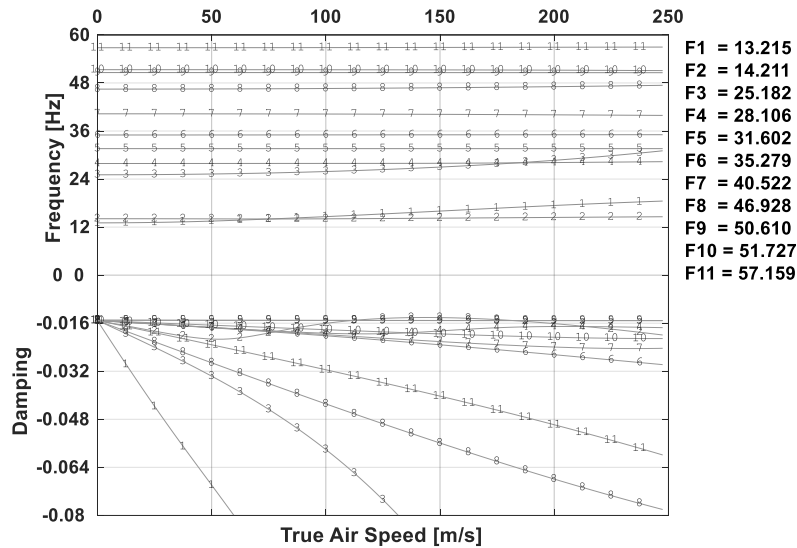


Figure 3.14. Fully operative condition, anti-symmetric modes association, V-g plot, $\chi = 136\%$

Actuators failure scenario

The actuator failure configurations were simulated calculating the DMIG matrices by means of new FE models. Starting from the one simulating the fully operative system, a single actuator failure was simulated assigning null stiffness to the corresponding grounded spring. In fact, as described in Chapter 2, each actuator was modelled through a tuned torsional spring, to be able to quickly modify the local stiffness value. In fact, a simple but reliable way of representing complex mechanisms, is certainly a strategic choice at the design stage. Both single actuator failure cases and more critical situations in which two actuators fail simultaneously were taken into account. After having run the modal analysis *SOL 103* [29], it was possible to see the variation of both morphing and torsional mode frequencies throughout the different configurations. The results are reported in Table 3.2, in which the number identifying each one of the three actuators was assigned as shown in Figure 3.15. One would expect the morphing mode frequency to be zero in case 7: failure of all the actuators. Instead, the corresponding frequency is kept high by the internal stiffness due to the torsional springs between adjacent rib blocks (whose function is to prevent free-plays due to tolerances). As shown in Table 3.2, none of the frequencies decreases under 60 Hz, but it was still essential to run the analyses. In fact, even if the modal frequencies were high enough to not be critical theoretically speaking, they could still induce new modal shapes in the range 0–60 Hz that may cause flutter. EASA regulations impose that in case of actuator failures the range of velocities for flutter clearance must be 0 - V_D . The malfunction scenarios for both anti-symmetric and symmetric modes have been investigated in order to verify the robustness of the system: no flutter occurs in the selected range of velocities in the case of first actuator failure. Instead, looking at simultaneous failure of two and three actuators, flutter occurs well before V_D , Figure 3.16. Although, it must be noticed that EASA CS-25 regulations do not require clearance up to V_D for double/triple failures. For greater completeness, the graph also shows the cruise speed value, imposing it equal to $V_C = 0.8V_D = 164.8$ m/s (according to paragraph 25.335 (b) of the EASA CS-25 regulation).

Table 3.2. Actuator failure impact on dynamic response [0; 100 Hz], anti-symmetric analysis.

Case ID	Torsional Frequency [Hz]	Morphing Frequency [Hz]
First actuator	59.09	92.40
Second actuator	59.64	92.12

Third actuator	59.99	91.80
First & Second	58.68	87.41
First & Third	58.96	87.80
Second & Third	59.48	87.17
Full failure	58.53	83.75

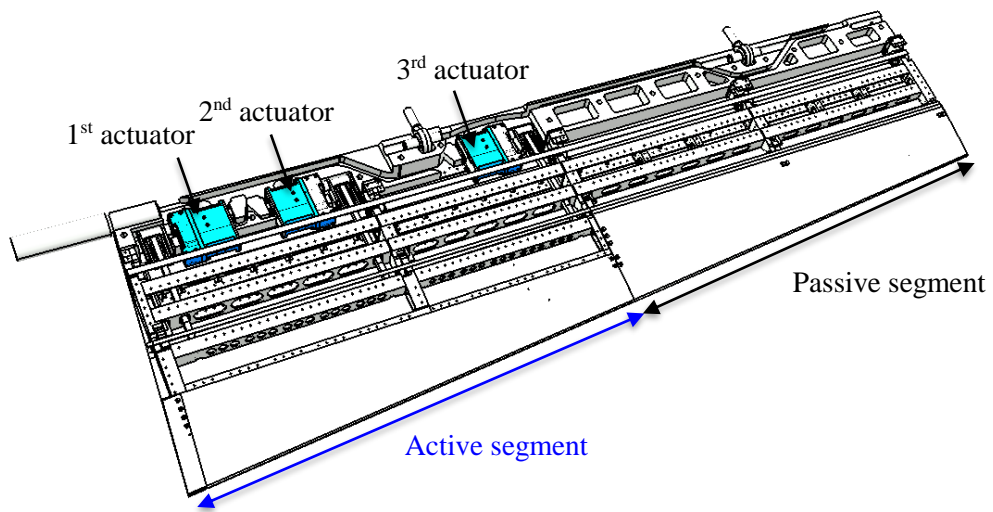


Figure 3.15. 3D CAD of the entire aileron, hidden upper skin.

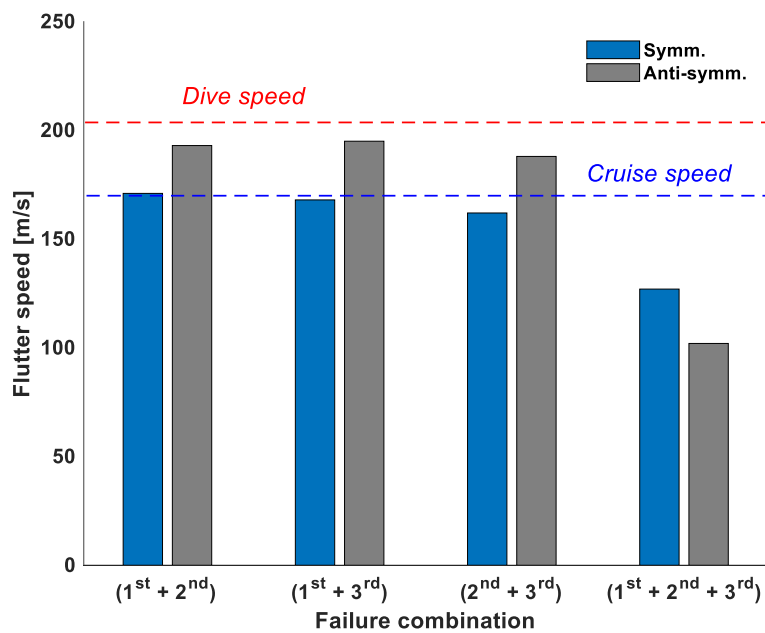


Figure 3.16. Flutter velocity trend - multiple failure cases.

Actuators jamming condition

A particular attention has been given to assess jamming of the actuators. Such malfunction was simulated by re-calculating the DMIG matrices of FE models in which a very high stiffness ($k_a = 10^6$ Nm/rad) was assigned to the corresponding grounded spring (see paragraph relative to finite element modelling). The investigated cases are the following:

- Case 1: Symmetric modes, $K_c = 12000$ Nm/rad, $\chi = 136\%$, jamming actuator 1;
- Case 2: Symmetric modes, $K_c = 12000$ Nm/rad, $\chi = 136\%$, jamming actuator 2;
- Case 3: Symmetric modes, $K_c = 12000$ Nm/rad, $\chi = 136\%$, jamming actuator 3;
- Case 4: Anti-symmetric modes, $K_c = 12000$ Nm/rad, $\chi = 136\%$, jamming of the actuator that gives the smallest flutter speed in the first three cases.

In order to do this, the relative rotation of hinged elements belonging to the actuation chain was counteracted by stiff torsion springs. Anyway, no criticalities were detected in case of jamming of any of the actuators (Figure 3.17); this outcome found an explanation by evaluating that in case of actuators “locking” the morphing mode exhibits a frequency increases and does no longer participate to critical coupling mechanisms involving lower frequency modes such as aileron’s harmonic and wing flexion. Nevertheless, jamming event, which is one of the main drawbacks associated with the use of electro-mechanical actuators, could result in different consequences on available flight control authority and fault duration. An excessive static resistive torque of the actuation components, if extended over time, can degenerate into their sudden failure. Such stiffness increase can modify the load distribution and cause the failure of some actuation systems in turn leading to unstable coupling mechanisms involving lower frequencies modes as the wing bending and other low-generalized mass secondary modes.

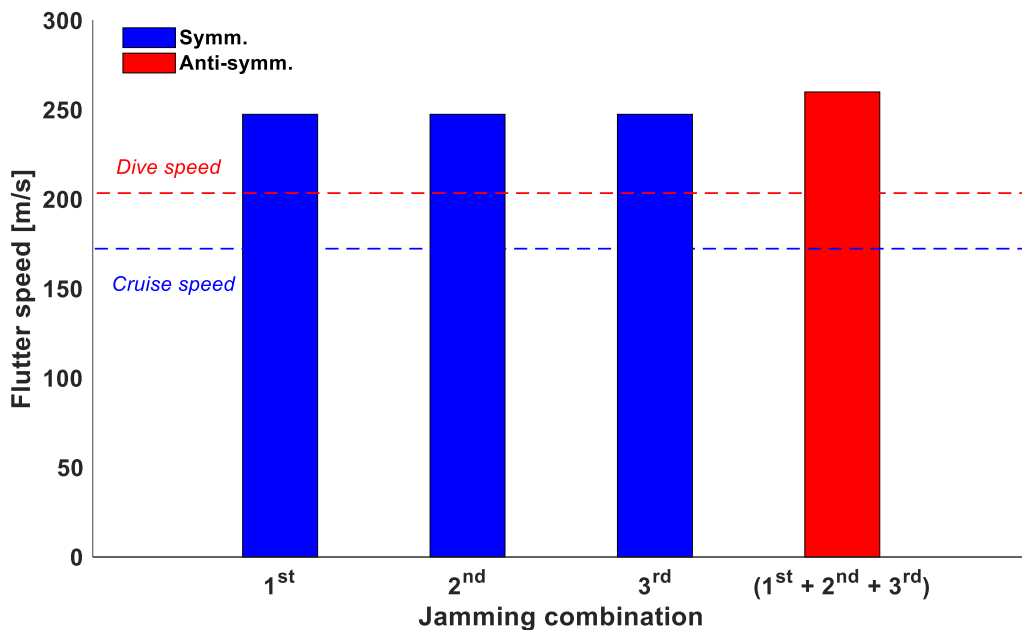


Figure 3.17. Flutter velocity trend - multiple jamming cases.

3.5 Conclusions

In the framework of the CRIAQ-MDO505 project an innovative morphing aileron was designed, manufactured and tested. This device was conceived with reference to a typical long-range reference aircraft with the objective of enhancing wing efficiency, as well as of maximizing roll control effectiveness, through the controlled camber variation of the trailing edge tip all along the flight path. The classical aileron architecture was replaced by a robotized structure moved by three rotary actuators and characterized by a multi-box arrangement; upon actuation, the external shape of the aileron morphs thanks to the relative rotation among adjacent boxes. To prove the compliance of the new technology with the basic airworthiness

requirements in terms of aeroelastic stability, flutter analyses were carried out while considering the coupling of typical aircraft modes with those related to the morphing architecture. Due to the particular unconventional design of the aileron, its FE-based dynamic model was preliminarily validated by means of ground vibration tests carried out on a true-scale prototype in free-free conditions; the validated model was then added to the aircraft aeroelastic model and flutter analyses took place in correspondence of relevant operative configurations. Minimum mass balancing was at first determined by imposing aircraft flutter clearance up to dive speed in case of roll-control line failure. Nominal functioning cases were then addressed showing the absence of any flutter in the certification envelope; this proved that as long as the morphing system works according to its design specs, no aeroelastic instability is expected to occur well beyond the aircraft dive speed. The robustness of the system was then investigated with reference to failure and jamming conditions. No criticalities were found up to dive speed both in case of single actuator failed or jammed. Although not prescribed by airworthiness regulations, multiple failures were anyway investigated due to the deeply unconventional arrangement of the control surface; obtained results showed that -even in the extremely remote case of two or three actuators failed- a braking/damper system (providing only +0.7% modal damping increase) is more than enough to assure flutter clearance up to V_D . This proved a very good robustness of the conceived device also with reference to possible malfunctions bringing to the loss of the authority of one or more actuators dedicated to morphing. Single/multiple jamming cases resulted practically irrelevant from the aeroelastic standpoint; in case of jamming the *unconventional* modes related to the multi-box structural arrangement show a relevant increase of their frequency and do not participate in critical coupling mechanisms involving (*conventional*) lower frequencies modes such as aileron's harmonic and wing bending.

Appendix 1. Routine for aero-servo-elastic analyses

SANDY 3.0 is a proprietary non-commercial code with the intent of providing an excellent and reliable tool for static and dynamic aeroelastic and aero-servo-elastic analysis of aircraft. Rational approaches and validated numerical methods, compliant with the CS-25 and CS-23 EASA standards, have been implemented in a multidisciplinary computational environment, able to accomplish the following main tasks:

- Generation of A/C dynamic model (structural and inertial models);
- Generation of A/C aerodynamic model;
- Generation of accurate transfer matrices, interfacing between dynamic and aerodynamic models;
- Evaluation of A/C static and dynamic acceleration and loads response due to flight and ground manoeuvres and/or gust;
- Evaluation of A/C static and dynamic acceleration and loads response to movable lifting surfaces deflections imposed by mechanical and/or electro-mechanical control circuits;
- Evaluation of divergence, control reversal and flutter speeds.

The computational tools and the numerical methods therein implemented, assure fast analyses aimed also at investigating the influence of several design parameters on the A/C aeroelastic behaviour. In other terms, the code permits a fast sensitivity aeroelastic analysis with respect to variations of some A/C components structural and dynamic properties, including also the integrated control circuits. The highly efficient computational structure is based on intercommunicating routines, running in a common software environment (Visual Fortran / Matlab) and properly organized in three macro-modules:

- Dynamic module;
- Aerodynamic module;
- Aeroelastic module.

The dynamic module includes a generator of A/C structural and inertial models and an internal FE solver for the evaluation of A/C modal parameters. In order to perform reliable modelling in reasonable time, only two typologies of elements are available:

- Simple one-dimensional elements (beam, rod, rigid-link, spring);

- DMIG (Direct Matrix Input at Grids) elements for a correct evaluation of stiffness and inertial properties of those parts requiring a more sophisticated representation.

DMIG elements may be imported from commercial FE softwares (e.g., MSC Nastran® [29]); the same applies to A/C modal parameters (mode shapes, frequencies, generalized masses, and damping) that, moreover, may be imported from GVT experimental data. In addition to the A/C structure normal modes, the dynamic module allows for including extra-modes correlated to the movable surfaces, in order to simulate loads alleviation systems, based on the use of those devices in feed-back with A/C kinematic parameters (acceleration, velocity, displacement), and/or perform fast instability analyses in presence of powered or fly-by-wire controls.

The aerodynamic module is characterized by a generator of aerodynamic models, coupled to an internal solver for the evaluation of modal pressure distributions by means of consolidated numerical methods, like the Doublet Lattice Method (DLM). More in detail, the module provides the capability of generating three-dimensional compressible aerodynamic models, and the possibility of performing local corrections in the pressure distributions to take into account the effects of the movable surfaces aerodynamics (as recommended by FAA AC 25.629-1A paragraph 6).

The aeroelastic module is constituted of routines for:

- Interpolating modal displacements on the aerodynamic lattice (matching routines implementing 3D-spline methodologies);
- Evaluating generalized aerodynamic pressures/forces and steady/unsteady aerodynamic influence coefficients;
- Solving the aeroelastic equations describing the A/C response and the instabilities identification.

The developed tool allows for managing multi-parametric analysis in a more fluent way compared to commercial standards, thus leading to relevant computational time savings. Engineering-oriented results can be achieved by solving the classic aeroelastic equations respect to the speed (dynamic pressure) in order to find the best combination between crucial design parameters like for example balancing ratio or control line stiffness. Software performance has been actually positively tested during the aeroelastic certification process of a wide set of commercial aircraft with respect to the stability demonstration at both theoretical and experimental levels [30-32]. A wide use has been found by the UNINA research team with special regards to the design of unconventional structures, motivating therefore them to expand the potentiality of such routine to very complex aeroelastic issues. The numerical processing of data referring to a multi-block structure required the adaptation of the software to new design requirements. Reliable procedures for quick consideration of all-move systems are necessary in the current research framework, increasingly aimed at executive design and demonstration in the wind tunnel and in flight. The morphing device is often treated as a substructure and the aircraft (A/C) as the basic system on which the device is installed. The dynamic sub-structures approach based on extra-modes definition can be well adopted when using experimental modes, [33]. The sub-structures generation is useful also in order to reduce the impact on already performed analysis due to the several changes that may occur during the design of an aircraft. Substructure's contribute to the aeroelastic response of the global system is expressed in terms of generalized parameters pertinent to additional and strategically defined modes capturing the substructure dynamics, [34]. Particular attention has been given to explore the feasibility to investigate the A/C flutter taking into account typical nonlinearities in correspondence of control surface: free-play, the bilinear stiffness due to the presence of spring tab or the distributed non-linearity due to the mechanical joints, [35].

Acknowledgments

The author and the team comprising UNINA and CIRA researchers acknowledges ETS (L'École de Technologie Supérieure), NRC (Canadian National Research Council), Bombardier Aerospace, Thales Aerospace and Finmeccanica Aircraft Division for their technical support as partners of the CRIAQ MDO-505 project.

References

- [1] Livne, E.: Future of Airplane Aeroelasticity, *Journal of Aircraft*, 40(6), 1066–1092 (2003).

- [2] Kota, S., Flick, P. and Collier, F.: Flight testing of the FlexFloil™ adaptive compliant trailing edge, 54th AIAA Aerospace Sciences Meeting, San Diego, United States, January (2016).
- [3] Hetrick, J., Osborn, R., Kota, S., Flick, P. and Paul, D.: Flight Testing of Mission Adaptive Compliant Wing, 48th AIAA/ASME/ASCE/AHS/ASC Structures, Structural Dynamics, and Materials Conference, Structures, Structural Dynamics, and Materials and Co-located Conferences, <https://doi.org/10.2514/6.2007-1709>.
- [4] Shyy, W., Aono, H., Chimakurthi, S.K., Trizila, P., Kang, C.-K., Cesnik, C.E.S. and Liu, H.: Recent Progress in Flapping Wing Aerodynamics and Aeroelasticity, *Progress in Aerospace Sciences*, 46(7), 284–327 (2010)
- [5] Ajaj, R.M. and Friswell, M.I.: Aeroelasticity of Compliant Span Morphing Wings, *Smart Materials and Structures*, 27(10), (2018), <https://doi.org/10.1088/1361-665X/aad219>.
- [6] Ajaj, R.M., Saavedra Flores, E.I., Friswell, M.I., Allegri, G., Woods, B.K.S., Isikveren, A.T. and Dettmer, W.G.: The Zigzag wingbox for a span morphing wing, *Aerospace Science and Technology*, 28(1), 364–375 (2013), 10.1016/j.ast.2012.12.002.
- [7] Ajaj, R.M., Saavedra Flores, E.I., Friswell, M.I. and DiazDelaO, F.A.: Span morphing using the compliant spar, *Journal of Aerospace Engineering*, 28(4), 1-13 (2015), 10.1061/(ASCE)AS.1943-5525.0000442.
- [8] Sabri, F., Meguid, S. and Lakis, A.: Modeling Flutter Response of a Flexible Morphing Wing for UAV, 53rd AIAA/ASME/ASCE/AHS/ASC Structures, Structural Dynamics and Materials Conference, Structures, Structural Dynamics, and Materials and Co-located Conferences, (2012), <https://doi.org/10.2514/6.2012-1707>.
- [9] Sabri, F. and Meguid, S. A.: Flutter boundary prediction of an adaptive morphing wing for unmanned aerial vehicle, *International Journal of Mechanics and Materials in Design*, 7(4), 307–312 (2011), 10.1007/s10999-011-9169-z.
- [10] Ren, H. and Zhiping, Q.: Transient aeroelastic responses and flutter analysis of a variable-span wing during the morphing process, *Chinese Journal of Aeronautics*, 26(6), 1430–1438 (2013).
- [11] Koreanschi, A., Henia, M.B., Guillemette, O., Michaud, F., Tondji, Y., Sugar Gabor, O., Botez, R. M. and Flores Salinas, M.: Flutter Analysis of a Morphing Wing Technology Demonstrator: Numerical Simulation and Wind Tunnel Testing. *INCAS Bulletin* 8(1), 99–124 (2016).
- [12] Murua, J., Palacios, R. and Peiró, J., Camber Effects in the Dynamic Aeroelasticity of Compliant Airfoils, *Journal of Fluids and Structures*, 26(4), 527–543 (2010).
- [13] Sanders, B., Eastep, F. E. and Forster, E.: Aerodynamic and Aeroelastic Characteristics of Wings with Conformal Control Surfaces for Morphing Aircraft”, *Journal of Aircraft*, 40(1), 94–99 (2003).
- [14] Amendola, G., Dimino, I., Concilio, A., Pecora, R., Amoroso, F. and Arena, M.: Morphing Wing Technologies Large Commercial Aircraft and Civil Helicopters – Morphing Aileron, 547–582, Elsevier Book (2018).
- [15] Arena M., Amoroso, F., Pecora, R., Amendola, G., Dimino, I. and Concilio, A.: Numerical and experimental validation of a full scale servo-actuated morphing aileron model, *Smart Materials and Structures*, 27(10), (2018).
- [16] Arena, M., Palumbo, R., Pecora, R., Amoroso, F., Amendola, G. and Dimino, I.: Flutter clearance investigation of camber-morphing aileron tailored for a regional aircraft, *Journal of Aerospace Engineering*, 32(2), (2019), 10.1061/(ASCE)AS.1943-5525.0000973.
- [17] Pecora, R., Magnifico, M., Amoroso F. and Monaco, E.: Multi-parametric flutter analysis of a morphing wing trailing edge, *The Aeronautical Journal*, 118(1207), 1063–1078 (2014).
- [18] Arena M., Concilio A. and Pecora, R.: Aero-servo-elastic design of a morphing wing trailing edge system for enhanced cruise performance, *Aerospace Science and Technology (final review)*.
- [19] Broadbent, E.G., *Flutter and Response Calculations in Practice*, AGARD Manual on Aeroelasticity, 3, NASA (1963).
- [20] Buxton, G.H.L. and Sharpe, G.D.: The Effect of Tab Mass-balance on Flutter, Part I, R. & M. No. 2418, A. R. C. Technical Report (1951).
- [21] Albano, E. and Rodden, W.P.: A Doublet-Lattice Method for Calculating Lift Distributions on Oscillating Surfaces in Subsonic Flows, *AIAA Journal*, 7: 279–285 and 7: 2192 (1969).
- [22] Harder, R.L. and Desmarais, R.N.: Interpolation Using Surface Splines, *Journal of Aircraft* 9(2), 189–191 (1972).
- [23] Arena, M., Pecora, R., Amoroso, F., Noviello, M. C., Rea, F. and Concilio, A.: Aeroelastic analysis of an adaptive trailing edge with a smart elastic skin, In *AIP Conference Proceedings* 1884(1), (2017), <https://doi.org/10.1063/1.5002521>.
- [24] Arena, M.: Aeroelastic stability analysis of a morphing wing trailing edge for a CS-25 category aircraft, Master thesis, Università degli Studi di Napoli “Federico II” (2014).
- [25] Phillips, H.W.: Application of Spring Tabs to Elevator Control, Report no. 797, NACA (1944).
- [26] European Aviation Safety Agency (EASA), *Certification Specifications and Acceptable Means of Compliance for Large Aeroplanes – CS-25, Amendment 11*, July (2011).
- [27] Rosenbaum, R. and Vollmecke, A.A.: Simplified flutter prevention criteria for personal type aircraft, *Airframe and Equipment Engineering*. Report no. 45. NACA (1955).
- [28] MSC-Nastran®, Software Package, Ver. 2017, Reference Manual.
- [29] Pecora, R., Pecora, M. and Lecce, L.: Flutter Certification of SKYCAR Aircraft: Rational Analysis and Flight Tests, *Proceedings of the 3rd CEAS Air&Space Conference*, Venice, Italy, September (2011).

- [30] Pecora, R., Amoroso, F. and Lecce, L.: Effectiveness of Wing Twist Morphing in Roll Control, *Journal of Aircraft*, 49(6), 1666–1674 (2012).
- [31] Pecora, R., Amoroso, F., Palumbo, R., Arena, M., Amendola, G., Dimino, I.: Preliminary aeroelastic assessment of a large aeroplane equipped with a camber-morphing aileron”, *Proceedings of SPIE - The International Society for Optical Engineering* (2017).
- [32] Pecora, M. and Pecora, R.: Application of the Extra-Modes Method to the Aeroelastic Analysis of Morphing Wing Structures, *Morphing Wing Technologies Large Commercial Aircraft and Civil Helicopters*, 429–450 (2017).
- [33] Belardo, M., Pecora, M. and Paletta, N. (2013), “Flutter analysis with hydraulic servos -a technique for modeling actuator dynamics”, *SAE 2013 AeroTech Congress and Exhibition, AEROTECH*.
- [34] Picardi, F. M., Paletta, N., Belardo, M. and Pecora, M. (2014), “Fast automatic procedure for flutter-clearance assessment when in the presence of significant structural damage”, *Journal of Aerospace Engineering*, 27(6).

4. Electro-actuation System Strategy for a Morphing Flap

Within the framework of the Clean Sky-JTI project the design and technological demonstration of a novel wing flap architecture were addressed. Research activities were carried out to substantiate the feasibility of morphing concepts enabling flap camber variation in compliance with the demanding safety requirements applicable to the next generation green regional aircraft. The driving motivation for the investigation on such a technology was found in the opportunity to replace a conventional double slotted flap with a single slotted camber-morphing flap assuring similar high lift performances -in terms of maximum attainable lift coefficient and stall angle- while lowering emitted noise and system complexity. The actuation and control logics aimed at preserving prescribed geometries of the device under variable load conditions are numerically and experimentally investigated with reference to an "iron-bird" demonstrator. The actuation concept is based on load-bearing actuators acting on morphing ribs, directly and individually. The adopted un-shafted distributed electro-mechanical system arrangement uses brushless actuators, each rated for the torque of a single adaptive rib of the morphing structure. An encoder-based distributed sensor system generates the information for appropriate control-loop at the same time, monitors possible failures in the actuation mechanism. Further activities were then addressed in order to increase the TRL of the validated architecture within Airgreen 2. Relying upon the already assessed concept, an innovative and more advanced flap device was designed in order to enable up three different morphing modes on the basis of the A/C flight condition / flap setting. Currently, numerical studies and preliminary lab experiments have been carried out looking at the next validation activities on the true-scale prototype expected in 2020.

4.1 Clean Sky challenge: JTI and Airgreen 2 frameworks

Air transport contribution to climate change represents the 3% of manmade CO₂ emissions and 12% of all transport sources with flights producing 628 Mtonnes of CO₂ yearly. Worldwide, it is estimated that the equivalent of 1300 new international airports will be required by 2050 with a doubling in commercial aircraft fleets. The aviation is therefore facing the challenge to meet the predicted growth in demand for air travel increasing (4-5% per annum over the next 20 years) while avoiding detrimental impacts on the environment. The Advisory Council for Aeronautics Research in Europe (ACARE) sets the reduction of environmental impact for aeronautics as one of its main targets, thus requiring new technological solutions for reducing CO₂ emissions, by 50% between 2000 and 2020, NO_x emissions by 80% and noise by 50%. Moreover, it specified that the aircraft lifecycles should be taken into account in order to reduce the environmental impact of manufacturing, maintenance and recycling. In 2007, the European Union founded the Clean Sky Joint Undertaking with the main purpose to bring aeronautics research and innovation stakeholders closer together, working on ambitious projects in technologies aimed at reducing, by 2020, the global environmental impact of the aircraft, [1]. In this perspective, regional aviation is a key factor for creating resources and an efficient air transport system that respects the environment, ensuring safe and seamless mobility, whilst reinforcing Europe's aero-industrial leadership. A substantial contribution to Clean Sky derives from Regional Air Transport that, to drastically reduce the environmental impact, adopts innovative solutions across several technology domains. Clean Sky was divided into different subprograms, one of them specifically directed to adaptive architectures, [2]. Advanced architectures have been already or will be developed to be adopted as wing control surfaces for loads control function and/or innovative high-lift devices (smart droop nose, morphing flap) in order to achieve lighter and simplified actuation/kinematic systems including relevant electronic control. Morphing structures have been investigated within a large number of research activities over past decades. Morphing wings matching the optimal aerodynamic shape at any flight condition is the most challenging aeronautical application of such technology. Current projects will provide technology maturation (TRL 4/5) for the structural-mechanics and materials aspects, including full-scale limited experimental validations. The adoption of morphing control surfaces and their validation in an operational environment through fly testing therefore represent a step forward, looking at potential application of such technology to innovative green airliners. In particular, morphing of metallic wing structures has always fascinated generations of researchers; numerous unconventional architectures have been proposed, tailored on specific end-applications and aircraft types. Although different for layout, all of them can be categorized in two basic groups: mechanized architectures and compliant mechanisms. Mechanized architectures implement morphing through the rigid-body motion of stiff subcomponents interconnected by suitably designed kinematic chains and actuation leverages, [3-18]. Each subcomponent of the kinematic chain is sized to provide its own contribution to the adsorption

of the external solicitations arising in operative conditions; actuators and actuation transmission lines are sized to enable the motion of the system and to preserve given shape configurations while counteracting aerodynamic loads with the minimum need of power, ([5],[7-8],[19]). Compliant mechanisms, [20-30], involve the deformation of structural elements to enable the required shape-change; mechanical properties of the structure have to be properly distributed in order to assure adequate morphing compliance and adequate stiffness to withstand external loads. Compared to compliant structures, rigid-body mechanisms offer a more direct solution to the paradox of morphing a structure which is considerably stiff to safely withstand external loads. Fewer actuators are typically required to control the morphing process whose overall benefit expected on the system level drives the additional mass, volume, force and power required by the actuation system. In force of this consideration, it naturally follows that the adoption of mechanized structures becomes quite mandatory when dealing with large aircraft applications ([3-4],[6],[8]) and/or when multi-modal morphing functionalities have to be assured, [17]. Within the framework of the JTI-Clean Sky project [2], and during the first phase of the Green Regional Aircraft Integrated Technological Demonstration (GRA-ITD), researches were carried out on the design and technological demonstration of a novel mechanized architecture enabling the camber variation of a flap segment to be installed on the next generation open rotor green regional aircraft (EASA CS-25 category, [31]); the driving idea was to replace a conventional double slotted flap with a single slotted morphing flap in order to improve aircraft high lift performances -in terms of maximum attainable lift coefficient and stall angle- as well as to reduce the noise emitted by the high lift system. Studies were limited to a portion of the flap element obtained by slicing the actual flap geometry (0.62 meters chord) with two cutting planes distant 0.8 meters along the wing span (Figure 4.1), [14]. The Regional Aircraft IADP will focus on demonstrating and validating key technologies that will enable a 90-seat class turboprop aircraft to deliver breakthrough economic and environmental performance and superior passenger experience. Regional aircraft are a key element of Clean Sky 2, providing essential building blocks towards an air transport system that respects the environment, ensures safe and seamless mobility, and builds industrial leadership in Europe. The Regional Aircraft IADP will bring technologies to a further level of integration and maturity than currently pursued in Clean Sky 1. The goal is to integrate and validate, at aircraft level, advanced technologies for regional aircraft so as to drastically de-risk their integration into future products. The control of the shape of adaptive devices has the potential to improve the aerodynamic performance of the wings with respect to off-design situations. A possible way to achieve this goal is to implement specific technologies for trailing edge morphing trailing, aimed at modifying the airfoil camber in flight. As part of the Clean Sky project, an innovative actuation system has been developed that comprises electro-mechanical modules. A challenging key aspect is the ability to get and preserve desired target wing shapes within a certain tolerance, allowing optimal aerodynamic performance in operative conditions and loads. In this chapter, the strategies followed to define the electro-actuation and control system of a morphing flap are outlined with emphasis on both numerically and experimental methodologies that have been implemented. On 2014, the European Commission officially launched Clean Sky 2, the second phase of the most important aeronautics research and innovation program ever undertaken in Europe. The continuation of Clean Sky will allow Europe to develop environmentally friendly, efficient aircraft, solutions intended for the worldwide marketplace and meeting society's expectations. Beyond industrial examples such as cabin technologies, manufacturing, maintenance, hybrid propulsion and others, many major research efforts are being launched or planned in Clean Sky 2. In the framework of the Clean Sky 2 – Airgreen 2 project, a novel multi-functional morphing flap technology was investigated to improve the aerodynamic performances of the next Turboprop regional aircraft along its flight path, Figure 2. Within such research scenario, an un-shafted distributed electro-mechanical arrangement represents an attractive solution for the actuation system of the morphing flap, in full agreement with the current needs for a “more electrical aircraft”. Despite the progress achieved in smart materials technology, their high power consumption, requiring a heavy power system, has limited their application in aerospace. Consequently, the aviation industry is moving towards well established electro-mechanical actuation solutions for rapid application in flight. Lightweight actuators are part of the trend in green aviation. Maximizing the integration of electrical systems in future aircraft will reduce their weight. The adoption of electrical actuators, such as DC motors, will bring multiple benefits in addition to those gained by morphing, because such actuators are lightweight, can be easily integrated into a structural system, and need less power than smart materials. The work deals with the design of the electro-mechanical actuation system for a full-scale flap as an alternative solution to the standard hydraulic actuation based

mechanisms. Design activities and experimental validation (ground test) of the proposed arrangements are both covered.

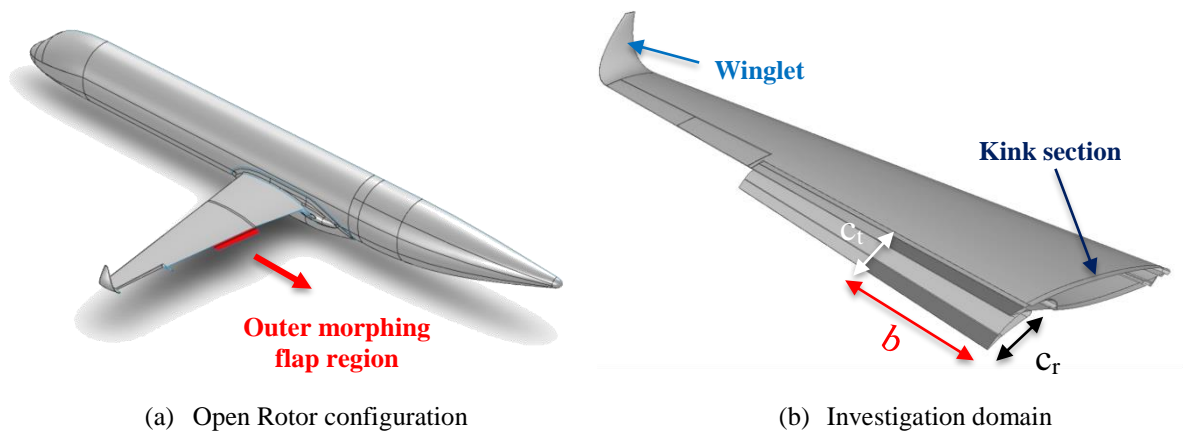


Figure 4.1. Reference wing for Clean Sky – JTI outer flap.

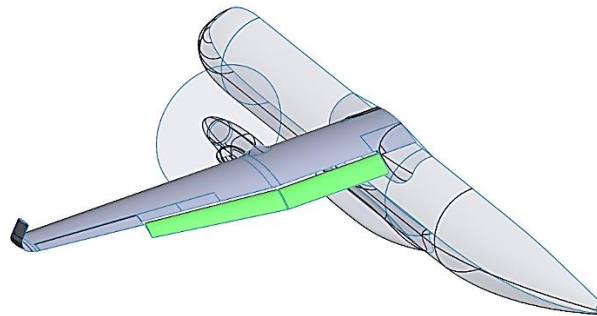


Figure 4.2. Reference turboprop aircraft for Clean Sky 2 – Airgreen 2 morphing flap.

4.2 Robotized system architecture

4.2.1 Mechanical constraints

When dealing with adaptive lifting surfaces such the flap, required high functionality of the resulting system is obviously associated to a structural design complexity. More in detail, an adaptive structure allows the controlled and fully reversible transition from a baseline shape to a variety of different configurations. For this reason, a kinematic mechanism was applied to create ribs with bi-modal camber morphing capabilities. More in detail, each of the eight flap articulated ribs was assumed to be segmented into four consecutive blocks (B0, B1 and B2 and B3) connected to each other by means of cylindrical hinges displayed on the airfoil camber line (H1, H2, H3) in a “finger-like” configuration. In this way, consecutive blocks can rotate relatively. In Figure 4.3, a bays assembly sequence is shown. Moreover, non-consecutive rib plates are connected by means of a link (L) that forces the camber line segments to rotate according to specific gear ratio. The ribs kinematic was transferred to the overall flap structure by means of a multi-box arrangement. The bi-modal morphing capability was implemented by active ribs playing the role of inner movable articulation of the flap structure, Figure 4.4. An internal leverage (K12) is hosted by block B1 and interconnect blocks B1 and B2. This leverage is activated by the external rotary actuator (M1) and amplifies its torque. The rotation induced by M1 makes the leverage K12 to move and therefore changes the relative position of block B1 with respect to block B3; at the same time blocks B0 and B2 are forced to follow the movement of B1 and B3 being mutually interconnected to the them. The position of the link L and of the pivots of the leverage K12 are selected in a way that, upon the rotation of M1 shaft, all the rib blocks rotate around hinges H1, H2, H3 according to specific angles compliant with the set of external morphed shapes

to be matched. A secondary leverage (K23) links B3 to B2 and is driven by the rotation of the actuator M2. The secondary leverage, hosted by block B2, amplifies the torque of the actuator M2 and makes B3 to rotate around the hinge H3 thus implementing the tab-like morphing. The layout of the morphing rib was properly adapted to fit the geometry of the flap device at each span-wise section. The adaptation included only a slight reshaping of the upper and lower boundaries as well as the extension of the chord-wise length of blocks B0 and B3 while moving from the inner section to the outer one. The chord-wise length of blocks B1 and B2 was kept equal for all flap sections thus obtaining hinge lines perpendicular to ribs' reference planes. Two C-shaped (continuous) spars (Al2024-T351) were positioned in correspondence of the 5% and 70% of the local airfoil chord in order to link all blocks B0 and B3 along the span.

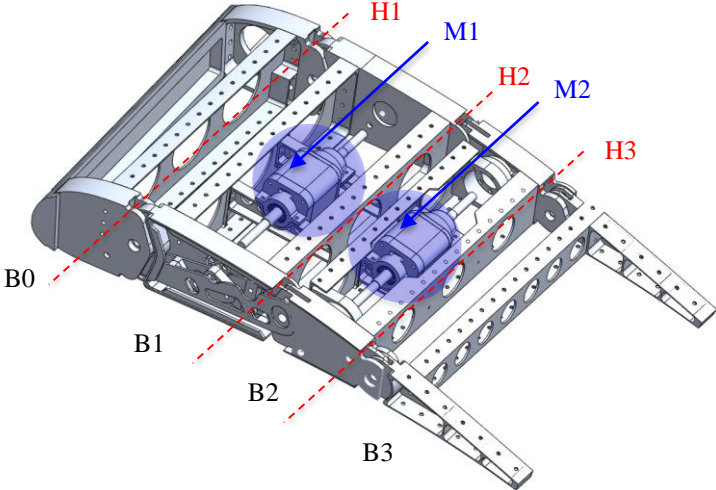


Figure 4.3. Actuated morphing bay.

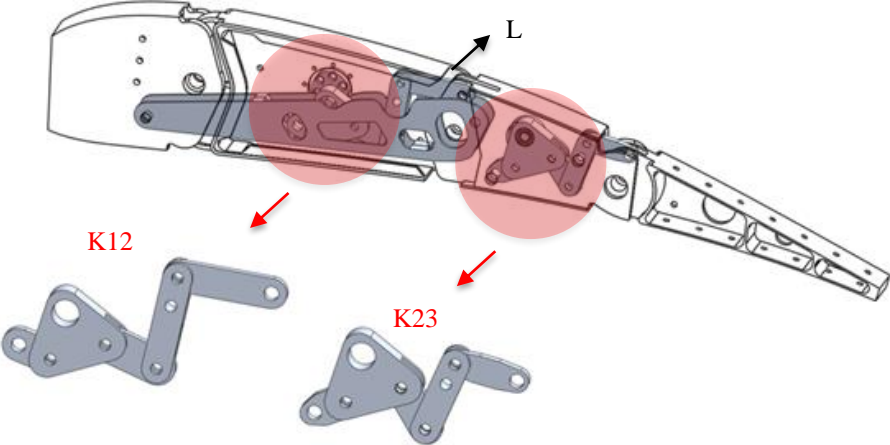


Figure 4.4. Bi-modal morphing bay: “5 bars-linkage” to enable the shape modification.

These spars were suitably conceived to provide the greatest contribute in carrying external loads while assuring adequate deformation levels to the entire assembly. Segmented spars and stringers were then adopted to generate a multi-box arrangement elastically stable under bending and torsion. Also for these longitudinal elements Al2024-T351 was selected. Both ribs and longitudinal stiffening components were properly shaped in order to enable the installation of a segmented skin solution characterized (on both upper and lower side) by four elements in Al2024-T4 sliding on each other as *armadillo shells*. Rubber seals were used to avoid friction between adjacent skin segments as well as to prevent airflow leakages. The shape of

the seals was defined by means of advanced kinematic analysis simulating flap morphing in both modes; these analyses also allowed for the verification of the implemented assembly tolerances while proving the absence of clashes between adjacent subcomponents in relative motion. The final layout of the device is depicted in Figure 4.5 while the skin segments in Figure 4.6.

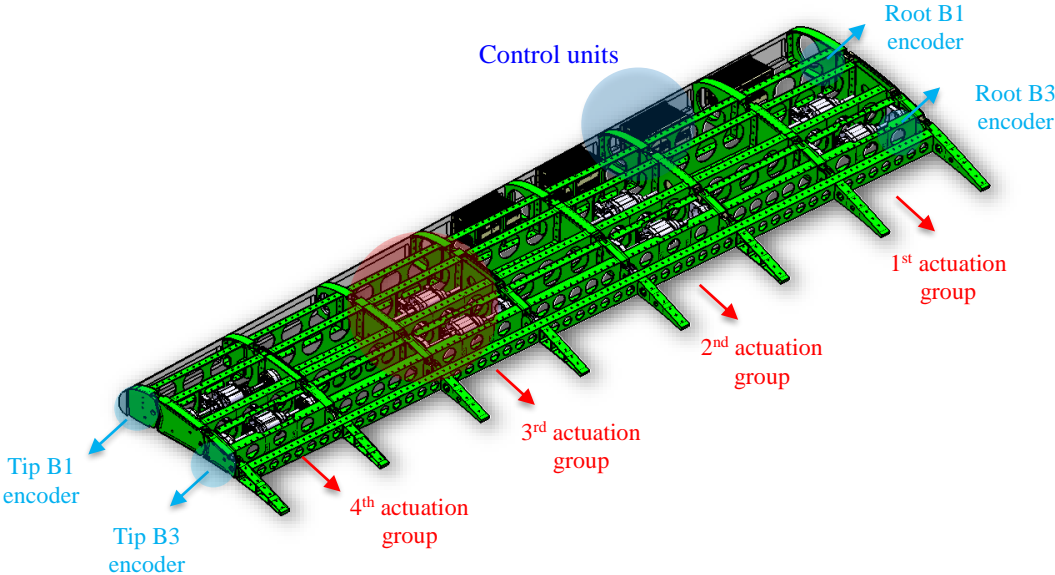


Figure 4.5. Bi-modal morphing flap layout: skeleton and systems (hidden skin).



Figure 4.6. Morphing flap skin arrangement: global architecture.

4.2.2 Actuation design

On the basis of preliminary addressed analysis, several load conditions were considered to size the distributed actuation system of morphing device. Then the aerodynamic hinge moment determines the joint torque necessary to size the actuation system: direct current (DC) actuators have been located in correspondence of three bays thus assuring a more controllable morphing shape along both the span-wise and chord-wise direction. The required torque is ensured by speed reducers (Harmonic Drive®), keyed on the motor shafts: HD® represents a typical gear widely used in mechatronic applications. Among its main advantages: no backlash, compactness and light weight, high gear ratios (in such application 120:1),

reconfigurable ratios within a standard housing, good resolution and excellent repeatability when repositioning inertial loads and high torque capability. The complete actuation design process is reported in Figure 4.7.

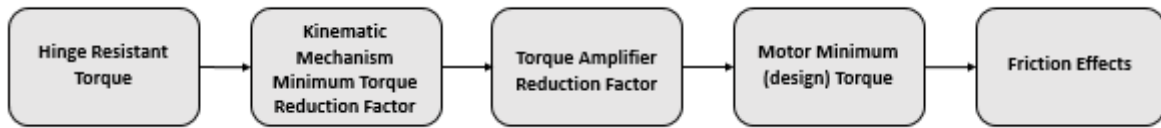
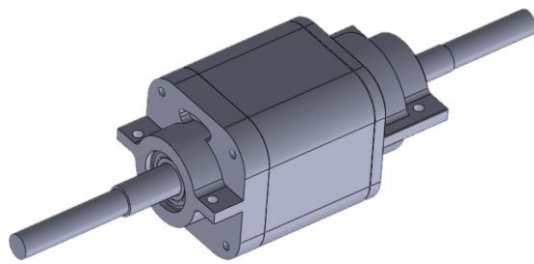


Figure 4.7. Actuation design process.

Sensitivity studies were carried out to find out the minimum number of actuators required to morph the flap under the action of design aerodynamic loads. Relying upon the available space and taking in account specific constraints in terms of efficiency, power and reliability, the Kollmorgen™ brushless motor KBMS-14 was down-selected (Table 4.2). Four actuation groups were considered adequate to move the whole structure in operative conditions. They were respectively linked to the 1st, 3rd, 5th and 7th bay and duly coupled to Harmonic Drive™ gearboxes (model HFUC-17-120-2UH-SP2983, Table 4.2), hosted by ribs blocks and acting as amplifiers of the actuation torque (and reducers of the shaft rotation speed). In Figure 4.8 the actuator and gearbox models are roughly depicted.



(a) Kollmorgen KBMS14™ Brushless Motor



(b) Harmonic Drive™ torque amplifier

Figure 4.8. Actuation and transmission components.

Table 4.1. Actuator and HD™ main features.

Specification / Actuator Model		KBMS-14	Speed Reducer Model		HFUC-17-2UH
Continuous Stall Torque	Nm	2.11	Gear Ratio	-	120
Peak Stall Torque	Nm	5	Maximum Torque	Nm	54
Maximum Speed	RPM	8000	Maximum Speed	RPM	60
Peak Current	Arms	10	Moment stiffness	Nm/rad	$16 \cdot 10^3$
Weight	Kg	2.5	Weight	Kg	0.64
Number of Poles	-	8	Temperature range	°C	0-60

Such actuation system allowed the achievement of each rib mechanism total output torque (T_{out}) expressed in Equation (4.1):

$$T_{OUT} = M_T \cdot R_{HD} \cdot K_{MA} \cdot C_{JHD} \quad (4.1)$$

Where M_T is the motor torque assumed constant and equal to half of the stall torque (0.6 Nm) in correspondence with the operational speed ($\omega = 400$ rpm); $R_{HD} = 120$ is the Harmonic Drive[®] constant torque amplification factor; K_{MA} is the kinematic mechanical advantage, whose has minimum torque amplification factor of about 5. Finally, C_{JHD} represents a torque correction factor including Harmonic Drive[®] maximum torque with respect to the product $M_T \cdot R_{HD}$, and for this reason equal to 0.75. Actuation total output torque (4.1) (with and without the C_{JHD} correction factor) and H3 hinge torque trends are reported in logarithmic scale in function of the H3 hinge rotation angle in Figure 4.9. It emerges the actuation system clear capability in overcoming the resistant hinge torque. In Figure 4.10 the assembly sequence of actuators, gearbox and rib blocks is roughly depicted.

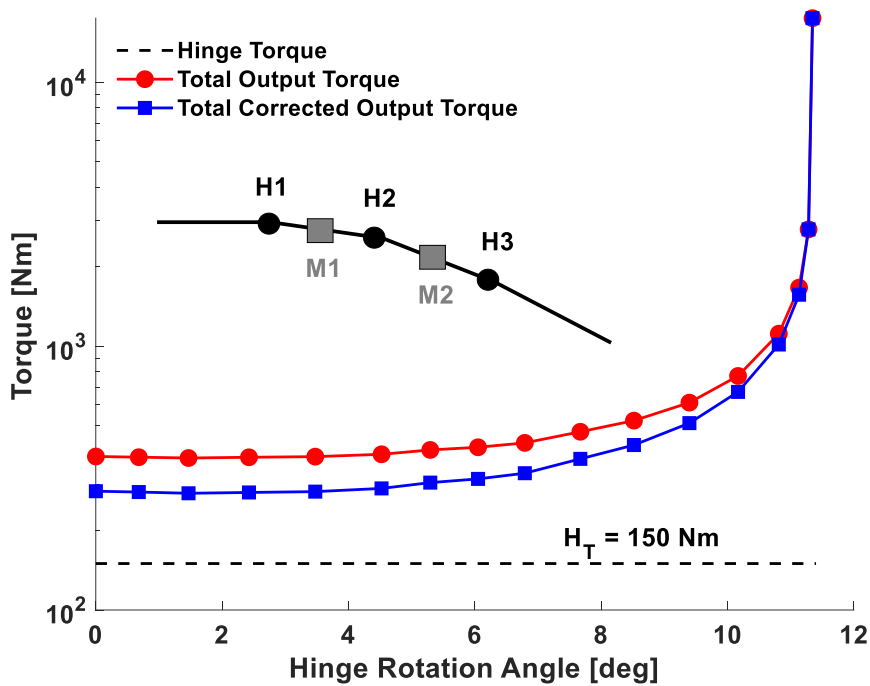


Figure 4.9. Actuation total output and H3 hinge torque trends vs H3 hinge rotation angle.

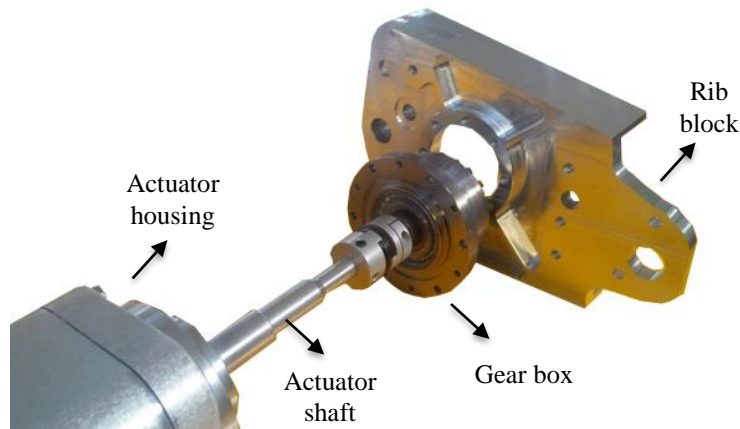


Figure 4.10. Actuation torque application.

4.3 Morphing flap overview

4.3.1 Target shapes and specifications

The articulated mechanism for flap camber morphing was designed with reference to the most severe load condition expected in service; from an accurate comparison of the solicitations induced by more than 20 different load cases, the enveloping limit condition was found as the climb case related to uncambered flap deployed at $\delta_{flap} = 35^\circ$, flight speed $V_\infty = 95.2 \text{ m/s}$, angle of attack $\alpha = 6^\circ$, sea level and max zero fuel weight. The highest resisting hinge torque ($H_T = 150 \text{ Nm}$) occurred in correspondence of the hinge axis connecting blocks B2 and B3, indicated with H3 in Figure 4.11, [17]. This led to the choice of such resistant hinge torque as the designing one for all the actuation kinematic mechanism. However, in order to deal with a high entity design torque, it was mandatory to introduce into the actuation system some suitable torque amplifiers devices.

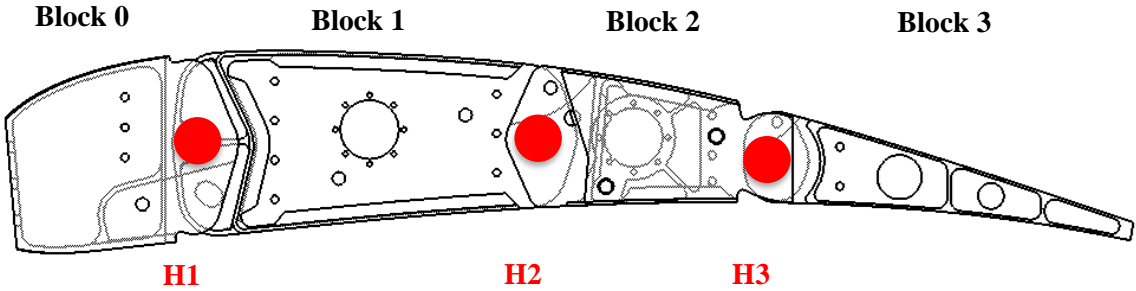


Figure 4.11. Morphing rib and its hinge lines.

A first phase of the work involved the determination of optimized airfoil shapes at a several flight conditions. The scenario of the project was very broad and involved both academic and industrial partners. The aerodynamic requirements were in fact defined by Leonardo Finmeccanica – Aircraft Division. 2D CFD optimization simulations were addressed to assess the design morphed shapes, as outlined in [32]. These results were used as input data to design a structural concept that guaranteed the reversible transition of the flap from the nominal configuration (baseline) to the target shapes. These optimized shapes were used as a starting point for the actuation system design; in correspondence of these shapes the aerodynamic loads to be counteracted by the actuation kinematics were evaluated together with the strain/stress field induced all over the structure. Table 4.1 recaps the rotations angles of flap rib blocks useful to reproduce the flap target shapes (Leonardo Finmeccanica – Aircraft Division and CIRA).

Table 4.2. Relative rotations between rib blocks (design values).

Relative rotation between:	Camber Morphing Mode	Tip Deflection
Rib blocks B1 and B2	3°	0°
Rib blocks B2 and B3	10.5°	0°
Rib blocks B3 and B4	3°	+10°; - 10°

4.4 Control logic strategy and Lab test on Iron Bird

4.4.1 System arrangement

The transmission chain along the chord-wise direction consisted basically of a kinematic mechanism, driven by load-bearing brushless actuators that acted directly on morphing ribs. The absence of a transmission shaft along the span, and the distributed arrangement of electro-mechanical actuators derived from the very demanding size and weight constraints the system has to comply with. Moreover, a distributed sensor system based on relative encoder generated the signals for the appropriate feedback actions and, at the same time, monitored possible faults inside the actuation mechanism. Eight controllers (ServoOne Jr. by LTI[®] motion, Figure 4.12(a), [16-17]) were mounted in the first 4 bays of the leading edge in order to drive the actuation groups. Encoders for relative rotation measurement were placed at the hinges H1, H2 and H3 of the ribs at station 1, 4 and 8. The measured rotations were then used to rationally drive the actuators and to preserve the commanded flap shape in case of variation induced by external perturbations (including aeroloads). The electric connection among all control units, was realized by means of a proper shielded routing, guaranteeing the logic correspondence between servo-drivers plugs and terminal pins. Such connection arrangement enabled the synchronized trigger of the actuators according to the master&slave based logic depicted in Figure 4.12(b).

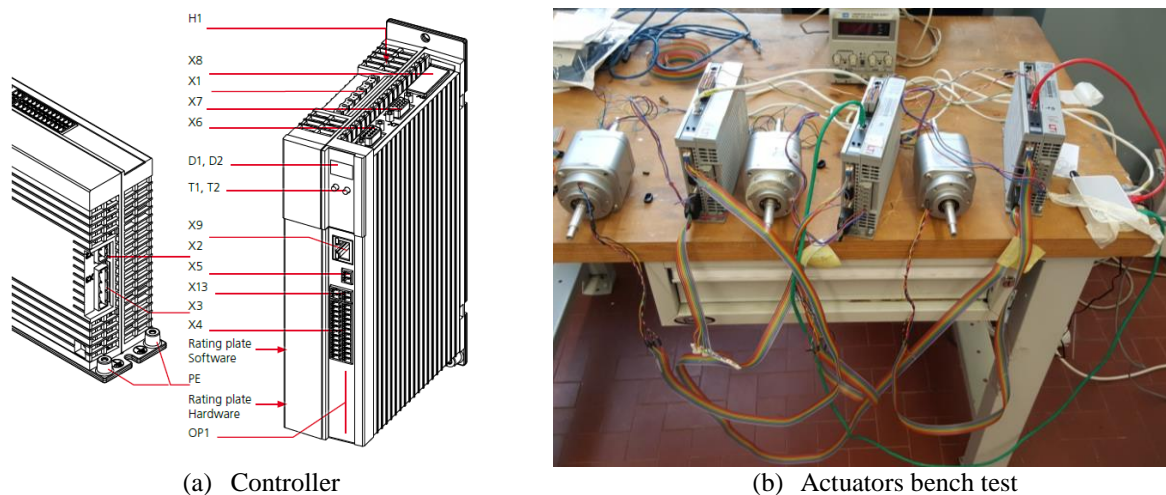


Figure 4.12. Control units of brushless motors.

The transmission ratios imposed between the slave and master EMAs were set as 1:8 and to 1:1 respectively for the first row (Block 1) and for the second row of actuators (Block 2) in chord-wise direction. A value of speed equal to 400 rpm was set for all the actuators and an acceleration/deceleration of 100 rpm/s was implemented to obtain a quasi-static morphing evolution (15 sec. duration) without dynamic oscillations due to inertial effects. As shown in Figure 4.13, the control loop of the actuator position used the motor encoder position as feedback signal. The bench test provided a first experimental validation of the designed controller and its hardware integration architecture; moreover, it was possible to appreciate the reproducibility of the theoretical reference and optimized airfoil shapes. On the other hand, the test offered the opportunity to make some adjustments in the mechanical part of the model and some tunings of the encoder transducers zero positions. When the controller was tested on the bench two steps were performed:

- (1) Stand-alone verification of each actuator;
- (2) Simultaneous testing of the actuators controlled by the central servo-drive, Figure 4.13.

This logical scheme enabled the synchronized activation of actuators according to the master and slave multi-axis strategy.

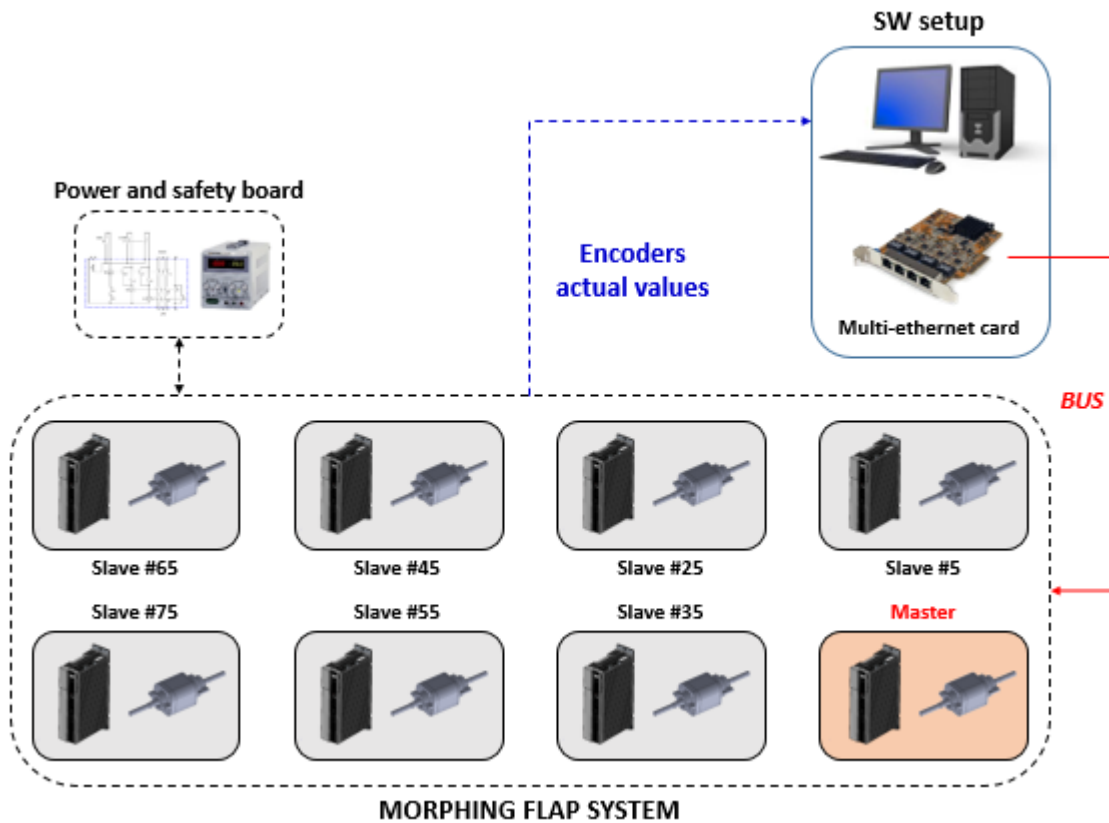


Figure 4.13. Architecture of the loop control: centralized logic.

The morphing flap prototype was used as mechanical demonstrator to prove the adequacy of the adopted solutions with respect to design requirements and system specifications. Three test campaigns were carried out:

- functionality test campaign;
- static test campaign;
- ground resonance test.

The main objectives of each campaign have been outlined in the following subparagraphs together with a general description of performed pre-test activities and test outcomes. In order to visually check the status of the inner structure and embedded equipment, skin modules were removed during all tests. For static tests, the applied load was reduced in order to compensate for the increased structural elasticity due to the absence of the skin.

Functionality test

These test were carried out to demonstrate that the flap was able to reproduce target morphed shapes in a controlled and repeatable manner (Figure 4.14). The target morphed shapes were considered successfully achieved if the angles between adjacent rib blocks -obtained upon actuators activation- matched the design values pertinent to each morphing mode (Table 4.3) with a precision of 0.5° . According to the general layout presented in Figure 4.5, the first and the last sections of the flap were then equipped with additional high precision encoders measuring in LabVIEW® environment the relative rotations between blocks B0 and B1 and between blocks B2 and B3 (Figure 4.15); due to the mechanical link between B0 and B2 it was considered un-relevant to place an additional encoder also between B2 and B3. Additional encoders were equipped with digital displays for real-time measure reading. The flap was then installed on an exhibition rig: the baseline and morphed configurations implemented during the tests have been reported together. Test protocols were repeated 20 times and at each cycle the measured angles resulted fully compliant with the design expectations at both inner and outer flap sections, Figure 4.16.

Table 4.3. Functionality test protocol.

Camber Morphing Mode	Tip Deflection Mode
<ol style="list-style-type: none"> 1. Voltage actuators activation; 2. Control switch to desired mode; 3. Actuation up to the target configuration; 4. Actuators stop and acquisition of rib blocks relative rotations; 5. Actuation reverse, up to the baseline configuration; 6. Actuators stop, flap power off, check of the encoders displays for full rotation recovery. 	<ol style="list-style-type: none"> 1. Voltage actuators activation; 2. Control switch to desired mode; 3. Actuation up to the tip down configuration; 4. Actuators stop and acquisition of rib blocks relative rotations; 5. Actuation reverse up to the baseline configuration; 6. Actuation up to the tip up configuration; 7. Actuators stop and acquisition of rib blocks relative rotations; 8. Actuation reverse up to the baseline configuration; 9. Actuators stop, flap power off, check of the encoders displays for full rotation recovery.



(a) Baseline



(b) Camber morphing



(c) Tab up



(d) Tab down

Figure 4.14. Flap configurations functionality test.

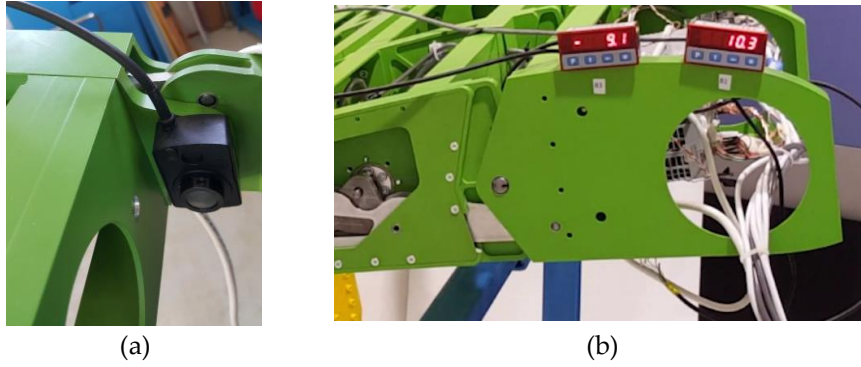


Figure 4.15. Sensing strategy: (a) hinge encoder and (b) rotations displays.

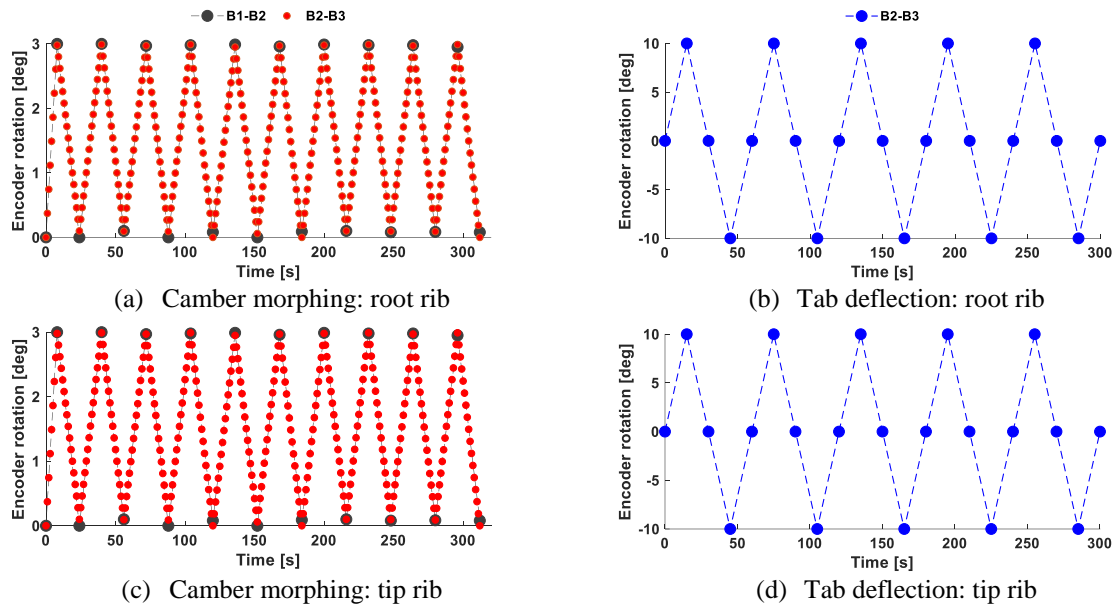


Figure 4.16. Flap configurations functionality test.

Static test

Static test was carried out to demonstrate the flap's capability to withstand limit loads without permanent deformations, failures or buckling (as per part C of EASA airworthiness requirements CS-25, [31]), Figure 4.18. The flap was constrained in correspondence of the blocks B1 belonging to the third and the sixth rib (from the root section) thus simulating a joint with a potential (and ideally rigid) deployment track. The pressure distribution related to the limit load condition (uncambered flap deployed at 35° , $\delta_{flap} = 35^\circ$, flight speed $V_\infty = 95.2$ m/s, angle of attack $\alpha = 6^\circ$, sea level and max zero fuel weight, see par. 2.1) was converted into an equivalent set of lumped forces acting at the centre of rib blocks B0, B2, B3. (Figure 4.17) and easily reproducible during tests through a whiffle-tree (Figure 4.18). The maximum vertical force to be applied at the top of the whiffle tree to reproduce the limit design condition (1650 Kg) was reduced by the 10% in order to account for the absence of the skin during test¹. Fifteen load steps of 100 Kg each, with a loading speed of 10 Kg/s, were considered adequate to avoid any dynamic amplification. A pause of 10 seconds at the achievement of each load step was moreover set to check data acquisition; load levels were measured through a load cell installed between the hydraulic jack and the whiffle-tree. All the actuators

¹ The skin was not installed in order to allow for a quick inspection of the inner flap structure during the test. The 10% reduction of the maximum load was evaluated on the base of pre-test simulations showing that the induced displacement field along the unskinned flap would have been the same of that induced by the full limit load along the skinned flap.

were turned on (powered) during the test in order to provide adequate (electrical) torque to counteract applied loads.

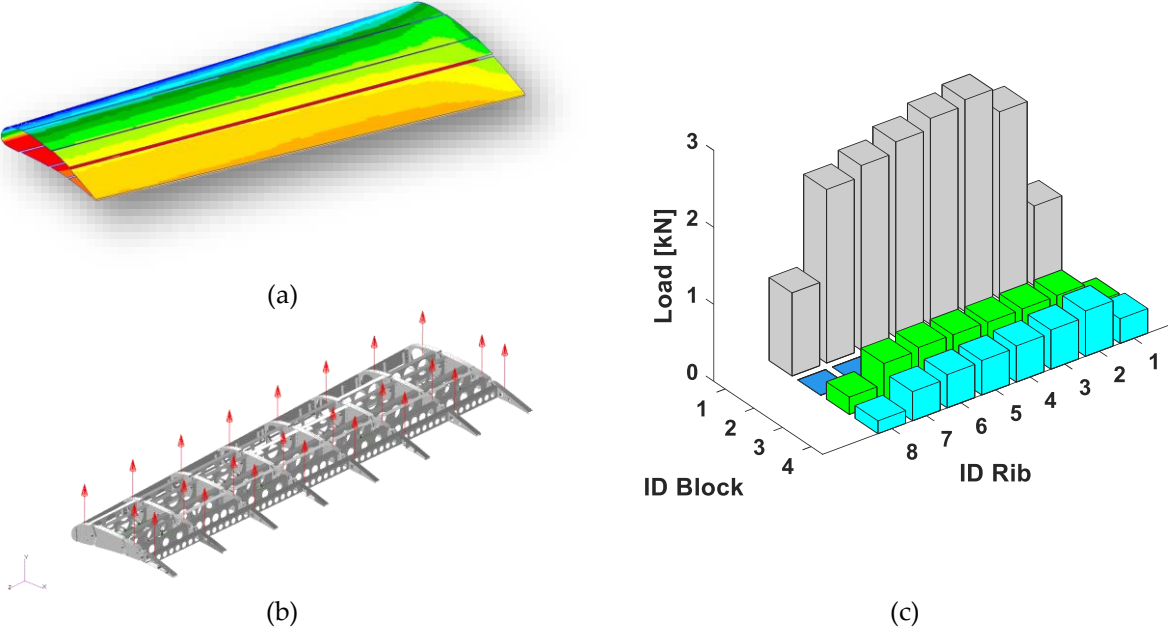


Figure 4.17. (a) pressure distribution at limit design condition; (b) lumped forces distribution along blocks B0, B2, B3 equivalent to the pressure distribution at limit design load condition; (c) histogram of the equivalent lumped forces distribution applied during tests (blocks B1, constrained).

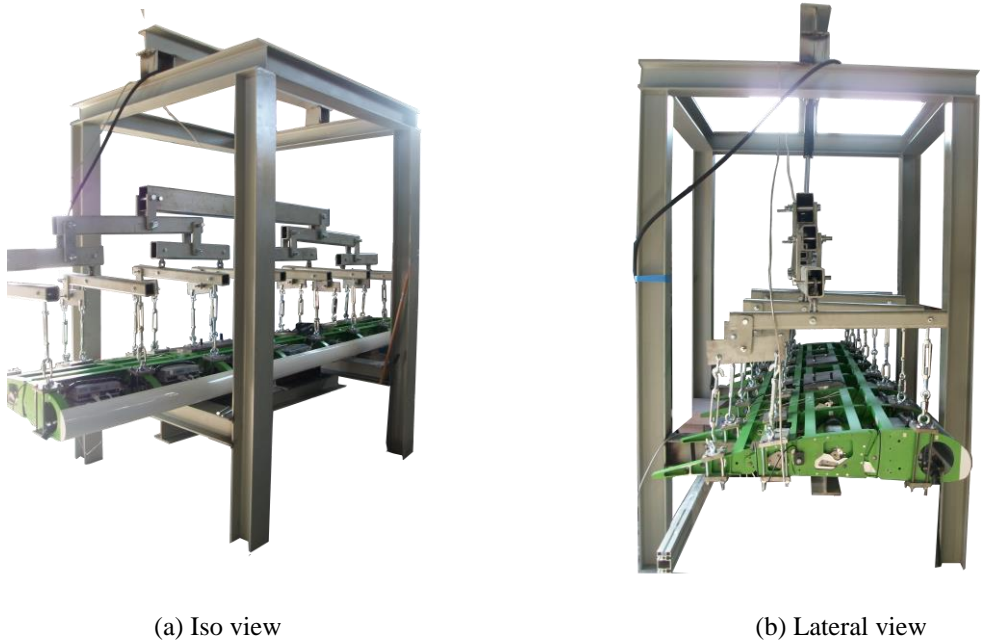


Figure 4.18. Whiffletree and rig for static test.

Actuation system capability to preserve the baseline flap shape under the action of aerodynamic loads was positively verified with a maximum deviation that resulted lower of 0.5° (Figure 4.19). No jamming of the actuation system occurred during the static test; after load removal, the flap was repeatedly morphed thus proving the full functionality of the actuation lines. The levels of electrical power absorbed by the actuators during the static test resulted within the nominal target values, thus ensuring the compliance of the system with safety-related aspects related to power supply (Figure 4.20(a)).

As expected, the obtained power absorption distribution (Figure 4.20(b)) recalls the trend of the applied load outlined in Figure 4.17(c). The absorbed power (P_{ABS}) was estimated by Equation (4.2):

$$P_{ABS} = V_{DC} \cdot I_{rms} \quad (4.2)$$

Where V_{DC} represents the DC link voltage (220 V) and I_{rms} the actual current (Arms). The results show that the current levels absorbed by the actuators are well below the saturation limits indicated in Table 2, thus proving the robustness of the electrical system with respect to possible jamming events at the contingent load condition.

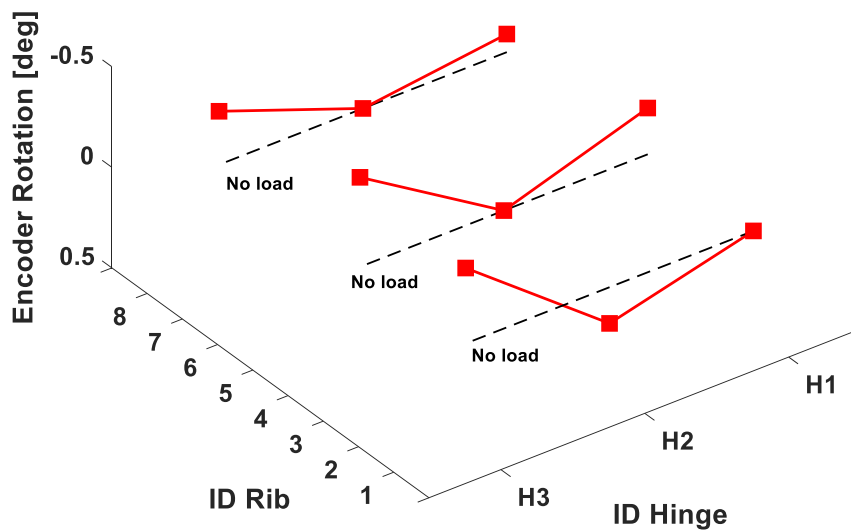


Figure 4.19. Deviation from the baseline configuration at rest: static load of 1520 N.

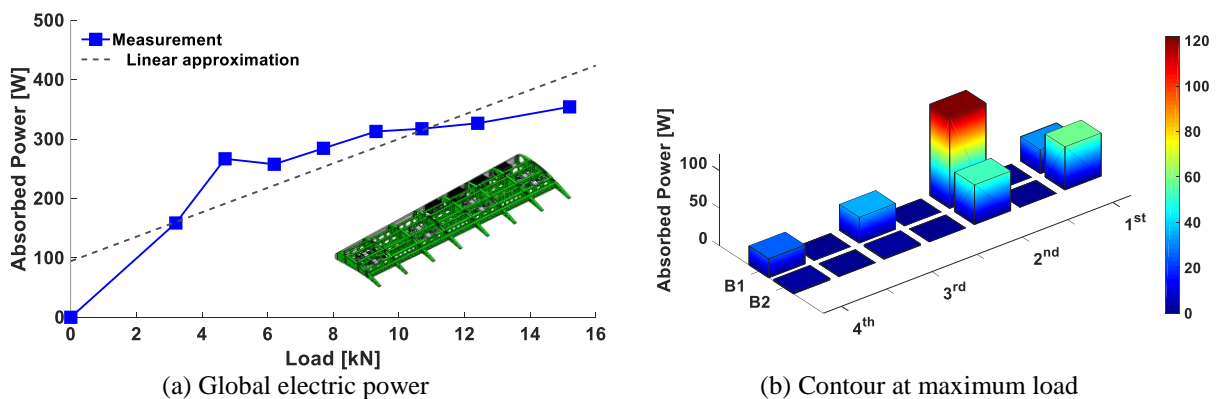


Figure 4.20. Absorbed power under static load.

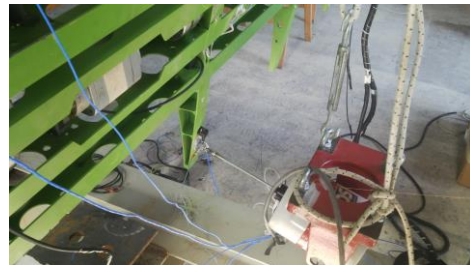
Dynamic test

At high speed only the first three segments of the morphing flap are stowed in the wing while the tab remains exposed to the aerodynamic flow and used for load control. From the aeroelastic standpoint, the tab behaves as a large aileron and detrimental flutter instability may arise from the coupling of the first wing bending mode with the tab harmonic (elastic oscillation of the tab around its hinge axis). Aeroelastic analyses based on numerical models [33-34] proved however that the flap tab design was safe from the flutter stand point considering also the functioning of the electric line feeding the actuators; in order to give experimental evidence of this result, ground resonance tests were carried out to validate the flap dynamic model used for theoretical flutter analyses. This validation was performed by correlating numerical and experimental generalized parameters related to the only flap mode proved to be relevant for flutter stability [34]: the tab harmonic at powered actuators.

The flap was suspended to a test rig through soft springs in order to reproduce a free-free condition, Figure 4.21; all the actuators were powered on. The “Normal Mode” method was then used to detect the generalized parameters of the flap tab harmonic mode in correspondence of powered actuators. The procedure for acquiring modal parameters is generally long and expensive: it requires advanced load control systems and a dense sensing network. In such context, a hand-controlled force was applied, isolating and acquiring the dynamic response of tab modes with only few accelerometers. The experimentally identified tab harmonic (3.358 Hz) resulted well in line with the theoretical expectations (3.350 Hz, see Figure 4.22). No further modes were detected in the frequency range (0-100 Hz) considered to be of practical relevance for aeroelastic stability phenomena. The generalised mass of the mode was calculated by applying the Complex Power method, [35]. The control of force level is crucial during this phase, Figure 4.23(a). An active (imaginary and proportional to viscous damping) and a reactive (real and proportional to mass and stiffness) powers components are applied to the system by means of the shakers in the frequency range very close to the measured mode, Figure 4.23(b). With the aim to guarantee that the forces are constant in the considered range of frequency, the measurements are carried out in closed loop. The comparison between numerical and experimental values of tab harmonic generalized mass is summarized in Figure 4.24; also in this case a very good correlation level was obtained.

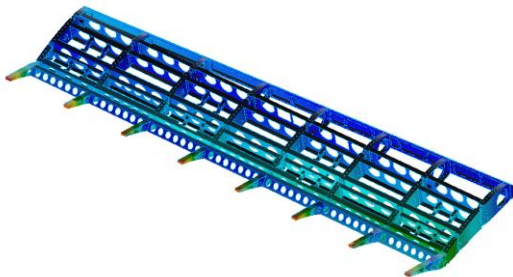


(a) Test rig and suspension configuration

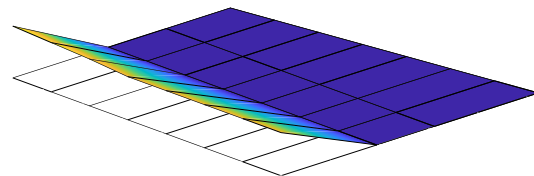


(b) Detail of the exciter

Figure 4.21. Boundary conditions of the GVT.



(a) Numerical mode, $f = 3.350$ Hz



(b) Experimental mode, $f = 3.358$ Hz

Figure 4.22. Tab normal mode in power on configuration.

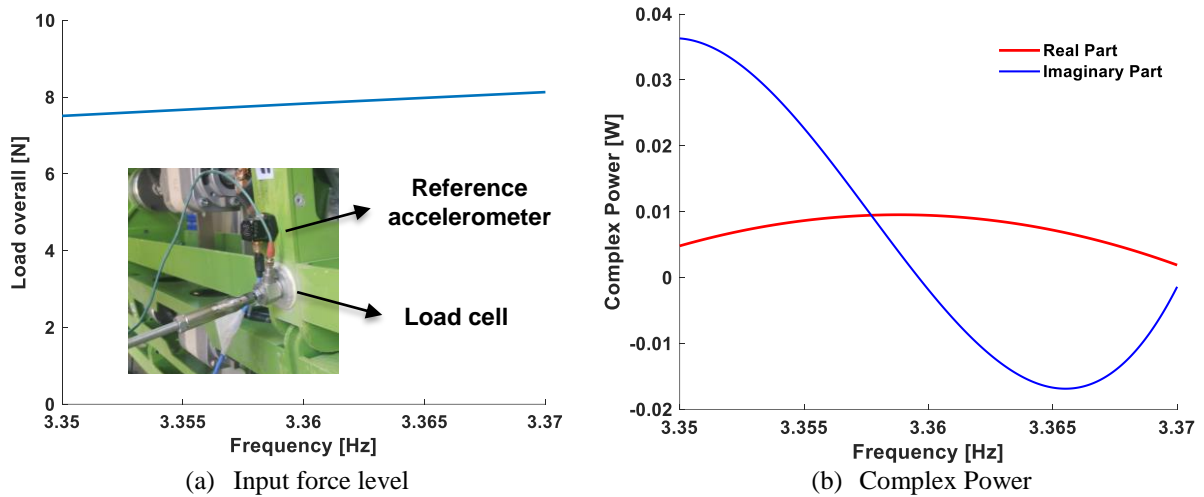


Figure 4.23. Frequency swept close to the resonance frequency ($f = 3.358$ Hz).

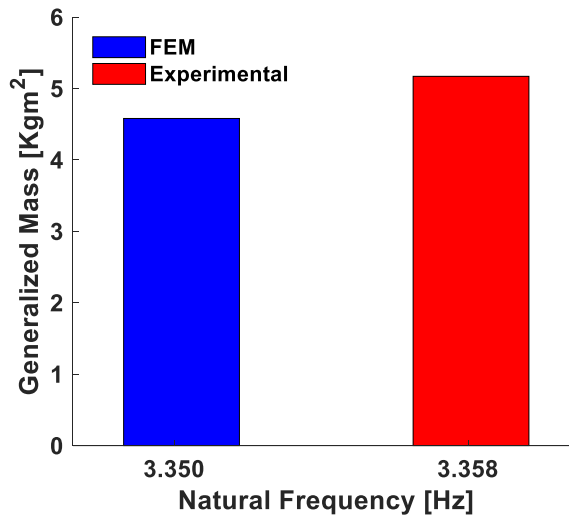


Figure 4.24. Generalized mass comparison.

4.5 Towards a Multi-modal Morphing Flap: Clean Sky 2 upgrade

In the framework of the current Clean Sky 2 – Airgreen 2 project, a novel multi-functional morphing flap technology is currently investigated to improve the aerodynamic performances of the next Turboprop regional aircraft (90 pax) along its flight path. Within such research scenario, an un-shafted distributed electro-mechanical arrangement represents an attractive solution for the actuation system of the morphing flap, envisaged in the current “more electrical aircraft” concept. For the morphing fowler flap, three different functions were planned in compliance with the initial design requirements defined in:

- Operating Mode 1: overall airfoil camber morphing;
- Operating Mode 2: $+10^\circ/-10^\circ$ (upwards/downwards) deflection of the flap tip segment (from the 90% to 100% of the local chord);
- Operating Mode 3: Tip segment twist ($\pm 5^\circ$ along the outer flap span).

Morphing mode 1 is supposed to be activated during take-off and landing only to enhance A/C high-lift performances also allowing for steeper initial climb and descent, noise-abatement trajectories. Thanks to this function, more airfoil shapes are available at each flap setting and therefore a dramatic simplification of the flap's deployment systems may be expected: actuation tracks could be hosted into wing airfoil shape without external fairing needs. Basically, very simple conventional track systems without external fairings are not able to comply with aerodynamic requirements in landing and take-off configuration; therefore, further needed positions are obtained using the overall airfoil camber (morphing mode 1) of the fowler flap in the retracted and extended configuration. Morphing modes 2 and 3 are related to the last chord-wise segment of the flap and are activated in cruise condition only, when the flap is stowed in the wing. Thanks to these modes, load control functionalities may be implemented to enhance wing aerodynamic efficiency, [26]. The new architecture of the three-modal morphing fowler flap (Figure 4.25) has been designed according to the challenges posed by real wing installation issues especially with reference to the minimum design space available at the tip section of the outboard section for the aero-shapes provide by Onera aerodynamic group, Figure 4.26. The operative configurations reflect different functional regimes of the flap: in low-speed conditions when the flap is fully deployed (mode 1) and in high-speed conditions where just the tab is exposed to the aerodynamic flux (mode 2 and 3).

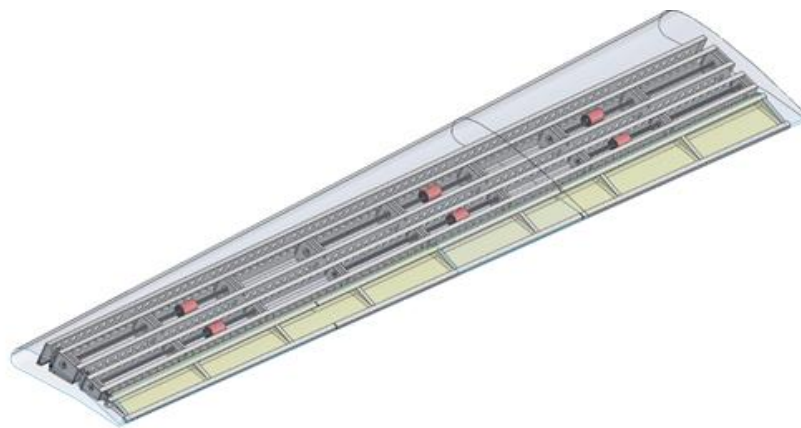


Figure 4.25. Outboard morphing flap, 8 bays and 6 actuators.

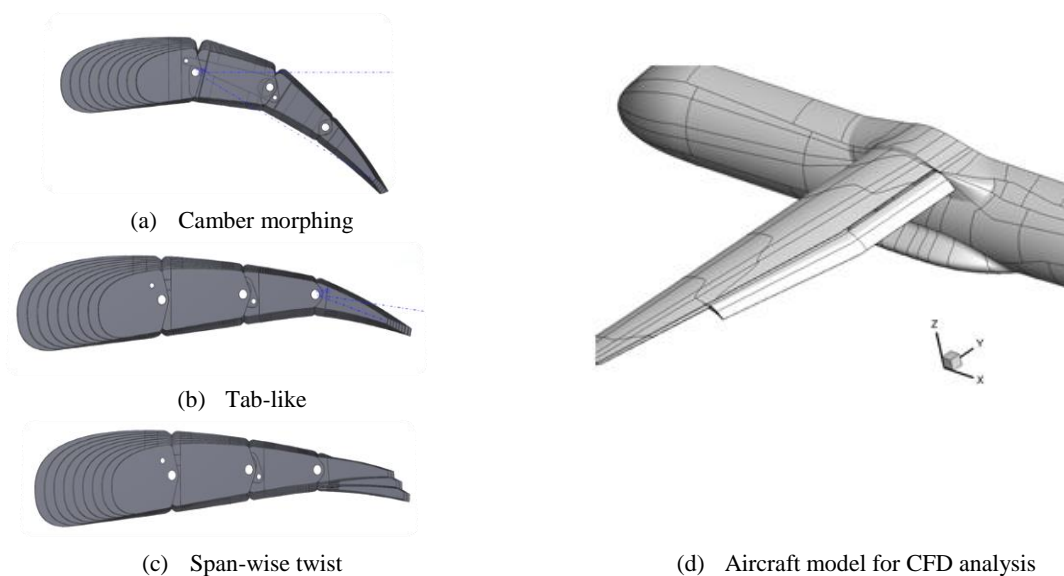


Figure 4.26. Flap configurations and numerical model, Onera.

4.5.1 Design Loads

Design Loads Envelopes (DLEs) have been defined for the main A/C components summarizing all the several loads conditions simulated/investigated in order to identify the most critical loads combination as loads envelope corner points. The current design structural loads of A/C structural elements can only be adequately represented by a more complex combination of shear, bending and torque loads distributions. Therefore, for each monitoring stations the most “significant” loads components have been defined chosen among the three forces and three moments, taking into account the peculiar characteristics of the A/C item in exam. Since strength requirements (CS 25.301, 25.303 and 25.305, [31]) are specified in terms of limit loads (the maximum loads to be expected in service) and ultimate loads (limit loads multiplied by prescribed factors of safety), unless otherwise provided, prescribed loads are limit loads. Limit loads are the loads that the A/C structure must be able to support without detrimental permanent deformation. At any loads up to limit loads, the deformation may not interfere with safe operations. In the present design loads assessment, limit loads are equal to design loads and, unless otherwise provided, prescribed design loads are limit loads. The morphing motion is achieved by means of a kinematic chain, which is servo-actuated by a set of hollow shaft brushless motors, in order to assure high actuation performances under aerodynamic loads. Moreover, particular attention was given to the analysis of the cruise operation of the device: two dimensional unviscid vortex lattice method (VLM) was used to calculate pressure coefficient distribution along the wing in correspondence of the tab deflection of 5° , dynamic pressure $q_\infty=16074.45 \text{ N/m}^2$ and dive speed $V_{\text{DIVE}}=162 \text{ m/s}$. The airfoil geometry for the VLM calculations is shown in Figure 4.27.

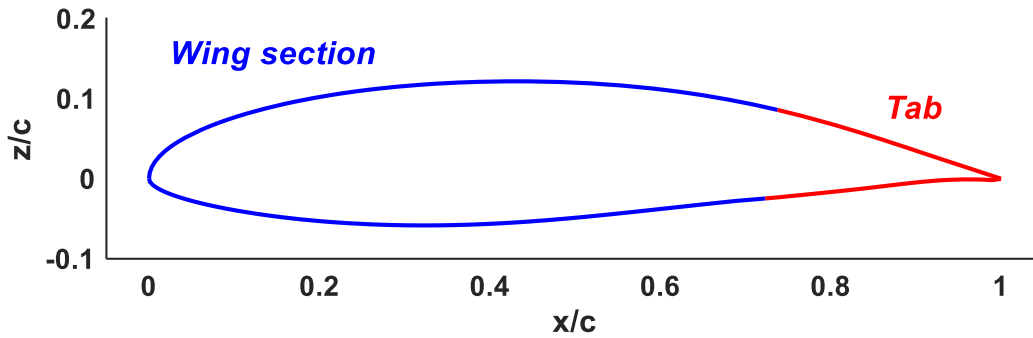


Figure 4.27. Wing root airfoil: focus on the tab segment.

The 2D pressure coefficient at the hinge of the tab, with a deflection angle of 5° , was calculated both on the upper and lower side of the airfoil, (4.3), (4.4).

$$C_{p_{upper}}(\delta = 5^\circ) = 0.33 \quad (4.3)$$

$$C_{p_{lower}}(\delta = 5^\circ) = 0.50 \quad (4.4)$$

$$p_{upper} = q_\infty C_{p_{upper}} \quad (4.5)$$

$$p_{lower} = q_\infty C_{p_{lower}} \quad (4.6)$$

Assuming for the tab segment a chord length c_{tab} of about 0.24 m and a span-wise b_{flap} of 5.17 m, the resultant aerodynamic force F for both upper and lower surface are given by (4.7) and (4.8).

$$F_{upper} = p_{upper} b_{flap} \left(\frac{c_{tab}}{2} \right) \quad (4.7)$$

$$F_{lower} = p_{lower} b_{flap} \left(\frac{c_{tab}}{2} \right) \quad (4.8)$$

$$H_{upper} = F_{upper} \left(\frac{C_{tab}}{3} \right) \quad (4.9)$$

$$H_{lower} = F_{lower} \left(\frac{C_{tab}}{3} \right) \quad (4.10)$$

The aerodynamic moment h_{tab} with respect of the hinge line of each block 3 is about 70 Nm, (4.11).

$$H_{total} = H_{upper} + H_{lower} = \sum_{i=1}^9 h_{tab_i} \quad (4.11)$$

4.5.2 Actuation Concept Layout and Control Scheme

Kinematic input

The kinematic transmission chain already outlined, which includes an electro-mechanical actuator, a speed reducer and a rotary sensor on hinge axis, has been extended to the application of the flap within Clean Sky 2 too. Anyway, it has been estimated a 50% weight saving, with good uncertainty range, in particular 92.5 Kg vs. 183 Kg of previous architecture and 37% of total weight related to electronic systems. Morphing flap demo will be bigger and lighter with less actuators. Relying upon the available space and taking in account specific constraints in terms of efficiency, power and reliability, the Kollmorgen™ brushless motor KBMS-10 was down-selected. Three actuation groups were considered adequate to move the whole structure in operative conditions. They were respectively linked to the 2nd, 4th and 7th bay and duly coupled to Harmonic Drive™ gearboxes (model HFUC-17-100-2UH), hosted by ribs blocks and acting as amplifiers of the actuation torque (and reducers of the shaft rotation speed). In Figure 4.28(a), the optimal morphing shape consisting of (4.5°, 10.5°, 10°) angles sequence with respect to the three hinge axes is shown. In view of the realization of the final full-scale prototype, the project involved the development of a technological demonstrator representative of only two bays, for the validation of design choices, Figure 4.28(b).

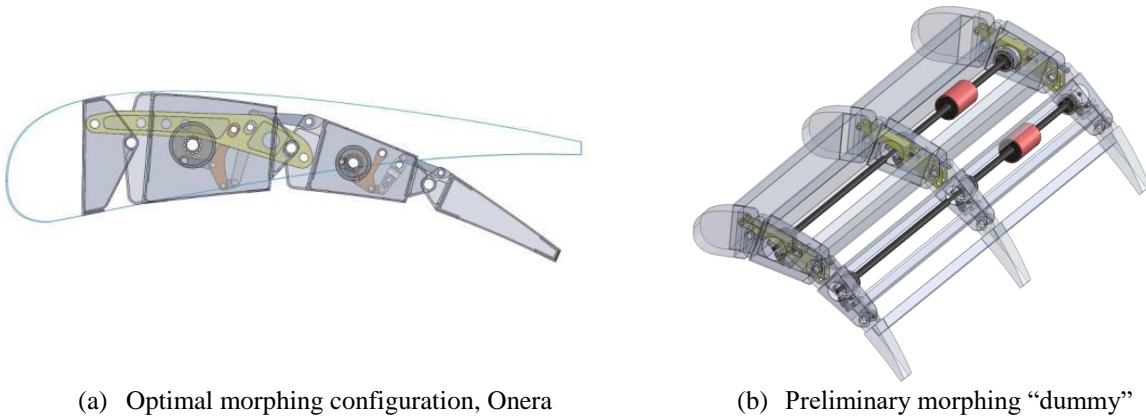


Figure 4.28. Prototype design.

Feedback strategy

The design process is flowing towards an increasingly “robotized” system, which can be externally controlled to perform certain operations, [36]. According to design specifications, a multi-axis actuation system including 6 electro-mechanical actuators (2 for the “dummy” demonstrator) by different gear-ratio combination for synchronized motion was assessed, in order to deploy the flap shape transition from the baseline configuration to a set of design target shapes in operative conditions, [7]. Motion control systems

involve the use of computation and feedback to control the movement of a mechanical system. The simplest independent-joint control strategy is to control each joint axis as a single-input multi-output (SIMO) system: in such a way, the ability to move individual actuators to different targets b/w inboard and outboard flap as well as b/w different stations, may lead to significant safety benefits, [37]. Additionally, failure of a controller does not imply the interruption of operation of the entire system. In recent years, independent-joint control schemes based on the complete dynamic model of the robot manipulators have been proposed for many industrial applications. This represents a design innovation compared to the previous architecture in which the management of the control was entrusted to a single master servo-driver. It is therefore necessary to define a control layout of each electro-mechanical actuator. The electric DC motor can be modelled according to Figure 4.29: the voltage V is applied which produces a current I in the armature circuit through the dynamics induced by the resistance R and the inductance L . A back E.M.F. component E , proportional to the motor angular speed ω_m , is also considered.

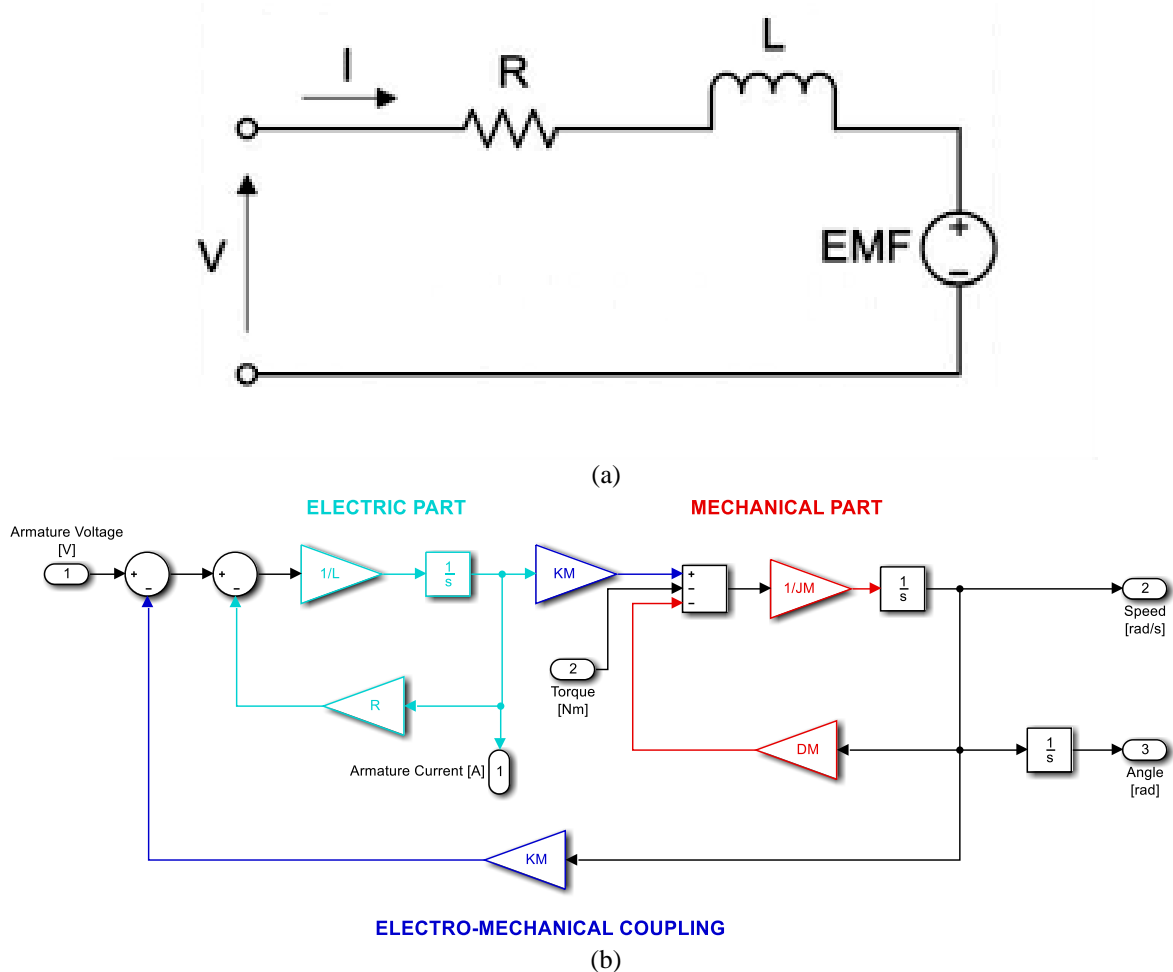


Figure 4.29. Actuator schematization: (a) electrical scheme and (b) Simulink[®] model.

A preliminary way to approach the motion control issue is to consider the servo-mechanism (motor, load, and gear-box) as a “rigid” system. However, previous experiences (Chapter 2) highlighted that the actuation system elasticity influences the dynamic behaviour of the morphing device. The more realistic way representative of the non-rigid behaviour of the system, includes an elastic coupling between motor and load (Figure 4.30).

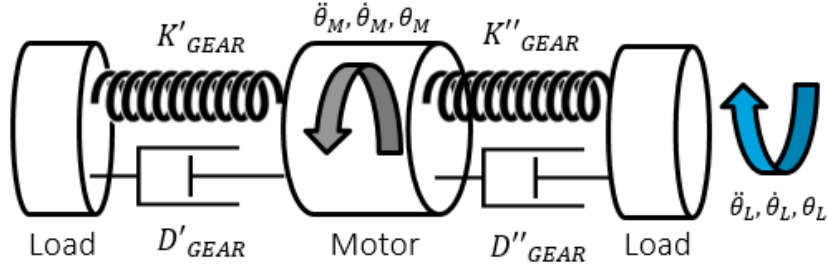


Figure 4.30. Lumped model: actuator, gear-box and structural load.

In this special case the dynamics equations are represented by:

$$J_M \ddot{\theta}_M + D_M \dot{\theta}_M = T_M - T_{MS} \quad (4.12)$$

$$J_L \ddot{\theta}_L = n T_{MS} - T_L \quad (4.13)$$

$$T_{MS} = K_{GEAR} (\theta_M - n \theta_L) - D_{GEAR} (\dot{\theta}_M - n \dot{\theta}_L) \quad (4.14)$$

Where J_M and J_L are respectively the motor and structural load moments of inertia, D_M the motor viscous friction coefficient, n the transmission ratio, T_{MS} the transmitted torque on the motor side, T_L the external torque perturbation on the load side and T_M the actuator torque. The elastic and dissipative effects of transmission are included in K_{GEAR} and D_{GEAR} . The status variables are defined both on the motor axis (θ_M and its time derivative) and on the load side (θ_L and its time derivative). With reference to the feedback transducer, a single rotary sensor can be coupled to each actuator. The feedback action could be therefore provided at blocks 1 and 3: the gear-ratio of block 2 is assumed to be ensured by the rigid leverage inside the rib. The present study is focused on the development of the position control for a ground demonstrator. Although position control is desired, it is needed to integrate a torque control to guarantee that the right torque is always supplied to the load by the motor. Torque control is realized with a current controller because:

$$T_M = K_M I(t) \quad (4.15)$$

in which the term K_M (motor constant) constitutes the electro-mechanical coupling.

Here is a sample illustration representative of a decentralized multi-loop control for each joint, Figure 4.30. A cascade configuration respectively implementing a P controller on the position, a PI controller on the velocity and torque, ensures that such laws are tracked on the basis of the values of the target position, shaft velocity and maximum current signals, minimizing so the shape error, [39-40]. An extra feed-forward action can be considered as a design solution in the present study to improve the system response when a “faster” signal is required. The implementation of a current loop is useful to protect the actuator’s motor against overcurrent. Such control scheme is very suitable for low-speed tracking, e.g. the camber-morphing trajectory in which the time spent to reach the desired deflection is such that a “quasi-static” state evolution may be assumed. The control issue of a morphing structure concerns mainly the definition of the input signals for the actuators in order to achieve a position set-point for the global plant: the three motion profiles can be reproduced according to a multi-loop control-based architecture, Figure 4.30. The control layout of single actuator is therefore represented as state-space system in Figure 4.31. For the present application, in which two variables are expected to be controlled (speed on the motor axis and position on the hinge axis), two transfer functions must be analysed, (4.16) and (4.17):

$$G_{VM}(s) = \frac{\mu \frac{s^2}{\omega_z^2} + 2 \frac{\zeta_z s}{\omega_z} + 1}{s \frac{s^2}{\omega_p^2} + 2 \frac{\zeta_p s}{\omega_p} + 1} \quad (4.16)$$

$$G_{LM}(s) = \frac{1 + 2\frac{\zeta_z s}{\omega_z}}{\frac{s^2}{\omega_z^2} + 2\frac{\zeta_z s}{\omega_z} + 1} \quad (4.17)$$

In particular, the frequencies ω_p and ω_z represent respectively the natural frequency of the system, i.e. the coupled system vibrates at the frequency of the pole of G_{VM} (velocity transfer function), and the “locked” frequency (calculated by the zero of G_{VM} transfer function). Such frequencies are equal to:

$$\omega_z = \sqrt{\frac{K_G}{J_{LR}}} \quad (4.18)$$

$$\omega_p = \omega_z \sqrt{1 + \frac{J_{LR}}{J_M}} \quad (4.19)$$

In which $J_{LR} = J_L/n^2$ and $\mu = 1/(J_M + J_{LR})$.

The reduction ratio assumed for gear-box is respectively equal to 100:1 for the HD[®] and 5:1 for the kinematic leverage.

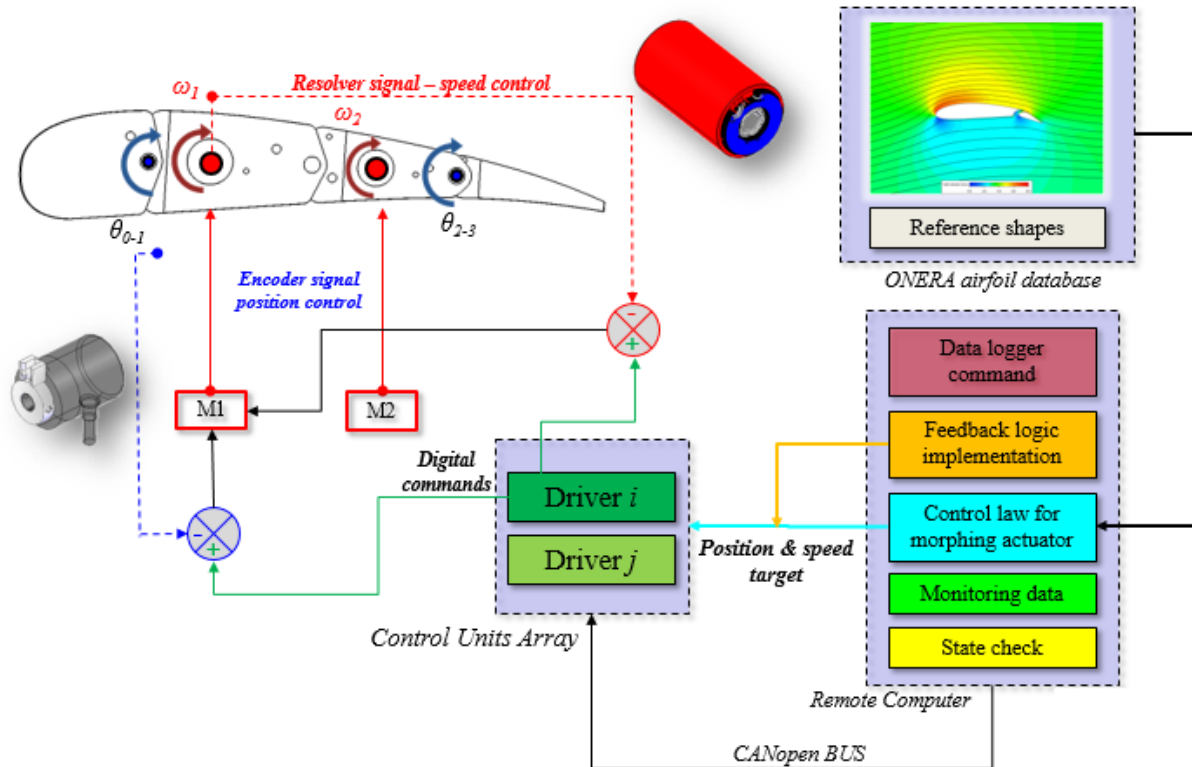


Figure 4.31. Decentralized control loop architecture of morphing rib and remote computer set-up.

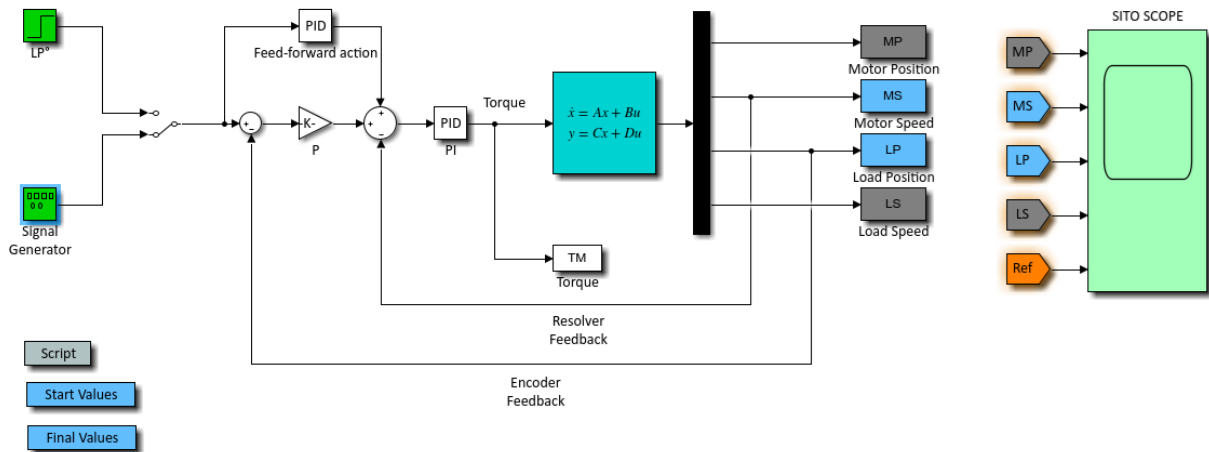


Figure 4.32. Simulink model of the single joint.

A Ziegler and Nichols approach was used for tuning the multi-loop controller within Matlab® environment. Time signals representing actuators input were considered in order to evaluate the controller performance as well as its stability. The shape of G_{VM} is characterized by singularities due to the terms of elasticity and damping effects, Figure 4.33.

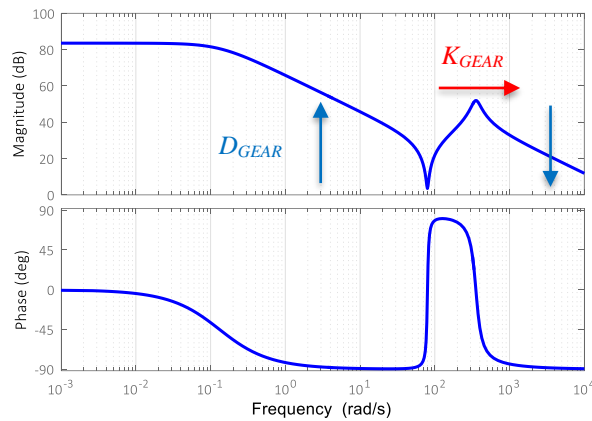


Figure 4.33. Bode diagram – sensitivity study of elastic and dissipative terms.

A trade-off iteration was carried out as the speed reducer stiffness was changed: finally, the value of the reducer chosen for the demonstrator, i.e. Harmonic Drive™ ($K'_{GEAR} = K''_{GEAR} = 16000 \text{ Nm/rad}$) has revealed a shift of the peak well outside the field of interest of the control. The trend is in fact representative of a low-pass filter of a quasi-rigid mechanism, Figure 4.34.

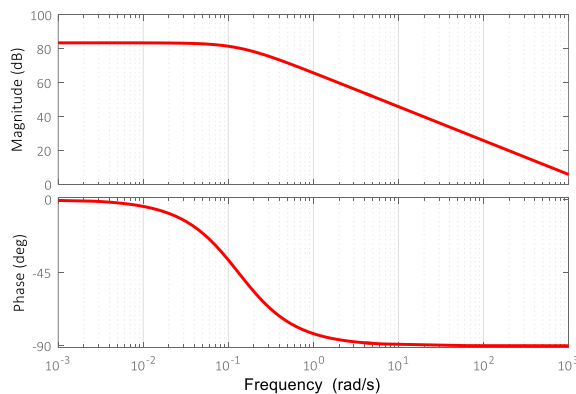


Figure 4.34. Bode diagram – $K'_{GEAR} = K''_{GEAR} = 16000 \text{ Nm/rad}$.

Finally, the gains determined by the preliminary model to concentrated elements have been included in an executive scheme of the actuator, Figure 4.35. The actuator has been modelled according to Figure 4.29(b). Some simulative results relative to the future 2-bay demonstrator are represented in Figure 4.36 and 4.37. The controller was tested through numerical simulations. The input to the controlled actuator was the difference between the target and achieved rotation. The resulting performance was compared with that achieved by an open loop control with the actual motor position estimated by a virtual absolute encoder directly geared to the hinge. They confirm that the nested-based strategy can be successfully used for morphing applications.

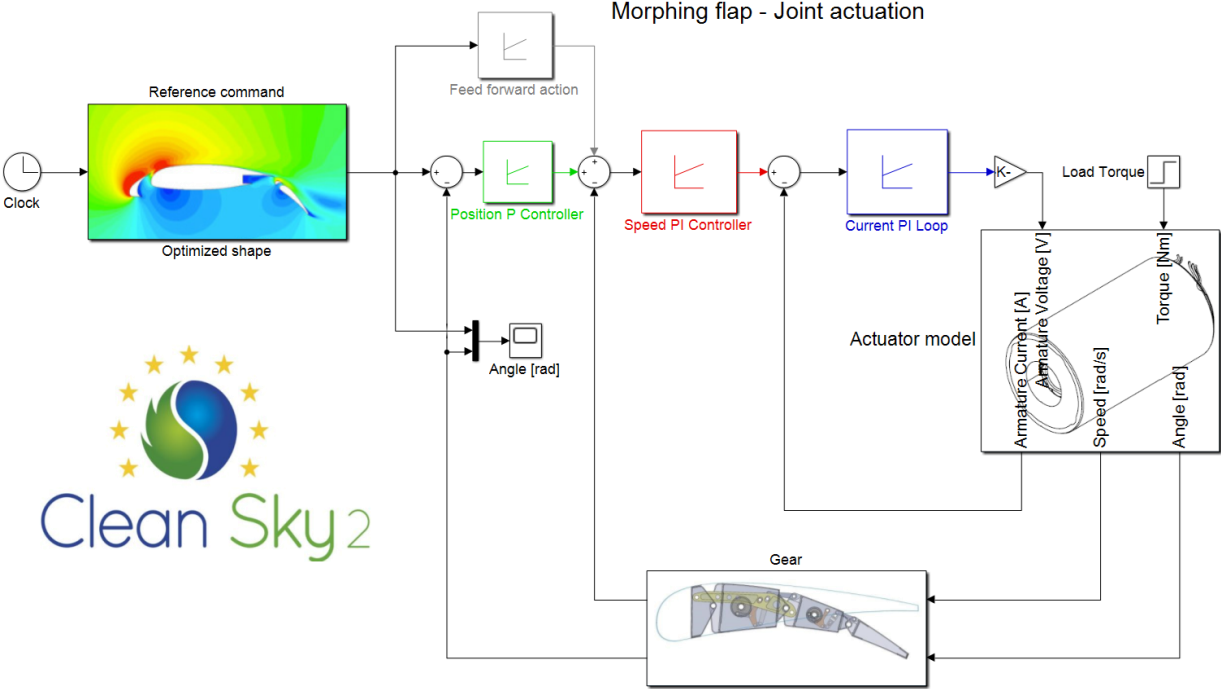


Figure 4.35. Executive representation of SISO control.

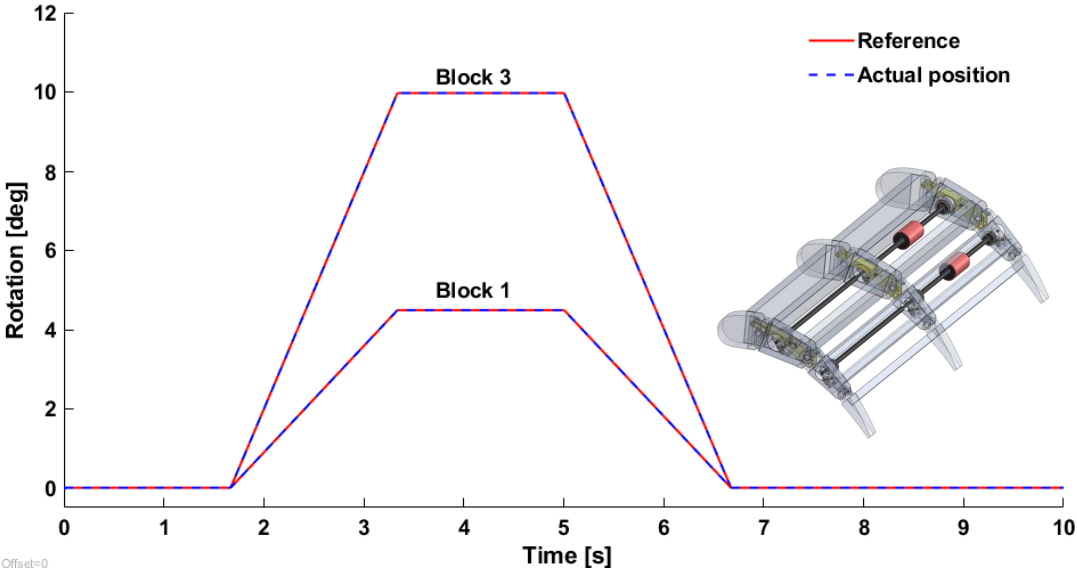


Figure 4.36. Trajectory in morphing mode.

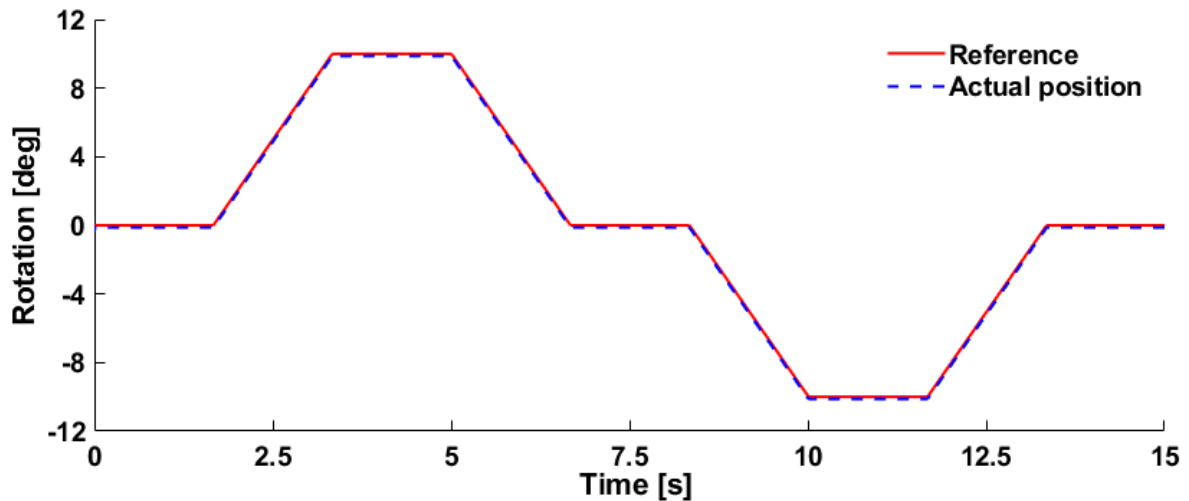


Figure 4.37. Trajectory in tab mode.

4.5.3 Compatibility with other electric devices

To further improve the benefits brought by such technology on the wing aerodynamic efficiency, an active flow control system based on Plasma Synthetic Jet (PSJ) actuators was investigated for a potential installation on the upper skin of the flap. PSJ actuators, or Sparkjets, are able to produce very high jet velocities, without the aid of any moving parts, affecting the structure of the flow-field to be controlled and allowing a positive variation of the aerodynamic forces on aircraft. This work faces the two main aspects related to the integration of the PSJ technology into the adaptive flap skin: the thermal and electro-magnetic interferences of the devices with the actuators and other electronic equipment of the flap. Due to the complexity of the interactions among the many elements and parameters that are involved, a very clear and simple way for addressing the “who-does-what” of an electro-magnetic interference (EMI) situation is the source and victim concept. It states that an EMI problem may be viewed as an interaction among three players, Figure 4.38:

- the source of EMI, which can be a natural phenomenon as lightning, or device that generates high frequency intentionally or as a byproduct of their operation (digital circuits and switch mode power supplies);
- the victim of EMI, which can be any analog or digital circuit whose low-level input can be activated, and eventually damaged by undesired signals;
- the coupling mechanism between source and victim, which can be a conducted path, a radiated path or an in-between like cable-to-cable crosstalk. These three elements are needed on the stage for the performance to exist.



Figure 4.38. EMI logical chain.

Essentially all coupling mechanisms that are conveying the source emissions up to the victim’s input are spectral-dependent: as frequency increases, the coupling coefficient increases. In some cases, it may even aggravate as frequency squared. Proper EMC tests are verified by the emission and the susceptibility levels. The emission levels of the equipment suggest when they are potential sources of interference to close systems, or more generally to the outside environment. This is accomplished by measuring the amplitude of high frequency noise that is emitted by conduction and by radiation, with specific instrumentation. It is

then compared to the applicable norms. The susceptibility levels of the equipment represent instead when they are confronted to the many electro-magnetic risks of their surrounding environment. This is accomplished by simulating an exposure to severe conducted or radiated disturbances, while checking that the equipment under test is still functioning properly. Experimental measurements were carried out to characterize the thermal and electro-magnetic fields induced by the operating device into the surrounding structure. A simplified test article was designed and manufactured to support all experimental activities while being fairly representative of the actual PSJ-skin assembly. Test results will allow for defining the safety-critical areas for the installation of flap actuation, control and sensing systems, Figure 4.39.

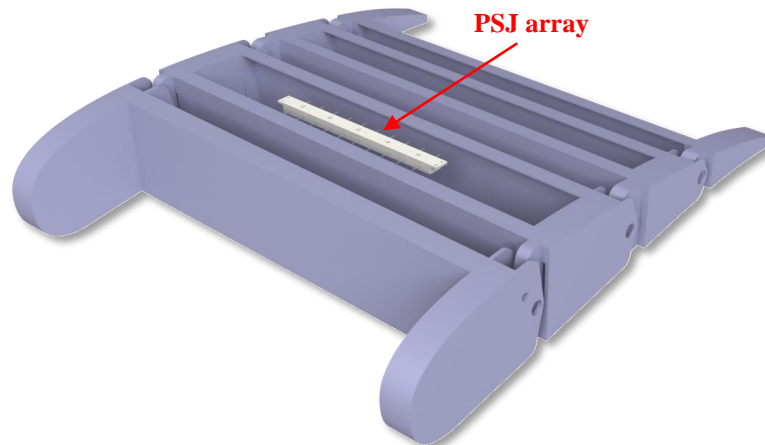


Figure 4.39. Morphing flap bay, focus on PSJ installation area.

A plasma synthetic jet actuator is a device developed at the beginning of the century, which soon has become the object of study of several research groups, [40-42]. It is mainly composed of 2 or 3 electrodes embedded in a small cavity linked to the external environment through an orifice. The operating cycle begins with an electrical discharge between the electrodes, which increases sharply pressure and temperature inside the cavity. The high-pressure air exhausts through the orifice, converting the increased internal energy into kinetic one. In the end, fresh air is drawn back inside the cavity, refilling the device for the next pulse. After a limited number of cycles, the device reaches a periodic behavior, generating a synthetic jet. In the last few years the interest of the scientific community on this topic has grown considerably, producing several numerical and experimental contributions. Being a very recent technology, many works were focused on the device response [43-44], varying the operating and the geometric conditions, with few works on the interaction with a boundary layer [45] or in cross-flow conditions, [46]. At the same time, different numerical simulations, [47-48] and physical models [49-50] have been developed to predict the behavior of the device and to investigate its main characteristics. Following the research line of the lumped models [51-52], a novel physical model, able to predict the time variation of all thermodynamic quantities in the cavity as well as the jet velocity at the orifice, was reported in [53]. This contains also details of the PSJ actuators used for this analysis. The power supply system is mainly constituted of a high-voltage trigger device and an external supply system (sustain device). To explain its working principles, it is convenient to introduce two sub-circuits: the *trigger circuit*, composed of an internal DC power supply and a trigger transformer, which quickly (in a few μs) raises the voltage (from 1.5 to 12 kV) between the electrodes producing a first trigger spark; the *sustain circuit*, composed of an external DC power supply (whose discharge time is controlled by a Mosfet transistor) a mixer and an electrical ballast, can provide a voltage up to 600 V, which by itself it is not able to produce a spark between the electrodes. The operating cycle starts with a high-voltage trigger pulse to produce a channel between the electrodes, that reduces the breakdown voltage below the electrodes voltage provided by the sustain circuit; so, when the Mosfet is turned on an electrical arc is formed inside the cavity. The purpose of the trigger spark is to momentarily reduce the local breakdown voltage between the anode and the cathode and to define the actuation frequency; whereas, the amount of energy provided to the fluid in each cycle can be controlled with the external power supply, by varying the sustain voltage, or through the Mosfet transistor,

by changing the duration of the discharge. Figure 4.40 presents a very interesting comparison of the device operating electrical phases. The first-row reports only the actuator bottom part; the second one, instead, shows the whole device. Starting from the left, it is possible to examine the device in the turned off condition, then during the trigger mode phase and, finally, during the operating regime. Note that without the top part both electrical arcs are clearly visible, with the sustain one being more intense. On the other hand, putting the cup on the device, the high-voltage trigger discharges are barely appreciable and, due to their short duration, the energy supplied to the fluid is negligible; on the other hand, in operating conditions the energy discharges are clearly visible leading to the PSJ formation.

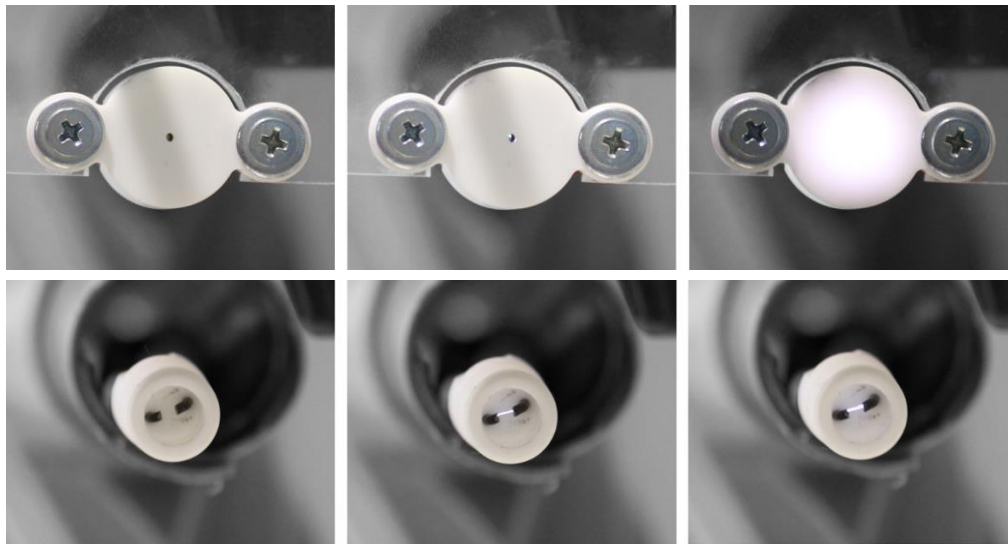


Figure 4.40. Actuator operating electrical phases. Device bottom part only (top row) and whole device (bottom row).

The electric and the magnetic fields produced by the actuator were measured with a PMM 8053A test device. The system consists of various electric and magnetic field probes and of a compact and portable meter equipped with a wide LCD display, 4 simple function keys (which allow different actions and settings, in accordance with the selected menu), internal rechargeable batteries and fiberoptic interfaces. The magnetic field probe was a EHP-50C, connected to the device through a fiber optic cable (FO-8053/10), with a frequency range of 10 Hz – 5 kHz, a resolution of 1 nT and an absolute error of ± 0.4 dB. The probe, reported in Figure 4.41, was vertically aligned to the device and placed at a distance of 0.3 m, corresponding to the distance with the morphing flap actuators, [54-55].

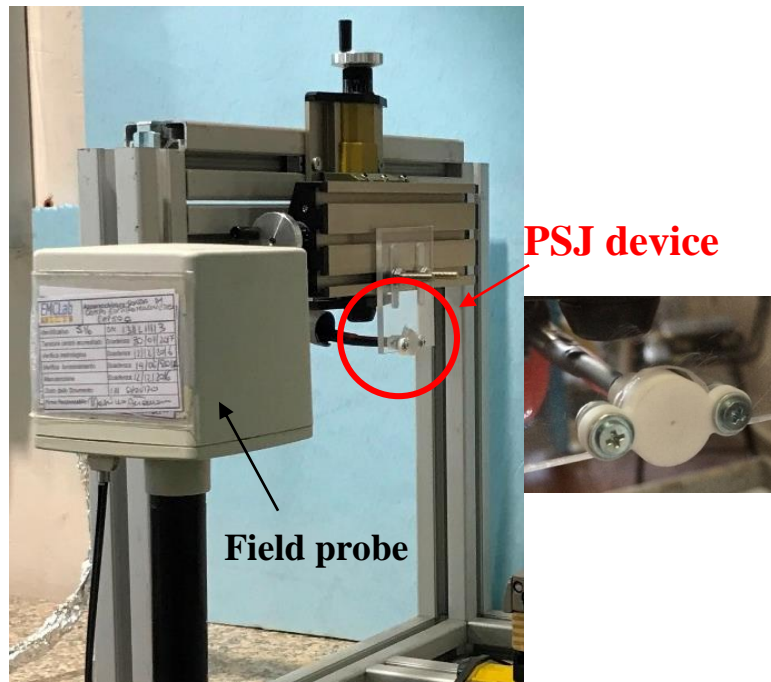


Figure 4.41. Electro-magnetic field probe, EHP-50C, position with respect the PSJ device.

This first preliminary experimental campaign was conducted in facilities of the Aerospace sector of the Industrial Engineering Dept., therefore a measurement of the typical electrosmog of the facility, before starting the device characterization, was detected and reported in Figure 4.42. The spectrum of the electric field (E) shows a first peak, located at a frequency $f=50$ Hz, corresponding to the standard power supply system, and its multiples; the total wideband (0 – 2 kHz) electric field value measured is equal to 13.21 V/m. This value must be subtracted from the subsequent measurements.

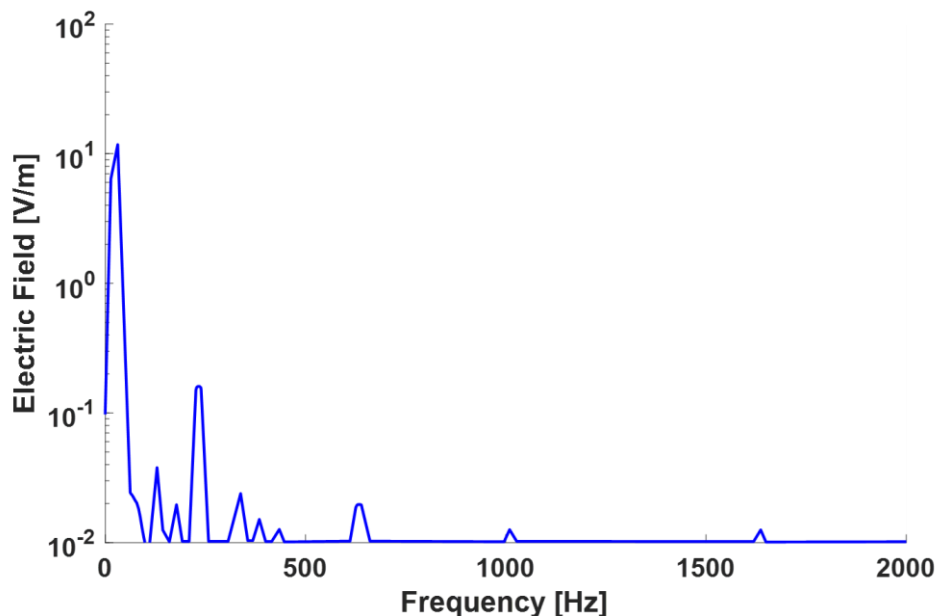


Figure 4.42. Facility electrosmog, (0 – 2 kHz).

Once that the background electrosmog was detected, the electrical interference measurements produced by the trigger sparks (Figure 4.43) and that ones generated by the sustain discharges (Figure 4.41), corresponding the operative conditions, were acquired. The measurements were conducted with an

actuation frequency of 1 kHz, a duty cycle of the 12% and with a power consumption of 3.85 W. The electrical field, produced by the device with the trigger discharges only, exhibits a first peak, which correspond to the actuation frequency with the greatest energy content, and secondary spikes, representing super-harmonics of the previous signal, with decreasing electrical values.

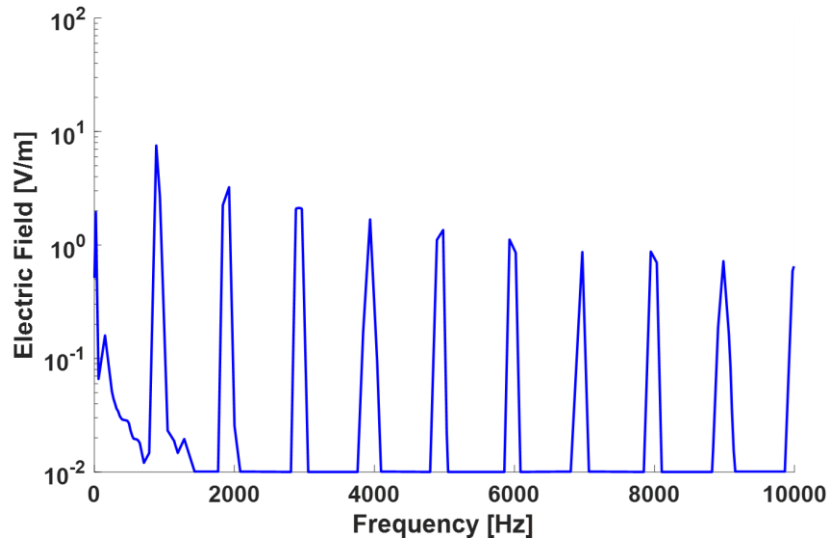


Figure 4.43. Spectrum measured with only the trigger discharge, (0 – 10 kHz).

The FFT analysis, in operative conditions, once again allowed for highlighting the frequency energy content of the signal in the 2 kHz windowing range. During the operating function, the harmonic peaks can be still appreciated, but the sustain discharge produces a noise distributed in all the spectrum (Figure 4.44), probably due to the electrical components of the sustain circuit (especially to the Mosfet transistor), which regulate the duration and the intensity of the energy discharge. The total wideband value measured in these conditions is equal to 69.20 V/m. Preliminary measurements show that the spectral content of the disturbance may be really reduced shielding the power supply wires (Figure 4.45). Indeed, after the shielding, the electric field measurements show a sensible reduction up to 17.37 V/m.

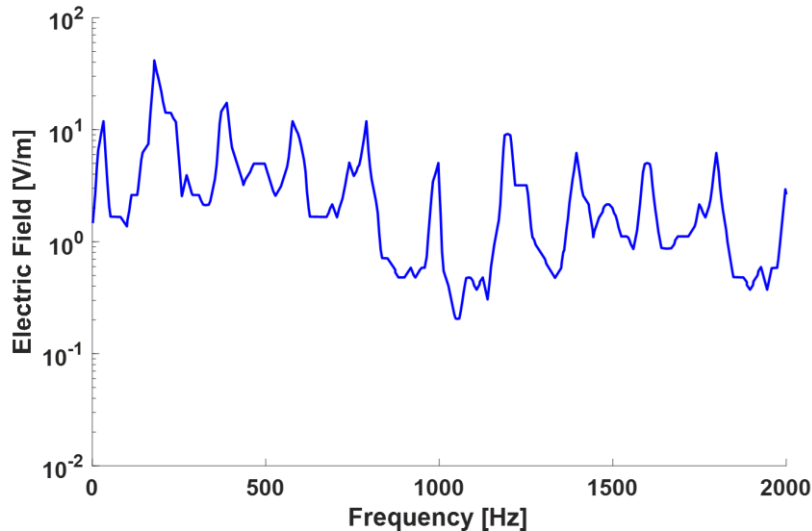


Figure 4.44. Spectrum measured during the operative conditions, (0 – 2 kHz).

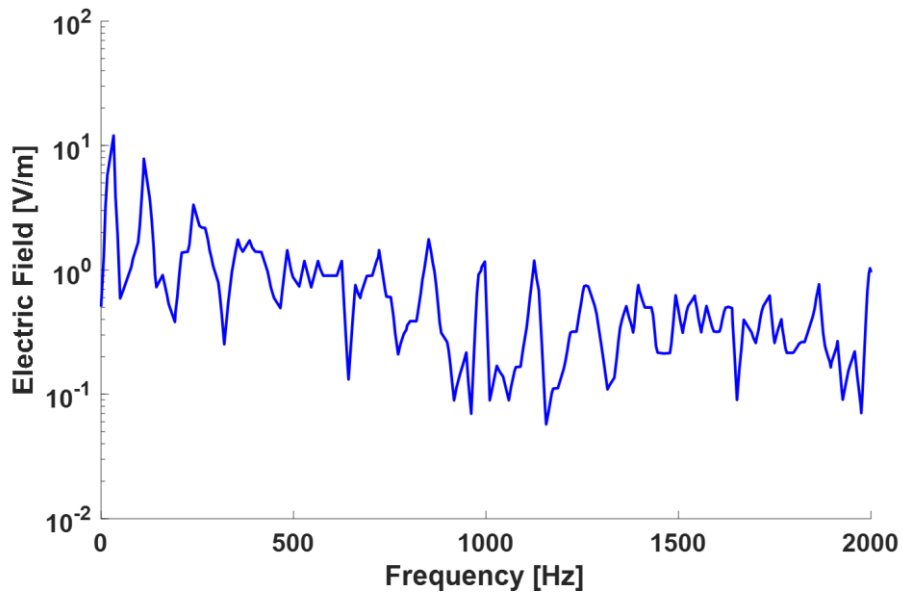


Figure 4.45. Spectrum measured during the operative conditions with shielded wires, (0 – 2 kHz).

For all the previous measurements, the magnetic field produced by the actuator was always lower than 1 μT , producing a negligible magnetic field. At the same time, the actuator external temperature was acquired with a FLIR SC6000 Series Infrared Camera, placed at 1 m from the device and an angle of 45° respect the jet stream-wise direction. In the case of MACOR (ceramic material) the emissivity coefficient has been considered equal to 0.8. During this campaign, the device was mounted on a plexiglass support. Figure 4.46 reports the temperature field acquired by the infrared camera, with a power consumption of 7 W; it is worth noting that the heated area is located in a narrow zone close to the device and after a few cavity diameters the device does not affect the surrounding structure.

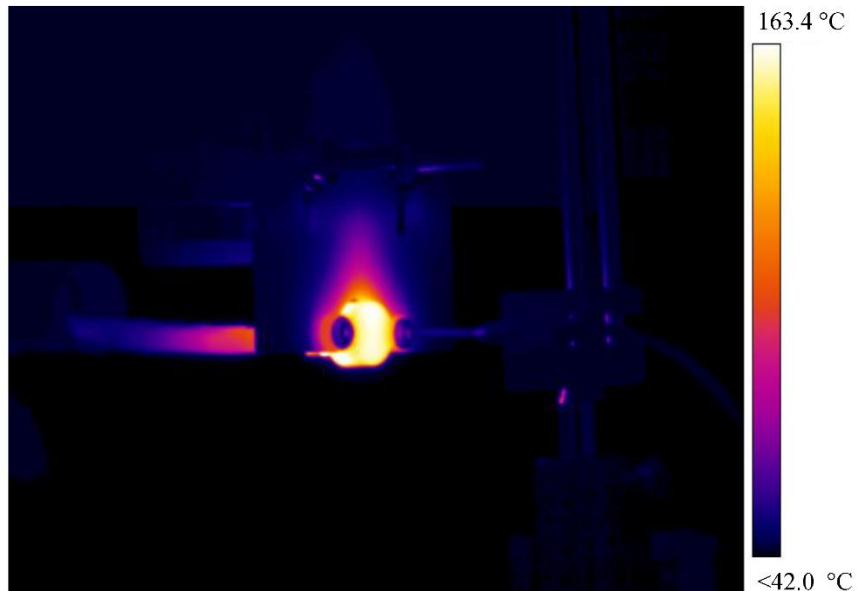


Figure 4.46. Temperature field acquired with the Flir SC6000 infrared camera.

4.6 Conclusions and next activities

In the framework of Clean Sky-JTI project, author investigated a high TRL solution for an innovative flap element tailored for regional transportation aircraft end application. The conceived device was designed in order to enable two different shape morphing modes depending on aircraft flight condition and flap setting. Geometrical dimensions and design loads related to a true-scale flap segment of 3.6 m span were considered for the definition and validation of the morphing flap actuation system.

A full scale prototype was finally manufactured and tested to:

- demonstrate the morphing capability of the conceived structural layout;
- demonstrate the capability of the actuation system to withstand static loads representative of the limit aerodynamic pressures expected in service.

Rational approaches were implemented in an efficient test campaign providing the necessary database for the mechanical demonstration of the morphing structure.

Test outcomes showed that: reliable, controllable and stable morphing compliant with design requirements is assured by the device for both morphing modes. The encouraging outcomes achieved have led to the design of a new architecture of morphing flap. Relying upon the already assessed concept, an innovative and more advanced flap device was designed in order to enable up to three different morphing modes on the basis of the A/C flight condition/flap setting. The chapter has illustrated the preliminary design of a decentralized multi-loop system to control the motion of the actuated ribs of a morphing flap, conceived to perform up to three operating modes. The robotized system has been schematized through a mathematical model within Matlab/Simulink® environment, which allowed for simulating the control laws of the ground demonstrator. The whole actuation chain, including actuator and gearbox, has been sized by the static loads representative of different flight conditions. Mechatronic systems based on non-rigid connections often have resonance frequencies, which can affect controller performance limiting its operating bandwidth. The hypothesis of very high transmission ratios (about 1:500 for each actuated block) needed to compensate the resistant torque, made it possible to implement a model based on the independent control of the joints. The design is made robust by closing more feedback loops that use position, speed and required torque information. Moreover, when the request of performance increases in terms of “faster” trajectories (i.e. with higher values for the velocity signals), typically a tracking degradation takes place, therefore the “disturbance” becomes more relevant. An extra feed-forward action, which can be computed by the values of the desired position has been considered as a valid solution in the present study. The positive benefits related to the addition of a feedback controller are widely known: disturbance rejection, larger bandwidth for the controlled system than the open-loop system and much more robustness with respect to parametric uncertainties. Further experimental campaign will be executed on a 2-bay demonstrator to verify the effectiveness of the proposed control technique. With respect the design of electronic hardware systems, the EMC test represents a significant task. In connect with EMC test for a certain aircraft and its electric subsystems, it has been put forward a test program for aircraft AC/DC power supply system characteristics, electro-magnetic emission, electro-magnetic susceptibility, and electro-magnetic environment and antenna couplings. To further improve the benefits brought by such technology on the wing aerodynamic efficiency, an active flow control system based on PSJ actuators was investigated for a potential installation on the upper skin of the flap. The discussed work is focused on the two main aspects related to the feasibility of PSJ actuators integration into the adaptive flap skin: the thermal and electro-magnetic interferences of the actuators with the other electronic equipment of the flap. Experimental measurements were carried out to characterize the thermal and the electro-magnetic fields induced by the operating device into the surrounding structure. A test article representative of a skin segment has been designed and manufactured to support all testing activities. The electro-magnetic field produced by the device, after appropriate shielding, seems to be compatible with the typical devices mounted within the morphing flap. Furthermore, the PSJ actuators could thermally affect only a small portion of the flap skin. This preliminary experimental investigation allowed for a definition of the safety-critical areas for the installation of flap electric actuation, control drivers and sensing network.

References

- [1] ACARE official site: <http://www.acare4europe.com/>.

- [2] Official site of Clean Sky consortium: <http://www.cleansky.eu/>.
- [3] Pecora, R., Amoroso, F., Magnifico, M., Dimino, I. and Concilio, A.: KRISTINA: Kinematic Rib based Structural system for Innovative Adaptive trailing edge, SPIE Smart Structures/NDE, Las Vegas, Nevada (USA) March 2016. Proc. SPIE 9801, Industrial and Commercial Applications of Smart Structures Technologies 2016, 980107 (2016); 10.1117/12.2218516.
- [4] Pecora, R., Concilio, A., Dimino, I., Amoroso, F. and Ciminello, M.: Structural Design of an Adaptive Wing Trailing Edge for Enhanced Cruise Performance, 24th AIAA/AHS Adaptive Structures Conference, AIAA SciTech, 4-8 Jan (2016).
- [5] Dimino, I. Diodati, G., Concilio, A., Volovick, A., Zivan, L.: Distributed Electromechanical Actuation System Design for a Morphing Trailing Edge Wing”, SPIE Smart Structures/NDE, Las Vegas, Nevada (USA) March 2016. Proc. SPIE 9801, Industrial and Commercial Applications of Smart Structures Technologies 2016, 980108 (April 16, 2016), 10.1117/12.2219223.
- [6] Wildschek A., Grünewald M., Maier R., Steigenberger J., Judas M., Deligiannidis N., and Aversa N.: Multi-Functional Morphing Trailing Edge Device for Control of All-Composite, All-Electric Flying Wing Aircraft, Proceedings of the 26th Congress of International Council of the Aeronautical Sciences (ICAS), Anchorage (Alaska), September 14-19, (2008).
- [7] Amendola, G., Magnifico, M., Pecora, R., Dimino, I.: Distributed Actuation Concepts for a Morphing Aileron device, The Aeronautical Journal, 120(1231), 1365–1385 (2016), 10.1017/aer.2016.64.
- [8] Dimino, I., Concilio, A., and Pecora, R.: Safety and Reliability Aspects of an Adaptive Trailing Edge Device (ATED), 24th AIAA/AHS Adaptive Structures Conference, AIAA SciTech, 4-8 Jan (2016).
- [9] Dimino, I., Flauto, D., Diodati, G., Concilio, A., Pecora, R.: Actuation system design for a morphing wing trailing edge, Recent Patents on Mechanical Engineering, 7(2), 138–148 (2014).
- [10] Amendola, G., Dimino, I., Amoroso, F., and Pecora, R.: Experimental characterization of an adaptive aileron: Lab tests and FE correlation, in Proceedings of SPIE - The International Society for Optical Engineering, vol. 9803, (2016).
- [11] Amendola, G., Dimino, I., Concilio, A., Magnifico, M., and Pecora, R.: Numerical design of an adaptive aileron, in Proceedings of SPIE - The International Society for Optical Engineering, vol. 9803, (2016),
- [12] Concilio A., Dimino I., Diodati G., Pecora R., Magnifico M. and Schorsch O.: Damping levels induced by morphing skin on an adaptive trailing edge device (ATED), 24th AIAA/AHS Adaptive Structures Conference San Diego United States 4-8 January (2016).
- [13] Pecora, R., Barbarino, S., Concilio, A., Lecce, L., and Russo, S.: Design and Functional Test of a Morphing High-Lift Device for a Regional Aircraft, Journal of Intelligent Material Systems and Structures, 22(10), 1005–1023 (2011).
- [14] Pecora, R., Amoroso, F., Amendola, F. and Concilio, A.: Validation of a smart structural concept for wing-flap camber morphing, Smart Structures and Systems, 14(4), 659–678 (2014).
- [15] Rea, F., Arena, M., Noviello, M.C., Pecora, R., and Amoroso, F.: Preliminary failure analysis of an innovative morphing flap tailored for large civil aircraft applications, in Proceedings of 2016 7th International Conference on Mechanical and Aerospace Engineering, ICMAE 2016, 534–542 (2016).
- [16] Noviello, M.C., Rea, F., Arena, M., Pecora, R., and Amoroso, F.: Actuation and control of a novel wing lap architecture with bi-modal camber morphing capabilities, in Proceedings of 2016 7th International Conference on Mechanical and Aerospace Engineering, ICMAE 2016, 426–431 (2016).
- [17] Pecora, R., Amoroso, F., and Magnifico, M.: Toward the bi-modal camber morphing of large aircraft wing flaps: The CleanSky experience, in Proceedings of SPIE - The International Society for Optical Engineering, vol. 9801 (2016).
- [18] Pecora, R., Magnifico, M., Amoroso, F., Monaco, E.: Multi-parametric flutter analysis of a morphing wing trailing edge, Aeronautical Journal, 118(1207), 1063–1078 (2014).
- [19] Dimino, I., Concilio, A., Schueller, M., Grati, A.: An Adaptive Control System for Wing TE Shape Control, SPIE International Conference on Smart Structures 2013, San Diego, California, USA, (2013).
- [20] Hasse A. and Campanile L.F.: Design of compliant mechanisms with selective compliance, Smart Materials and Structures, 18(11), 1–10 (2009).
- [21] Baker D. and Friswell M.I.: The Design of Morphing Aerofoils using Compliant Mechanisms, Proceedings of 19th International Conference on Adaptive Structures and Technologies, Ascona (Switzerland), October 6-9, (2008).

- [22] Barbarino, S., Pecora, R., Lecce, L., Concilio, A., Ameduri, S., and De Rosa, L.: Airfoil Structural Morphing Based on S.M.A. Actuator Series: Numerical and Experimental Studies *Journal of Intelligent Material Systems and Structures*, 22, 987–1004 (2011).
- [23] Ameduri, S., Concilio, A. and Pecora, R.: A SMA-based morphing flap: conceptual and advanced design, *Smart Structures and Systems*, 16(3), (2015).
- [24] Ameduri, S., Concilio, A., Pecora, R., and Karagiannis, D.: A single slotted morphing flap based on SMA Technology, *Smart Structures and Systems*, 17(5), 819–835 (2016).
- [25] Bilgen O., Kochersberger K.B., Inman D.J., and Ohanian III O.J.: Novel, Bi-Directional, Variable Camber Airfoil via Macro-Fiber Composite Actuators, *Proceedings of the 50th AIAA/ASME/ASCE/AHS/ASC Structures, Structural Dynamics and Materials Conference, Palm Springs (California), May 4-7, (2009)*.
- [26] Browman, J., Sanders, B., and Weisshaar, T.: Evaluating the Impact of Morphing Technologies on Aircraft Performance, *Proceedings of the Forty-Third AIAA Conference on Structures, Structural Dynamics and Materials, AIAA Paper 2002-1631, April (2002)*.
- [27] Munday, D., and Jacob, J.: Active Control of Separation on a Wing with Conformal Camber”, *Proceedings of the Thirty-Ninth AIAA Aerospace Science Meeting and Exhibit, AIAA Paper 2001-293, January (2001)*.
- [28] Barbarino, S., Ameduri, S., and Pecora, R.: Wing chamber control architectures based on SMA: Numerical investigations, in *Proceedings of SPIE - The International Society for Optical Engineering, 2007, vol. 6423, article number 64231E*.
- [29] Blondeau, J., and Pines, D.: Pneumatic Morphing Aspect Ratio Wing, *Proceedings of the Forty-Fifth AIAA Conference on Structures, Structural Dynamics and Materials, AIAA Paper 2004-1808, April (2004)*.
- [30] Popov A.V., Grigorie T.L., Botez R.M., Mébarki Y., Mamou M.: Modeling and testing of a morphing wing in open-loop architecture, *Journal of Aircraft*, 47(3), 917–923 (2010).
- [31] European Aviation Safety Agency (EASA), *Certification Specifications and Acceptable Means of Compliance for Large Aeroplanes – CS-25, Amendment 11, July (2011)*.
- [32] Mingione G.: Preliminary Design of Wing Trailing Edge Morphing Architectures, JTI-GRA deliverable no. GRA2.2.1-TN-CIRAPlus-TECH-210105A, (confidential).
- [33] Pecora, R., Amoroso, F., Arena, M., Noviello, M.C. and Rea F.: Experimental validation of a true-scale morphing flap for large civil aircraft applications, *Proceedings Volume 10166, Industrial and Commercial Applications of Smart Structures Technologies 2017; 101660L (2017) <https://doi.org/10.1117/12.2259878>*.
- [34] Pecora, R., Amoroso, F., Noviello, M.C., Dimino, I., Concilio A.: Aeroelastic stability analysis of a large civil aircraft equipped with morphing winglets and adaptive flap tabs, *Proceedings of SPIE, Adaptive Structures and NDE Conference, Denver (CO, USA), September (2018)*.
- [35] Flore, L.: The use of complex power method in experimental modal analysis, *U.P.B. Sci. Bull., Series D, 78(2), (2016)*.
- [36] Arena, M., Noviello, M.C., Rea, F., Amoroso, F. and Pecora, R.: Control strategy of an electrically actuated morphing flap for the next generation green regional aircraft, *Proceedings Volume 10595, Active and Passive Smart Structures and Integrated Systems XII; 105950K (2018) <https://doi.org/10.1117/12.2296424>*.
- [37] Arena, M., Noviello, M. C., Rea, F., Amoroso, F., Pecora, R. and Amendola, G.: Modal stability assessment for a morphing aileron subjected to actuation system failures: Numerical analysis supported by test evidence,” *7th International Conference on Mechanical and Aerospace Engineering, ICMAE, 437–442 (2016)*.
- [38] Tchatchueng Kammegne, M. J., Botez, R. M., Grigorie, T. L., Mamou, M. and Mébarki, Y.: Proportional fuzzy feed-forward architecture control validation by wind tunnel tests of a morphing wing, *Chinese Journal of Aeronautics*, 30(2), 561–576 (2017).
- [39] Popov, A. V., Labib, M., Fays, J. and Botez, R. M.: Closed-Loop Control Simulations on a Morphing Wing, *Journal of Aircraft*, 45(5), 1794–1803 (2008).
- [40] Grossman, K. R., Cybyk, B. Z. and V. D. M.: Sparkjet actuators for flow control, in *41st Aerospace Sciences Meeting and Exhibit, Reno, Nevada, (2003)*.
- [41] Narayanaswamy, V., Raja, L. L. and Clemens, N. T.: Characterization of a high-frequency pulsed-plasma jet actuator for supersonic flow control, *AIAA Journal*, 48(2), 297–305 (2010).
- [42] Curuana, D., Rogier, F., Dufour, G. and G. C.: The Plasma Synthetic Jet Actuator, *Physics, Modeling and Flow Control Application and Separation, Journal Aerospace Lab*, 6, 1–13 (2013).
- [43] Popkin, S. H., Cybyk, B. Z., Foster, C. H. and Alvi F. S.: Experimental Estimation of SparkJet Efficiency, *AIAA Journal*, 54, 1831–1845 (2016).
- [44] Zong, H. and K. M.: Formation, evolution and scaling of plasma synthetic jets, *J. Fluid Mech.*, 837, 147–181 (2018).

- [45] Zong, H. and K. M.: Interaction between plasma synthetic jet and subsonic turbulent boundary layer, *Physics of Fluids*, 29(045104), (2017).
- [46] Chedeveigne, F., Leon, O., Bodoc, V. and Caruana, D.: Experimental and numerical response of a high-Reynolds-number $M = 0.6$ jet to a Plasma Synthetic Jet actuator, *International Journal of Heat and Fluid Flow*, 56, 1–15 (2015).
- [47] Laurendeau, F., Chedeveigne, F. and Casalis, G.: Transient ejection phase modeling of a Plasma Synthetic actuator, *Physics of Fluids*, 26(125101), (2014).
- [48] Laurendeau, F., Leon, O., Chedeveigne, F., Senoner, J. M. and Casalis, G., Particle Image Velocimetry Experiment Analysis Using Large-Eddy Simulation: Application to Plasma Actuators, *AIAA Journal*, 57(11), 3767–3780 (2017).
- [49] Sary, G., Dufour, G., Rogier, F. and Kourtzanidis, K.: Modeling and Parametric Study of a Plasma Synthetic Jet for Flow Control, *AIAA Journal*, 52(8), 1591–1603 (2014).
- [50] Zong, H., Wu, Y., Li, L., Song, H., Zhang, Z. and Jia, M.: Analytic model and frequency characteristics of plasma synthetic jet actuator, *Physics of Fluids*, 27, 1–21 (2015).
- [51] Chiatto, M., Capuano, F., Coppola, G. and de Luca, L.: LEM Characterization of Synthetic Jet Actuators Driven by Piezoelectric Element: A Review, *Sensors*, 17(6), 1216, (2017).
- [52] Chiatto, M., Marchitto, L., Valentino, G. and de Luca, L.: Influence of a Piezo-Driven Synthetic Jet on a Water Spray Behavior, *Atomization and Sprays*, 27(8), 691–706, (2017).
- [53] Chiatto, M. and de Luca, L., Numerical and Experimental Frequency Response of Plasma Synthetic Jet Actuators, *AIAA Paper*, 2017-1884, 1–16 (2017).
- [54] Arena, M., Chiatto, M., Amoroso, F., Pecora, R. and de Luca, L.: Feasibility studies for the installation of Plasma Synthetic Jet Actuators on the skin of a morphing wing flap, *Proceedings Volume 10595, Active and Passive Smart Structures and Integrated Systems XII*; 105950M (2018) <https://doi.org/10.1117/12.2300512>.
- [55] Chiatto, M., Arena, M., Palumbo, A., Pecora, R. and de Luca, L.: Plasma-Based Actuators for Flow Control: Recent Developments and Future Directions. *EUROMECH*. 14 March 2018 – 16 March 2018.

5. Self-Sensing System for Compliant Morphing Tab

Nowadays, smart composites based on different nano-scale carbon fillers, such as carbon nanotubes (CNTs), are increasingly being thought of as a more possible alternative solution to conventional smart materials, mainly for their improved electrical properties. Great attention is being given by the research community in designing highly sensitive strain sensors for more and more ambitious challenges: in such context, interest fields related to carbon nanotubes have seen extraordinary development in recent years. A smart structure as a morphing wing needs an embedded sensing system in order to measure the actual strain state as well as to “monitor” the structural conditions. Looking at these self-sensing perspectives for the next generation of composite structures, a strain sensor has been realized. The epoxy resin was first analysed by means of a micro-mechanical test, estimating the electrical resistance variations as function of the load, in order to demonstrate the feasibility of the sensor. Such intrinsic piezoresistive performance is essentially attributable to the re-arrangement of conductive percolating network formed by MWCNT, induced by the deformation of the material due to the applied loads. The specimens have been prepared within this investigation, to demonstrate their performance for a potential composite skin of variable-shape structures. Relying upon the results obtained on the dog-bone sample, the technological innovation has been extended to a coating that can be directly integrated on the skin surface. The nanotechnology can be considered a suitable way to make large scale monitoring: such aspect is extremely advantageous when compared to traditional glass fiber optic sensors. In fact, because of their high cost, it is not possible to create a dense network of these fibers to inspect large structural parts.

5.1 Research scenario

In recent years, much more attention has been turned to the design of nano filler for polymer materials to harness the exceptional electrical properties of CNTs, [1-20]. In particular, polymers with the incorporation of CNTs show great potential for microelectronic applications such as highly sensitive strain sensors for aeronautical smart systems. For such application, the direct current (DC) properties of nanocomposites are used. Currently, numerous experimental studies aimed to well characterize the electrical properties of nanocomposites, made from insulating polymers filled by CNTs, are being carried out. Polymer-based composite materials belong to the family of ultra-light structural materials, which have been introduced massively in the recent years in aeronautical applications, [21-25], but also in other fields like civil and automotive engineering as well. Moreover, the anisotropy of the elastic properties allows optimizing the performance of the structural materials, offering countless new design possibilities. Non-destructive testing and surveillance techniques have been developed over the years, mainly encouraged by the constant search of enhanced safety in the aeronautical industry and in civil engineering applications, [26-28]. However, the standard methods currently used are far from being optimal for these novel materials, and potential improvements in the continuous monitoring techniques are constantly being investigated. From this perspective, new strain monitoring systems have thus emerged during the last years as an interesting option. The potential of CNTs composite materials used as strain sensors can be used in order to monitor motion. In their particular experiment, Kong J.H. *et al.* in [29] realized conductive polydimethylsiloxane (cPDMS) strain sensors. They have been assembled on each finger joint of a glove using Velcro fasteners at both ends of the device, in order to monitor the motion of the human fingers in real-time. The changes in electrical resistance for cycling bending and straightening motions of the finger were detected, which indicated that the resistance was immediately increased with the applied bending deformation, and it is recovered gradually to its initial value at straightening. Moreover, the magnitude of the resistance change ratio could be clearly determined depending on the degree of finger bending. As well-known, in the engineering field - especially the aerospace one - the need for high-performance material properties, such as lightness, stiffness, damping and taking up a minimal amount of space, has greatly increased, involving consequently continuous technological research, aimed to get materials that are stiff, with high-damping capacity, anti-corrosive, sensorized and, above all, lightweight. This purpose leads to investments in research of new generation materials, especially multi-layered and multifunctional composite materials, which - with the addition of nanoparticles in their composition - gain those sought-after capacities. Sensorized materials can be effectively produced: these materials become sensors themselves without using external devices, embedded or attached. In this chapter, the research has been focus on assessing the resistivity properties of nano-composites for potential aeronautical applications and in particular for morphing structures. An intelligent structure must be able to measure in real-time its deformation state: the example of a morphing

wing is certainly useful to understand the ambitious realization of a sensing system for detecting strain variations under the action of the external load. More precisely, this last part of the thesis deals with a feasibility study into the incorporation of carbon nanomaterials into structural composites as sensors. Coupons made of MWCNTs embedded in typical aeronautic epoxy formulation were prepared and tested under different conditions in order to better characterize their sensing performance. Following a synergic collaboration among three partners as Smart Structures Lab (University of Naples “Federico II”), Chemical Lab (University of Salerno) and Material Research Centre (University of Bath), the team worked on the feasibility of multifunctional materials, [30-35]. The improvement of the structural properties has been verified by many perspectives: increase in damping, increase in sound absorption, greater resistance to flame, better resistance to lightning are some of the main aspects investigated in this international joint venture. The chapter focuses in particular on the possibility of implementing capacity in the common aeronautical resins. The team assessed a piezoresistive response of a MWCNTs epoxy resin to evaluate by means of mechanical tests the variation of the electrical resistance according to the deformations that the material has undergone. A resin strain sensor has been realized with the aim of looking for a more innovative strain monitoring tools for the next generation of composite structures, providing the most contemporary overview possible of carbon nanotube-based strain sensors for aeronautical application. Another emerged datum was that such intrinsic piezoresistive performance is essentially attributable to the re-arrangement of conductive percolating network formed by MWCNT, induced by the deformation of the material due to the applied loads. Relying upon the satisfying results achieved at sample level, the activity continued with the stratification of such resin on aeronautical Carbon Fiber Reinforced Plastics (CFRPs), designing a smart coating exhibiting self-diagnostic capability. The correlations between mechanical strain and electrical properties of coated CFRPs highlights the feasibility in manufacturing CFRPs having integrated high sensitivity in providing an effective real-time strain monitoring. Their components choice - the epoxy resin and the carbon nanotube concentration - allowed for preparing a conductive coating with high sensitivity factor and a high glass transition temperature, conditions for which the developed strain sensor result reliable in the normal operational temperature range of the aircraft. The partners showed that self-responsive panels can simultaneously act as sensor and structural element: this research is fully included in the current context addressed to realize more “intelligent” systems. Demand for highly compliant mechanical sensors for use in the fields as robotics and wearable electronics has been constantly rising in recent times. Carbon based materials, and especially, carbon nanotubes, have been widely studied as a candidate piezoresistive sensing medium in these devices due to their favorable structural morphology. The ever-growing field of robotics especially as used to complement human motions has given rise to the need for light weight and flexible sensors. Such devices must be highly compliant with excellent performance to achieve the desired end task and at the same time be comfortable for the end user. The present chapter deals with a study of these new generation materials, focusing on the applications for adaptive structures, moving up to a "self-sensing" system. Looking at the Figure 5.1 below, it is interesting the thin line that exists between modern industrial robotics and future aeronautical adaptive structures. A smart structure as a morphing wing needs an embedded and light-weight sensing system in order to measure the actual strain state as well as to “monitor” the structural conditions.

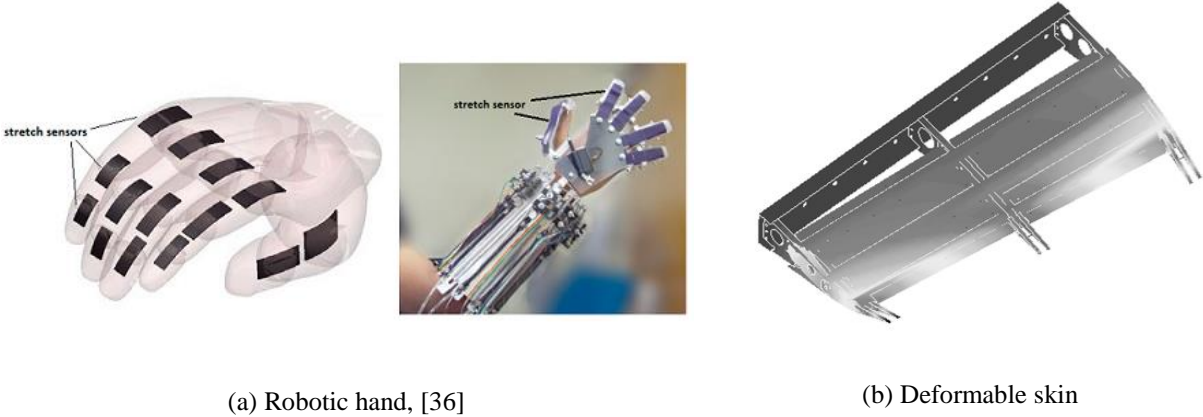


Figure 5.1. Sensor system for large scale integration: bio-robotics and analogy with morphing surfaces.

5.2 Materials and methods

Epoxy resins have been widely used for coatings, electronic materials, adhesives, and matrices for fiber-reinforced composites due to their outstanding mechanical properties ranging from extreme flexibility to high strength and hardness, high adhesion strength, good heat resistance, and high electrical resistance. The epoxy matrix was prepared by mixing the epoxy precursor TGMDA (epoxy equivalent weight 117–133 g/eq), with an epoxy reactive monomer 1,4-butanedioldiglycidylether (BDE) that acts as reactive diluent. These resins, both containing epoxy functionality, were obtained from Sigma-Aldrich. The epoxy mixture was made by mixing TGMDA with BDE monomer at a concentration ratio of 75:25 wt % epoxide to flexibilizer. In particular, the use of 25 wt % loading of reactive diluent has been chosen to reduce the viscosity of epoxy resin and hence to improve the nanofiller dispersion. GPOSS, functionalized with eight oxirane groups for each cage, were dispersed in the epoxy matrix and successively MWCNTs were dispersed in ethanol by ultrasonic waves for 30 min. The curing agent was 4,4'-diaminodiphenyl sulfone (DDS). This hardener agent was added at a stoichiometric concentration with respect to all the epoxy rings (TGMDA, BDE, and GPOSS). GPOSS was purchased from Hybrid Plastics and MWCNTs (3100 Grade) were obtained from Nanocyl S.A. Epoxy blend (TGMDA and BDE) and DDS were mixed at 120 °C until complete hardener solubilization and then the mixture was cooled to 90 °C. Carbon nanotubes and POSS compounds were added simultaneously and incorporated into the matrix at 90 °C by using an ultrasonication for 20 min. An ultrasonic device, Hielscher model UP200S (200 W, 24 kHz) (Hielscher Ultrasonics, Teltow, Germany), was used. The realization steps are well summarized in Figure 5.2(a). The samples were subjected to a two-step curing process as highlighted in Figure 5.2(b): an initial step at moderate temperature (125 °C for 1 h) and the second one at higher temperature (200 °C for 3 h), [37–38].

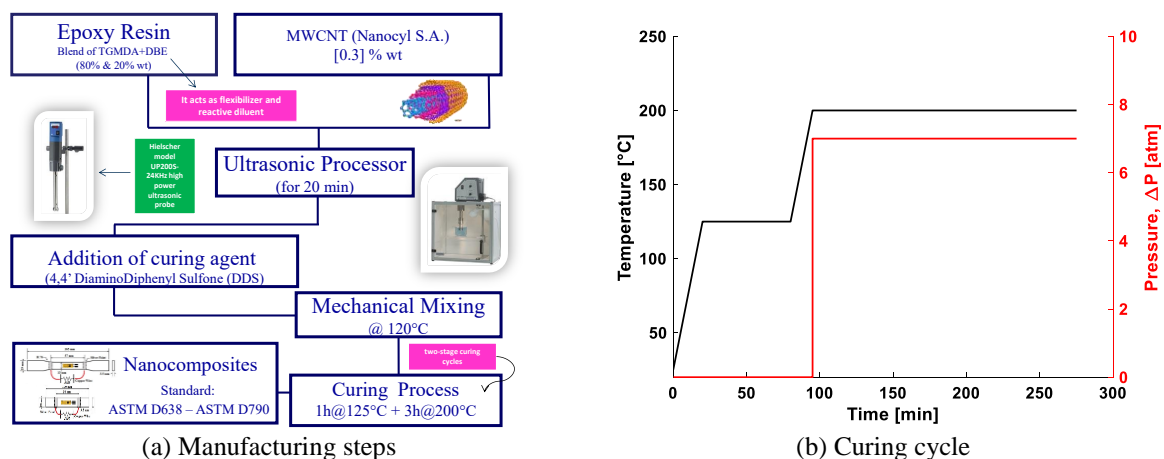


Figure 5.2. Self-sensing realization process.

5.3 Characterization of self-sensing resin

Electrical analysis

In order to investigate the mechanical and piezoresistive behavior of the nanocomposites, axial and flexural response strength measurements were performed in agreement with ASTM standards D638 and D790, respectively [39–40], using a Dual Column Tabletop Testing Systems (INSTRON, series 5967) set with a cross head speed of 1 mm/min for both loading and unloading. In particular, for the flexural tests a configuration of a three point-bending mode is adopted. The corresponding force was measured by the machine load cell and converted to axial stress (σ), whereas mechanical strain (ε) was calculated as the machine crosshead displacement normalized by the gage length of the test specimen. In order to exclude possible slipping during the displacement, the local deformation was detected by means of a conventional strain gage (RS 5 mm Wire Lead Strain, gauge factor 2.1) bonded to one side of the specimen and having a gauge resistance of 120 Ω constantly measured with a precision multimeter Agilent 34410A. Copper electrodes were fixed on the sample surface using silver paint (Silver Conductive Paint, resistivity of 0.001

Ω cm) thus ensuring a good ohmic contact between the parts for the measurement of the resistance, R , of the samples using the two-probe method with a multimeter Keithley 6517A configured in the double function of voltage generator and ammeter. This measurement method, although simple, has successfully been applied in literature for resistance measurements in presence of tensile test, [16], [41]. Contact resistance was neglected since the measured electrical resistance for all specimens was in the order of several $k\Omega$. An overview of the test setup and features of the investigated specimens are reported in Figure 5.3. In particular, the piezoresistivity behaviour observed in the strain sensors based on CNT/polymer nanocomposites is attributable to relevant changes in the electrical network, e.g. loss of contact among CNT, [42], variation in the tunnelling resistance due to the rearrangement of neighbouring CNT, [4], [43], and intrinsic piezoresistivity of fillers due to their deformation [7], [44]. As a consequence, there is in general, a new arrangement of the filler that results in small but experimentally detectable changes in the electrical properties. A preliminary electrical characterization focused on the DC volume conductivity of the composites is carried out without applying any strain (zero load) in order to identify a suitable filler concentration to be considered for testing under axial tension and flexural stress. Therefore, in Figure 5.4 the electrical conductivity (σ_m) as function of the amount of MWCNT (v) is reported. In particular, *Kirkpatrick's model* predicts the DC electrical conductivity based on the likelihood of contact between particles of filler within the composite. As expected by the percolation theory, the conductivity depends on the filler loading in agreement with a power law of the type:

$$\sigma_m = \sigma_0(v - v_c)^t \quad (5.1)$$

where v_c is the amount corresponding to percolation threshold, σ_0 is the filler conductivity and t an exponent depending on the system dimensionality, [45]. The *percolation threshold* is the minimum quantity of the filler required to form a continuous network of particles to transport electrical charge between the ends of the material being electrically polarized by a DC source. In particular, conductive paths are formed in the composite when the CNT amount (i.e. v) increases over a threshold value (EPT, i.e. v_c) thus leading the material to convert from an insulator to a conductor behaviour. It is worth to note that, as the concentration of the conductive fillers approaches the EPT, which is in the range [0.1-0.3 wt%], an abrupt increase in the electrical conductivity of the composites, compared with the few pS/m characterizing the pure resin, can be observed. A value of about 0.29 S/m is achieved at the highest filler loading (i.e. 1 wt%). It is worth noting that the values of EPT and electrical conductivity beyond the EPT greatly depend on the chemical nature of the hosting matrix, as well as on the manufacturing methods. As an instance, the same MWCNTs, embedded in resins characterized by very low values of viscosity, are able to give lowest EPT values, [46]. This different behaviour is most likely due to a strong influence of the viscosity on the nano-filler dispersion state. The value of the exponent t (i.e. 2.2) of the percolation law, obtained as the slope of the linear interpolation in the inset of Figure 5.4, is found to agree with universal values typically reported in literature. The sensitivity of the composites reinforced with carbon-base filler, as reported in different literature studies [3], [47-48], is low when the composite acts as an insulator (below the EPT) and decreases significantly as the weight loading of CNT increases in the high conductivity region. Therefore, the region around the EPT is the most suitable for sensor applications, [49-51]. In more detail, at low filler concentrations the composite conductivity can be considered very close to the pure polymer matrix. Once the percolation threshold has been reached (red line, Figure 5.4) the electrical conductivity undergoes a drastic increase due to the start of the formation and consolidation of an electrically conductive network through the sample. Lastly there is the saturated electrical conductivity obtained when a completely interconnected network is formed. Hence, in this chapter the mechanical and piezoresistive response of an epoxy resin suitable for the realization of structural aeronautic components and reinforced with 0.3 % wt of multi-walled carbon nanotubes was investigated when specimens are subjected to mechanical stress in axial and flexural mode. Such specific filler concentration has been chosen since it is a first concentration above the EPT and because in aeronautical composites a good electrical should be ensured.

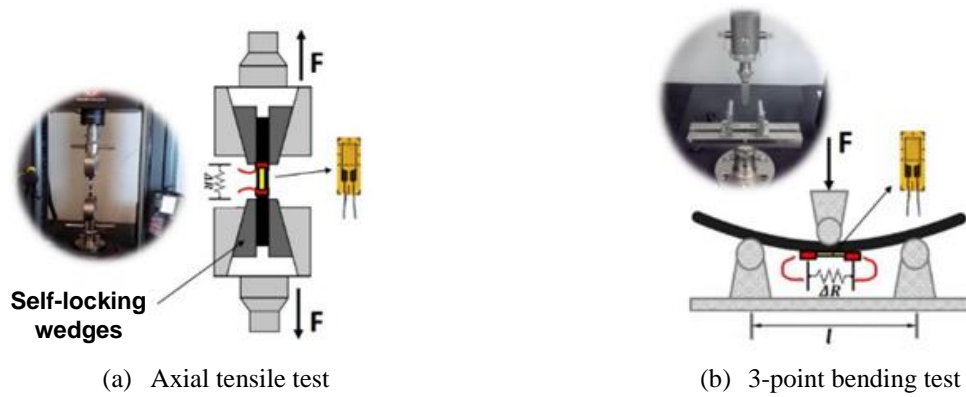


Figure 5.3. Experimental setup and for sensing characterization.

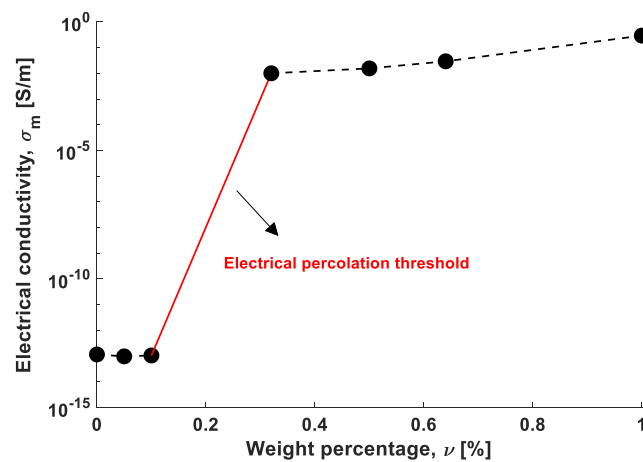


Figure 5.4. DC volume electrical conductivity.

Mechanical analysis

As previously mentioned, a strain gauge has been glued to the center of the sample in order to correlate the variation of CNTs electrical resistance to the structural deformation, Figure 5.5(a). The percentage of nanotubes (about 0.3 %) was chosen according to the percolation properties: it has been verified actually that the gauge factor tends to be maximized when the concentration of CNT is slightly higher than the percolation threshold, [38]. An optical extensimeter has been applied by means of a fibre Bragg grating (FBG), Figure 5.5(b). The most common way of printing gratings inside a glass core fibre is realizing a periodic modulation of the effective refractive index using excimer lasers or UV sources and a suitable method for generating the spatial pattern, such as phase mask. When a light source is travelling inside a fibre core, the signal is reflected back by the grating at the Bragg wavelength λ_B . Light waves are scattered at each plane and interfere constructively. Bragg's law describes the condition for constructive interference from several planes of the grating separated by a distance d , and, as a result, this narrow component is reflected back and missed in the transmission spectrum. When an FBG is bonded on a structural surface and local deformation is present, the grating's period length varies and the reflected wavelength changes (upward or downward shift) accordingly, allowing detection of the local strain. Selected optic fibre is characterised by an outer diameter of 0.250 mm and an acrylate coating. FBG is 10 mm long and its central wavelength is 1570 nm. Fibre is bonded on the outer surface of the carbon nanotube-based composite coupon. The typical period of a Bragg grating is about 0.5 μm . For silica core fibres ($\rho_e = 0.22$) the typical strain sensitivity is approximately 1.2 pm/ $\mu\epsilon$. For low strain (< 0.2%), room-temperature (23 °C) applications of cyanoacrylate adhesive (M-bond 200) works well. Surface impurities are completely removed and surface is roughened with fine abrasive paper before adhesive bonding. The route of the sensor fibre is first measured and clearly

marked out, keeping in mind that the fibre sensor will only measure strain along the axis of the fiber. Once the sensor fibre has been tacked in place before adhesive bonding, a soft tip applicator or a rubber pad is used to spread the epoxy along the fiber. Thick adhesive layer would result in transverse strains with the consequence of fibre birefringence and variable coupling coefficients. Thick bond lines may furthermore result in strain transfer loss. The aim of the experimental test campaign is to monitor the strain of a carbon nanotube-based composite sample and correlate to the current. An optical interrogator SM130 is used to detect strain values with a sampling rate of 1 Hz. A laptop running Enlight software is provided with a graphical interface showing the FBG pick tracking. Data output file are logged in *.txt* format and then processed in Matlab® environment. The main tools used for the testing activity are represented in Figure 5.6. The sensitivity of a piezoresistive sensor, that is desirable to be as high as possible for practical applications, can be quantified in terms of gauge factor, a dimensionless parameter defined as the relative change in electrical resistance due to an applied strain (5.2):

$$G.F. = \frac{\Delta R}{\epsilon R_0} \tag{5.2}$$

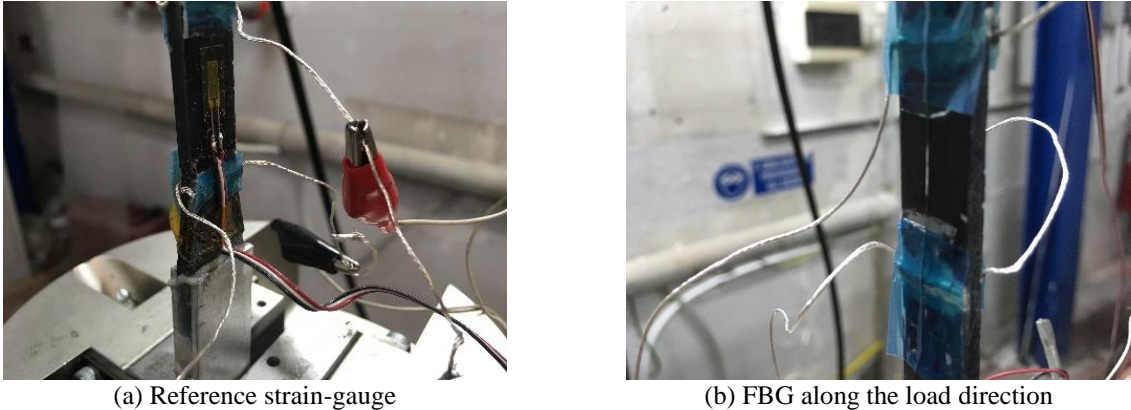


Figure 5.5. Static test: deformation transducers set-up.

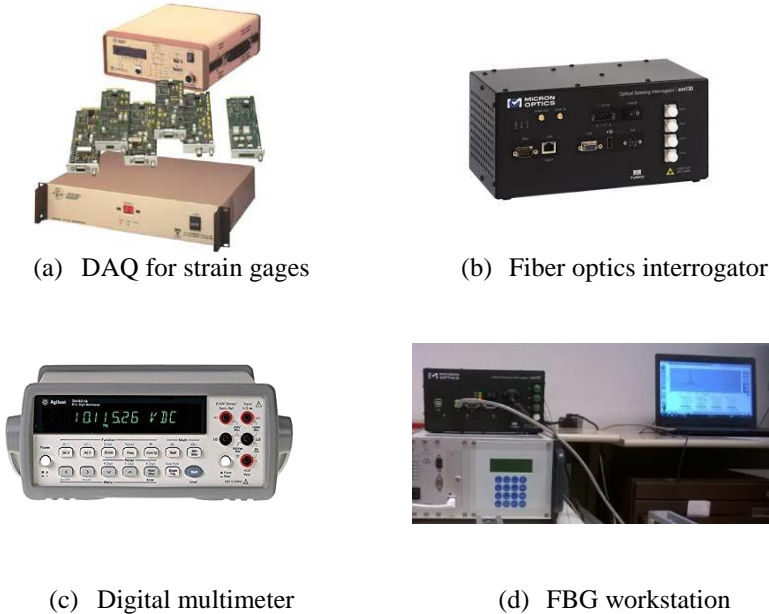


Figure 5.6. Test instrumentation.

Tensile test

In Figure 5.7 the mechanical and piezoresistive performances of the CNT-based polymer when loaded in axial tension up to failure, are represented. Especially, the outcomes report the normalized change of electrical resistance $\Delta R/R_0$ on the right vertical axis, in which R_0 is the steady-state electrical resistance of the material without applying any external load while the differential $\Delta R = R - R_0$ is the ohmic instantaneous change, as function of the axial strain. The mechanical load (i.e. σ) is then reported on the left vertical axis with respect to the strain gauge and FBG measurements. An interesting comparison among the three trends can be outlined. Firstly, the experiment allowed for well to identify the different operating regions, essential to get the structural behavior of the polymer: the typical elastic region detected for lower strain levels (strain up to 2% with respect the rest position) which is then followed by the nonlinear plastic zone for higher loadings. The test stopped once the specimen collapse sample was achieved. The sudden mechanical break obviously affects the sensor response. Actually, the plasticity of the resin led to a micro-cracking that disturbs the electrical measurements (around at the 3.5% of strain level). Anyway, the sensing capability of the polymer has been well characterized. In the linear mechanical region, a high correlation signal with piezoresistive curve can be appreciated. The intrinsic sensing properties of the resin are largely consistent with the measurements provided by commercial sensors (Strain Gauge, FBG). Then, the $\Delta R/R_0$ curve becomes nonlinear with an evident abrupt change most likely due to the occurrence of the first nano-crackings within the structure. The sensitivity of a piezoresistive sensor has been quantified in terms of gauge factor: the value obtained of 0.43 is derived as the slope of the interpolating line of resistance ratio curve of experimental data that lie in the elastic region. The increase of the overall resistance of the sample with increasing tensile stress agrees with the assumption that in a conductor-filled polymer the main electrical conduction mechanism occurs via "tunneling effect" which requires that the filler particles must be sufficiently close (at the so-called "tunneling distance") to each other to allow the electron flow. As a consequence of the imposed tensile strain, it is reasonable that the tunneling resistance could vary between neighboring CNT due to the enlargement of inter-tube distance and/or a decreasing of the electrical contact areas. Both phenomena lead to an increase of the resistance exhibited by the sample. In order to investigate the reversibility and stability of sensor properties of the nanocomposites, specimens were subjected to tensile loading cycles based on increases/decreases of some selected level strains, [16], [47], [52].

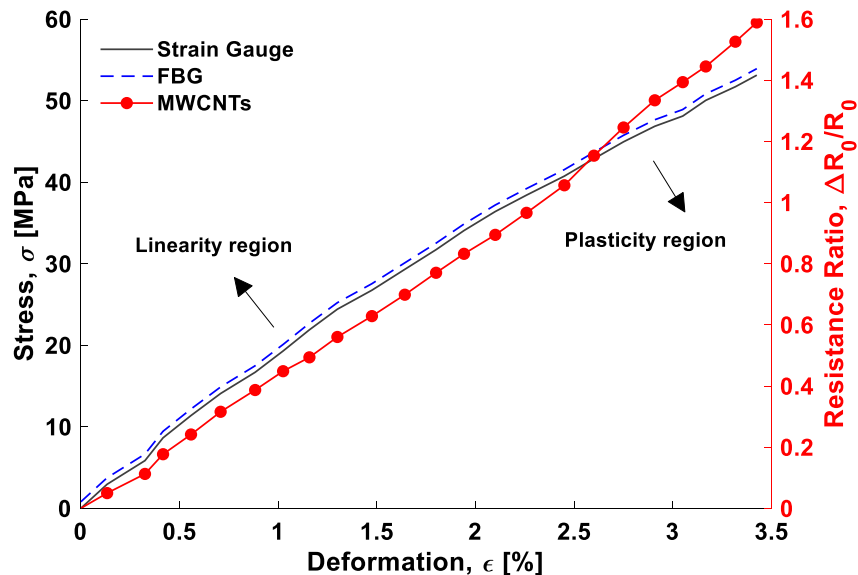


Figure 5.7. Tensile test, sensing correlation ($G.F. = 0.43$).

Flexional test

The self-sensing capability of filled sample was related to bending deformations too. Other literature studies report experiments performed in the 4-points-bending mode on thermoplastic polymers and rubbers, [50-53]. Here, the flexural stress-strain curves are obtained from three-point bend test of the samples. The flexional test outcomes are shown in Figure 5.8. In order to prevent possible discrepancies during the displacement, the flexural strain was detected by means of a conventional strain gauge. In this case, it was not possible to install another strain sensor on the opposite side, being the point of application of the load. In the same figure the experimentally detected values are also compared to those evaluated from the following relation:

$$\varepsilon_{flexural} = \frac{6wh}{L^2} \quad (5.3)$$

where w is the maximum deflection of the center of the sample, h is the sample thickness and L is the support span. Differently from the piezoresistive behavior observed in tensile test, the normalized change of electrical resistance $\Delta R/R_0$ vs. strain measured in such mode is nonlinear in the whole strain range and follows an exponential law. The different behaviors observed for the two types (tensile and flexural) of imposed stresses may be explained by considering a different micro-rearrangement of the conductive network inside the insulating polymer. In presence of tensile stress, i.e. the application of a traction force normal to the surface, the material reacts with a simple stretching in the direction of the force. This stretching is uniform in the entire cross-section of the load application. As a consequence, the percolating network moves rigidly with the force and the electrical response appear linear. In the case of flexural loading M , the specimen deformation follows the curvature distribution according to a radial law [54], Figure 5.9(a). Since the bottom surface is under tension, while the top one is under compression, as a result, the electrical sensitivity of the material is influenced by a combination of these two coexisting effects. Therefore, the nano-networks in the compressed part approach each other as a result of the action of compressive stresses. The specular tensile load instead implies a greater elongation which increases the distance between the carbon nanotubes, thus reducing the tunneling sensitivity, Figure 5.9(b). As a result, the tunneling resistance between nanotubes, particularly sensitive to distance variations, affects more significantly the electrical response of the material thus originating the exponential dependence of the resistance ration as function of the strain state.

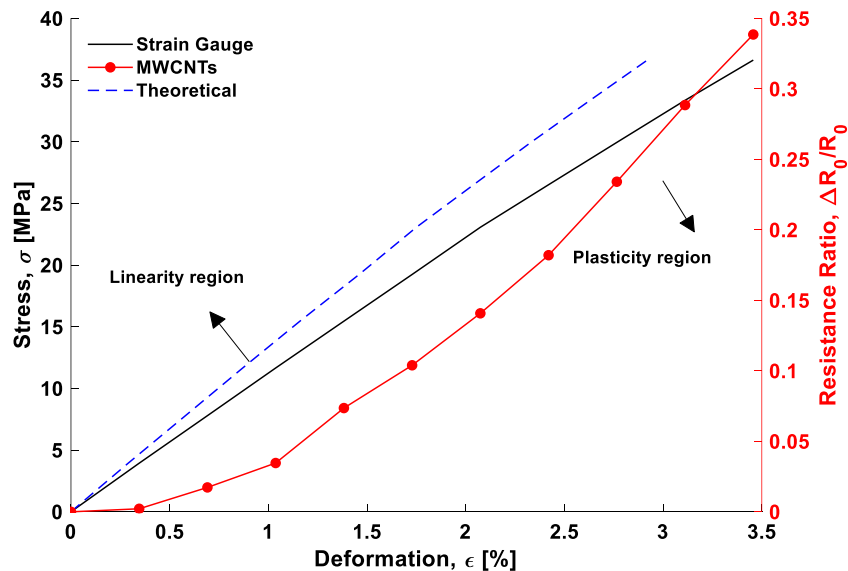


Figure 5.8. 3-point bending test, sensing correlation.

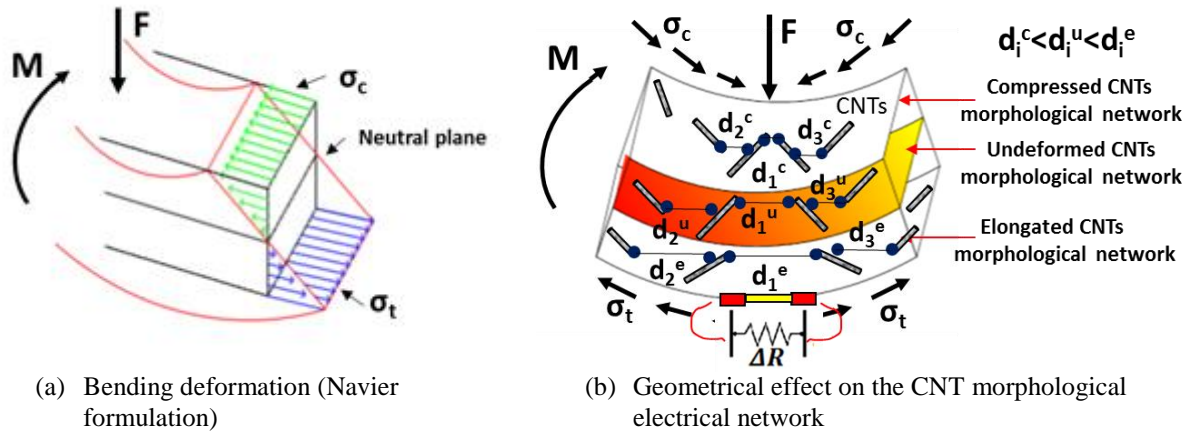


Figure 5.9. Piezoresistive correlation with flexional mechanical stress.

5.4 Integrated self-sensing coating

An uniform conductive coating made of epoxy based MWCNTs could be a valid solution to implement for an active compliant skin on the tab segment of morphing flap, Figure 5.10. The research activity allowed for evaluating nano-technologies that can be integrated into structures aiming to create an electrical structural network whilst reducing cabling weight and improving survivability of composite structures. In this perspective, the filling of carbon nanotubes in the form of coating on the rigid laminate segments, has been investigated as a valid solution to embody a shape sensing system inside the smart structure. This “distributed sensing” technology allows for implementing an extensive embedded sensor network overcoming then the curvature and endurance limits often associated to the adoption of fiber optics or standard strain gauges. A complication of typical sensing system comes from the fact that the structure is morphing, then deformable and experiencing large displacements. Morphing surfaces necessitate the implementation of an intelligent sensing network to ensure not only optimal control of the aerodynamic surface but also failure tolerance and robustness. The aim of the research is addressed in developing a shape sensing system through toughening additives such as nano-materials and various types of polymers, incorporated onto the skeleton itself. The appropriate choice both of the components of the epoxy resin and the carbon nanotube concentration, allows to prepare a conductive coating with high sensitivity factor and a high glass transition temperature, conditions for which the developed strain sensor result reliable in the normal operational temperature range of the aircraft. A smart coating exhibiting self-diagnostic capability has been therefore designed to meet these ambitious requirements. The coating made of epoxy-based carbon nanotubes has been applied on industrial Carbon Fiber Reinforced Plastics (CFRPs) representative of a portion skin of the morphing flap conceived within Clean Sky 2- Airgreen 2. The correlations between mechanical strain and electrical properties of coated CFRPs highlights the feasibility in manufacturing CFRPs having integrated high sensitivity in providing an effective real-time strain monitoring. The reliability of the developed CFRPs, in the normal operational temperature range of aircrafts, opens new perspectives in the field of self-responsive structures in aeronautics.

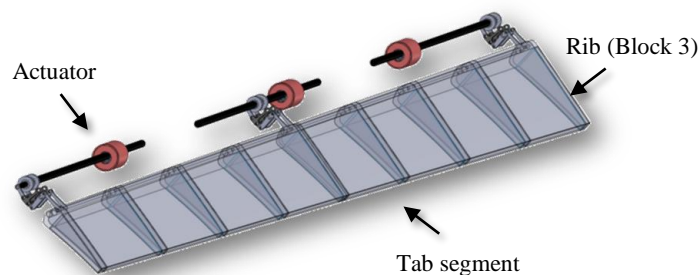


Figure 5.10. Isoview of the tab segment (Clean Sky): detail of the skin.

Sample manufacturing

The specimens analyzed in this work have been obtained following a well-defined procedure described in some papers [33], [38], [55]. Fiber-reinforced composite parts have been cut into flat coupons 20 cm×35 cm with a nominal thickness of 1.15 mm. A diamond tip water-cooled saw blade has been used. The surface of Carbon Fiber Reinforced Plastics (CFRP) parts has been treated by sandblasting in order to increase the roughness of the surface for a greater adhesion of the conductive coating to the laminate. Subsequently they have been cleaned and dried prior to coat them. In order to obtain a uniform conductive resin coating on the panels produced, a K303 multicoater of the RK Printcoat Instrument has been used, i.e. a surface coating applicator. The panel has been deposited on the multicoater and clamped by means of a bench vise, Figure 5.11(a), in order to avoid movements during the covering. After the clamping, the appropriate head has been applied. Subsequently the mixture loaded with the carbon nanotubes has been deposited along the head and finally the movement of the head at programmed speed (1 mm/ min) has been activated (Figure 5.11(b) and (c)). Finally, the laminate, with the conductive coating, has undergone a curing cycle of 1 h at 150 °C and 3 h at 220 °C, Figure 5.11(d). The carried-out process step allowed to have a coating thickness of about 150 μm. Different from conventional strain monitoring systems, these multifunctional composites can be applied with successful on various surface giving rise to an innovative solution for monitoring structural deformation and damage directly measuring electrical resistance change, due to the piezoresistive properties of the developed coating, without require further additional sensors.

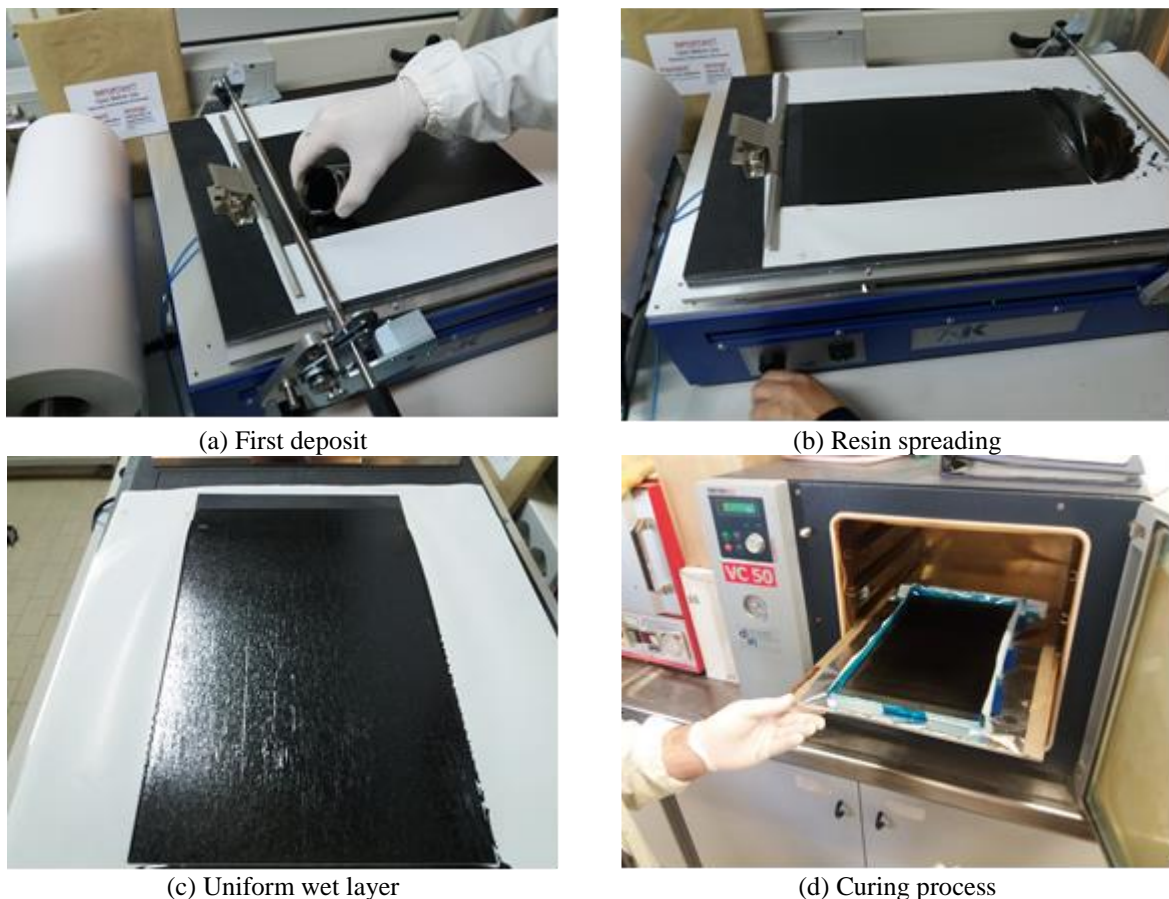
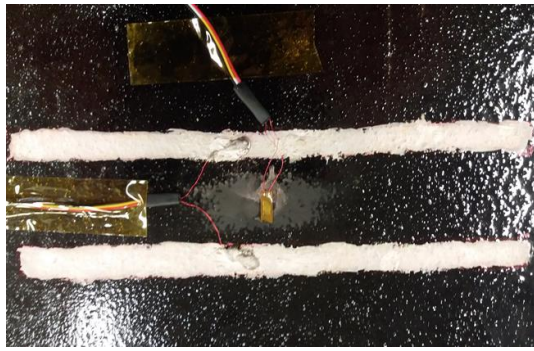


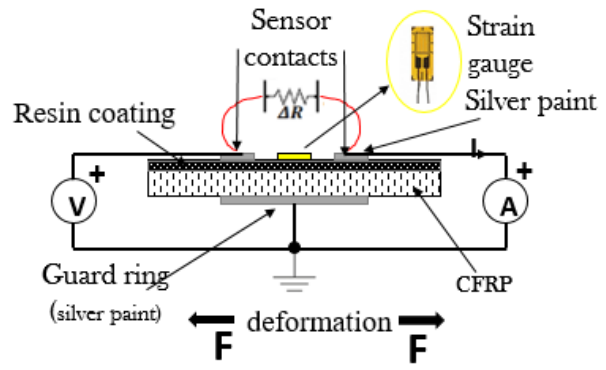
Figure 5.11. Manufacturing process of MWCNTs-based film for a substrate CFRC panel.

Coating characterization

For this purpose, suitable electrical contacts have been deposited on the panel, by using silver paint (RS 186-3600 with volume resistivity $0.001 \Omega \cdot \text{cm}$, when fully hardened). As a matter of fact, to prevent that bulk currents (i.e. those passing through the material given the high electrical conductivity of the CFRP) provide a contribution to the measured surface current, the electrical measurement configuration has been opportunely studied. In particular, a guard ring “collects” such currents which can be drained downstream of the measuring instrument, toward the mass of the system. The experimental results confirm the correctness of this ploy since an electrical resistance of 30Ω and of the order of $\text{k}\Omega$ is measured adopting a configuration equipped with and without the guard ring, respectively. In fact, the first value is not plausible being too much low for proposed conductive coating, whereas the second one is comparable to that observed only on the resin loaded with 0.1% by weight of carbon nanotubes. The electrode-sample system is shown schematically in Figure 5.12. The two-probe method, performed with a Multimeter Keithley 6517A configured as voltage generator and HP3458A Digital Multimeter employed as ammeter, has successfully been applied in literature, although simple, for resistance measurements in presence of tensile test [16],[41]. Moreover, in order to exclude possible slipping during the displacement, the local deformation was detected by means of a conventional strain gauge (RS 5mm Wire Lead Strain, gauge factor 2.1 and gauge resistance of 120Ω) bonded to one side of the specimen, whose electrical resistance change has been constantly measured with a precision multimeter Agilent 34410A. Tensile tests have been carried out by using an MTS 370.50 Universal Testing System at 1 mm/min crosshead speed and equipped with 500 kN load cell and hydraulic grips. In the all analyzed range of strains, a linear behaviour is observed with normalized change of electrical resistance, Figure 5.13. The increase of the resistance of the applied coating with increasing tensile strain agrees with the assumption that in a conductor-filled polymer the main electrical conduction mechanism occurs via “tunneling effect” which requires that the filler particles must be sufficiently close (at the so-called “tunneling distance”) to each other to allow the electron flow, [56]. Consequently, the tunneling resistance changes between neighbouring CNT due to the enlargement of inter-tube distance and/or a decreasing of the electrical contact areas. Both phenomena lead to an increase of the resistance exhibited by the conductive material. The interpolating line of resistance ratio curve of experimental data allows to evaluate the gage factor of the conductive coating, that in this case is about 4.7. The sensitivity factor or otherwise called gauge factor is a very important feature of the strain sensor for which it is necessary to give some clarifications. Processing conditions and material properties play a notable role in determining the sensor sensitivity. In particular, to improve the sensitivity of the sensor system, the following conditions are needed: 1) lower content of CNTs close to the percolation threshold, 2) lower curing temperature, 3) higher stirring or mixing rate, 4) higher height of barrier of matrix and 5) higher electrical conductivity of filler. In other words, in order to obtain a high value of $G.F.$ it is necessary to maximize the tunneling resistance (see condition 1,3,5) and to use soft materials such as thermoplastic or thermosetting polymers with a low glass transition temperature (see condition 2,4) [14]. A linear pattern of the resistance ratio was also observed when the specimen was bending loaded in a jammed-free configuration (cantilever beam scheme). In this case, the voltamperometric measurement was carried out along the whole deflected length of the panel, considering multiple pairs of silver contacts. In such a way, it was possible to reconstruct an interpolated scheme (Figure 5.14(a)) of the superficial resistances of the coating. The same approach was used by shifting the end load (up to 2 N) from the centreline along the x direction of the panel, inducing so a torsional load, Figure 5.14(b). The results bring out an increase in resistance where the tension states are much higher (close to the constraint line). In previous works, high values of sensitivity factor were obtained, using thermoplastic matrices such as polysulfone ($G.F.=6.2$) [41] or Poly(methyl-methacrylate) ($G.F. \leq 6$) not applicable in the field of aeronautical materials where most of the materials are based on epoxy resins. In the present case, a high $G.F.$ has been achieved looking at epoxy resins normally used in the field of structural materials for aeronautical applications. A very relevant result of the present activity is therefore the applicability of the thermosetting filled formulation (with suitable CNT concentration) as coating to confer self-diagnostic function to structural aeronautical panels. From prelamina tests carried out on structural panels, this strategy seems to be easy to implement and can constitute the first step of industrialization processes. Studies are ongoing about the electro-mechanical behaviour with dynamic strain cycles applying the developed functional coating on structural panels reinforced with different fibers (Carbon Fiber and Glass Fiber).

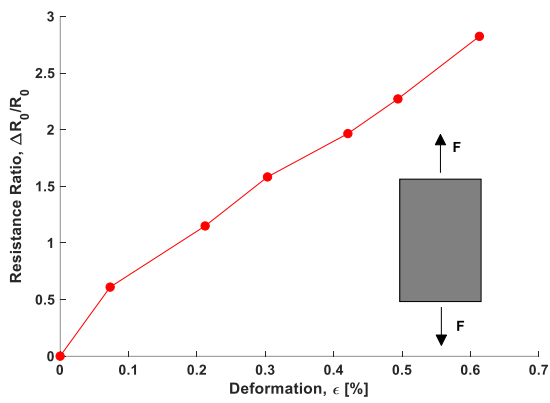


(a) Electrodes and reference strain gauge

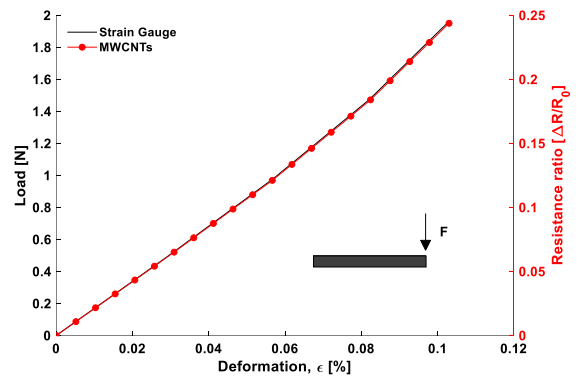


(b) Electrical connection scheme

Figure 5.12. Specimen instrumenting phase.

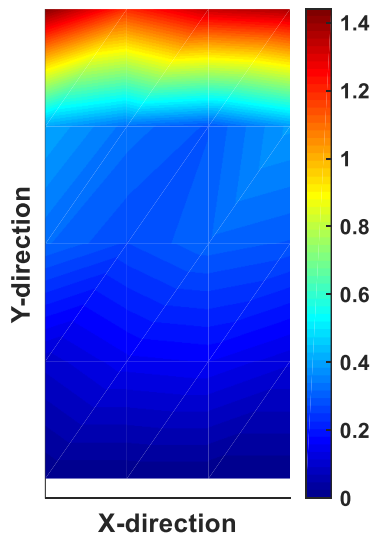


(a) Tensile test

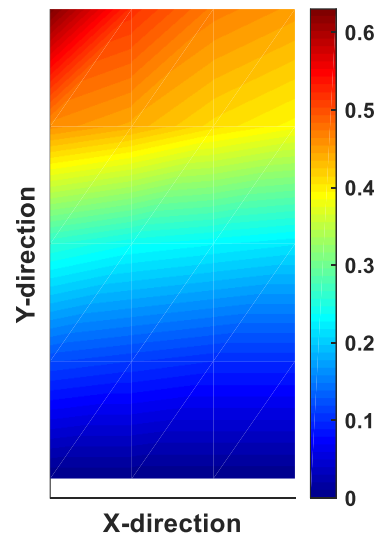


(b) Bending test

Figure 5.13. Mechanical test results.



(a) Bending load



(b) Torsional load

Figure 5.14. Mechanical test results.

5.5 Conclusions and outlooks

Future aircraft will possess adaptive capabilities, from supervised morphing to active deployable subcomponents, and self-sensing properties for auto-inspection. Deployable and adaptive structures are also attractive for space missions, envisaging a better matching of the different mission phases and an easier storage and release of some essential components, like antennas and solar cells. All these functionalities are promising but challenging and a crucial role is played by integrated sensing networks (for real-time monitoring and control aims), that should be widely distributed all over the structure, implying a huge number of terminals and an impressive quantity of cables. Structural systems are in fact characterized by infinite degrees of freedom, in principle, excited over a wide frequency range. Furthermore, morphing and deployability also implies the occurrence of very large deformations. Specific materials, able to recover large deformations, like foams, silicones and polymeric shape memory alloys, may also be monitored; the challenge of following and withstanding the large deformations of the structure is accompanied by the adhesion to the external surface and by extreme environmental conditions in space. Integration, cable routing, information management, and monitoring wide strain and temperature ranges, are critical tasks in this framework. Morphing or active deployable functionalities seem highly dependent on the availability of an extended sensor network on the basis of consolidated knowledge from several industrial research projects. The piezoresistive behaviour of a structural resin, particularly indicated for aircraft applications and reinforced with a specific amount of MWCNT, was investigated with electrical measurements when the specimens are subjected to a low number of cycles and different levels of strain loaded in both axial tension and flexural mode. The piezoresistive properties can be mainly attributed to the re-arrangement of conductive percolating network formed by MWCNT induced by the deformation of the material due to the applied stresses. The nanocomposites showed high sensibility, reliability and reversible response. An uniform conductive coating made of epoxy based MWCNTs has been stratified on aeronautical CFRPs. Measurements of electrical resistance as a function of applied strain have been performed on panels. The Gage Factor of the coated CFRPs has been found of 4.7 which is the higher value achieved until now for thermosetting resins. This value is not a trivial result, considering the chemical nature of the functional coating here described, which is based on thermosetting matrix characterized by mechanical performance able to meet the industrial requirements of primary structures.

Acknowledgments

The author thanks Prof. Liberata Guadagno and Prof. Michele Meo for having given him the opportunity to collaborate in stimulating and highly research contexts. A sincere acknowledge is addressed to the research team that includes: Dr. Massimo Viscardi, Dr. Giuseppina Barra and Dr. Luigi Vertuccio for the remarkable support during all the research and experimental activities. The research leading to these results has received funding from the European Union Horizon 2020 Programme under Grant Agreement n° 760940.

References

- [1] Kang, I., Schulz, M.J., Kim, J.H., Shanov, V. and Shi D.: A carbon nanotube strain sensor for structural health monitoring, *Smart Materials and Structures*, 15, 737–748 (2006).
- [2] Topolov, V.Yu, Bowen, C.R. and Bisegna, P.: New aspect-ratio effect in three-component composites for piezoelectric sensor, hydrophone and energy-harvesting applications, *Sensor Actuat A-Phys*, 229, 94–103 (2015).
- [3] Kang, I., Heung, Y.Y., Kim, J.H., Lee, J.W., Gollapudi, R., Subramaniam S. *et al.*: Introduction to carbon nanotube and nanofiber smart materials, *Composites Part B-Eng*, 37, 382–394 (2006).
- [4] De Vivo, B., Lamberti, P., Spinelli, G., Tucci, V., Vertuccio, L. and Vittoria, V.: Simulation and experimental characterization of polymer/carbon nanotubes composites for strain sensor applications, *J Appl Phys*, 116:054307-14 (2014).
- [5] Dargahi, J.: A piezoelectric tactile sensor with three sensing elements for robotic, endoscopic and prosthetic applications, *Sensor Actuat A-Phys*, 80, 23–30 (2000).
- [6] Tomblor, T.W., Zhou, C., Alexseyev, L., Kong, J., Dai, H., Liu, L. *et al.*: Reversible electromechanical characteristics of carbon nanotubes under local-probe manipulation, *Nature*, 405, 769–772 (2000).
- [7] Yang, L. and Han, J.: Electronic Structure of Deformed Carbon Nanotubes, *Phys Rev Lett*, 85, 154–157 (2000).

- [8] Song, X., Liu, S., Gan, Z., Lv, Q., Cao, H. and Yan, H.: Controllable fabrication of carbon nanotube-polymer hybrid thin film for strain sensing, *Microelectron Eng*, 86, 2330–2333 (2009).
- [9] Häntzschke, E., Matthes, A., Nocke, A. and Cherif, Ch.: Characteristics of carbon fiber based strain sensors for structural-health monitoring of textile-reinforced thermoplastic composites depending on the textile technological integration process, *Sensor Actuat A-Phys* 203, 189–203 (2013).
- [10] Williams, J.C. and Starke, A.E. Jr.: Progress in structural materials for aerospace systems, *Acta Mater*, 51, 5775–5799 (2003).
- [11] Kawakami, H. and Feraboli, P.: Lightning strike damage resistance and tolerance of scarf-repaired mesh-protected carbon fiber composites, *Composites Part A-Appl S*, 42, 1247–1262 (2011).
- [12] Larsson, A.: The interaction between a lightning flash and an aircraft in flight, *C R Physique*, 3, 1423–1444 (2002).
- [13] Park, S., Shin, H.H. and Yun, C.B.: Wireless impedance sensor nodes for functions of structural damage identification and sensor self-diagnosis, *Smart Materials and Structures*, 18, 055001-(11pp) (2009).
- [14] Ning, Hu., Karube, Y., Arai, M., Watanabe, T., Yan, C., Li, Y., *et al.*: Investigation on sensitivity of a polymer/carbon nanotube composite strain sensor, *Carbon*, 48, 680–687 (2010).
- [15] Serra, N., Maeder, T. and Ryser, P.: Piezoresistive effect in epoxy-graphite composites, *Sensor Actuat A-Phys*, 186, 198–202 (2012).
- [16] Ku-Herrera, J.J. and Aviles, F.: Cyclic tension and compression piezoresistivity of carbon nanotube/vinyl ester composites in the elastic and plastic regimes, *Carbon*, 50, 2592–2598 (2012).
- [17] Amjadi, M., Kyung, K.U., Park, I. and Sitti, M.: Stretchable, skin-mountable, and wearable strain sensors and their potential applications: A review, *Adv Funct Mater*, 26, 1678–1698 (2016)
- [18] Gaiser, P., Binz, J., Gompf, B., Berrier, A. and Dressel, M.: Tuning the dielectric properties of metallic-nanoparticle/elastomer composites by strain, *Nanoscale*, 7, 4566–4571 (2015).
- [19] Loh, K.J., Kim, J. and Lynch, J.P.: Self-sensing and power harvesting carbon nanotube-composites based on piezoelectric polymers, 4th International Conference on Bridge Maintenance, Safety and Management. Seoul (Korea): CRC Press; Taylor & Francis Group, 3329–3336 (2008).
- [20] Mei, H., Zhang, C., Wang, R., Feng, J. and Zhang, T.: Impedance characteristics of surface pressure-sensitive carbon black/silicone rubber composites, *Sensor Actuat A-Phys*, 233, 118–124 (2015).
- [21] Barra, G., De Nicola, F., De Vivo, B., Egiziano, L., Guadagno, L., Lamberti, P., Raimondo, M., Spinelli, G., Tucci, V., Vertuccio, L., Vietri, U. and Volponi, R.: Enhanced electrical properties of carbon fiber reinforced composites obtained by an effective infusion process, *IEEE 9th Nanotechnology Materials and Devices Conference, NMDC*, (2014).
- [22] Viscardi, M., Arena, M., Barra, G. and Guadagno, L.: Structural performance analysis of smart carbon fiber samples supported by experimental investigation, *International Journal of Mechanics*, 10, 376–382 (2016).
- [23] Viscardi, M., Arena, M., Barra, G. and Guadagno, L.: Smart carbon-epoxy laminate with high dissipation properties for vibro-acoustic optimization in the turboprop aircraft, *International Journal of Mechanics*, 11, 51–57 (2017).
- [24] Barra, G., Guadagno, L., Simonet, B. and Santos, B.: The influence of different dispersion methods on the size of the aggregate of CNTs in epoxy resin for the manufacturing of carbon fiber reinforced composites, *AIP Conference Proceedings*, (2016).
- [25] Guadagno, L., Raimondo, M., Vietri, U., Barra, G., Vertuccio, L., Volponi, R., Cosentino, G., De Nicola, F., Grilli, A. and Spena, P.: Development of multifunctional carbon fiber reinforced composites (CFRCs) - Manufacturing process, *AIP Conference Proceedings*, (2014).
- [26] Thill, C., Etches, J., Bond, I., Potter, K. and Weaver, P.: Morphing skins, *The Aeronautical Journal*, 112(1129), 117–139 (2008).
- [27] Wang, Y., Wang, A.X., Wang, Y., Chyu, M.K. and Wang, Q.-M.: Fabrication and characterization of carbon nanotube-polyimide composite based high temperature flexible thin film piezoresistive strain sensor, *Sensors and Actuators A: Physical*, 199, 265–271 (2013).
- [28] Weisshaar, T.A.: Morphing aircraft technology – new shapes for aircraft design, In multifunctional structures/integration of sensors and antennas, Meeting Proceedings RTO-MP-AVT-141, Overview 1, Neuilly-sur- Seine France, 2006 RTO, pp. O1-1–O1-20, Available from: <http://www.rto.nato.int/abstracts.asp>.
- [29] Kong, J.H., Jang, N.S., Kim, S.H. and Kim, J.M.: Simple and rapid micropatterning of conductive carbon composites and its application to elastic strain sensors, *Carbon*, 77, 199–207 (2014).
- [30] Viscardi, M., Arena, M., Guadagno, L., Vertuccio, L. and Barra, G.: Multi-functional nanotechnology integration for aeronautical structures performance enhancement, *International Journal of Structural Integrity* (2017), <https://doi.org/10.1108/IJSI-11-2017-0060>.
- [31] Arena, M., Viscardi, M., Guadagno, L., Vertuccio, L. and Barra, G.: Multidisciplinary challenge in the design of a MWCNTs-based polymer smart structure, 8th EASN-CEAS International Workshop on Manufacturing for Growth & Innovation, 4-7 September, Glasgow, UK (2018).

- [32] Viscardi, M., Arena, M., Barra, G., Vertuccio, L., Ciminello, M. and Guadagno, L.: Piezoresistive strain sensing of carbon nanotubes-based composite skin for aeronautical morphing structures, Proc. SPIE 10599, Nondestructive Characterization and Monitoring of Advanced Materials, Aerospace, Civil Infrastructure, and Transportation XII, 105991C (2018).
- [33] Arena, M., Vertuccio, L., Barra, G., Viscardi, M. and Guadagno, L.: Dynamic performance of self-sensing epoxy resin for aerospace structures, AIP Conference Proceedings 1981, 020066 (2018), <https://doi.org/10.1063/1.5045928>.
- [34] Barra, G., Vertuccio, L., Naddeo, C., Arena, M., Viscardi, M. and Guadagno, L.: Thermal degradation and fire properties of epoxy modified resins, AIP Conference Proceedings 1981, 020149 (2018), <https://doi.org/10.1063/1.5046011>.
- [35] Arena, M., Vertuccio, L., Barra, G., Viscardi, M. and Guadagno, L.: Nano-filler technologies characterization for smart aeronautical applications, Italian Association of Aeronautics and Astronautics (AIDAA) XXIV International Conference, 18-22 September (2017), Palermo – Enna, Italy.
- [36] Devaraj, H., Giffney, T., Petit, A., Assadian, M. and Aw, K.: The Development of Highly Flexible Stretch Sensors for a Robotic Hand. Robotics, 7, (2018).
- [37] Barra, G., Vertuccio, L., Vietri, U., Naddeo, C., Hadavinia, H. and Guadagno, L.: Toughening of epoxy adhesives by combined interaction of carbon nanotubes and Silsesquioxanes, Materials, 10(10), 1131 (2017).
- [38] Vertuccio, L., Guadagno, L., Spinelli, G., Lamberti, P., Tucci, V. and Russo, S.: Piezoresistive properties of resin reinforced with carbon nanotubes for health-monitoring of aircraft primary structures, Composites Part B: Engineering, 107, 192–202 (2016).
- [39] ASTM D638: Standard Test Method for Tensile Properties of Plastics, West Conshohocken, PA: ASTM International, (2010).
- [40] ASTM D790: Standard Test Methods for Flexural Properties of Unreinforced and Reinforced Plastics and Electrical Insulating, (2010).
- [41] Oliva-Avilés, A.I., Avilés, F. and Sosa, V.: Electrical and piezoresistive properties of multi-walled carbon nanotube/polymer composite films aligned by an electric field, Carbon, 49, 2989–2997 (2011).
- [42] Park, M., Kim H. and Youngblood, J.P.: Strain-dependent electrical resistance of multi-walled carbon nanotube/polymer composite films, Nanotechnology, 19:055705, (2008).
- [43] Wichmann, M.H.G., Buschhorn S.T., Gehrman J. and Schulte, K.: Piezoresistive response of epoxy composites with carbon nanoparticles under tensile load, Phys Rev B, 80, 245437-1 245437–8 (2009).
- [44] Yang, L., Anantram, M.P., Han, J. and Lu, J.P.: Band-gap change of carbon nanotubes: Effect of small uniaxial and torsional strain, Phys Rev B, 60, 13874–13878 (1999).
- [45] Nan, C.W., Shen, Y., Ma, J.: Physical Properties of Composites Near Percolation, Annu Rev Mater Sci., 40, 131–151 (2010)
- [46] Pham, G.T., Park, Y.B., Liang, Z., Zhang, C. and Wang, B.: Processing and modeling of conductive thermoplastic/carbon nanotube films for strain sensing, Composites Part B-Eng, 39, 209–216 (2008).
- [47] Vertuccio, L., Vittoria, V., Guadagno, L., De Santis, F.: Strain and damage monitoring in carbon-nanotube-based composite under cyclic strain, Composites Part A Appl Sci Manuf, 71, 9–16 (2015).
- [48] Ferreira, A., Rocha, J.G., Ansón-Casaos, A., Martínez, M.T., Vaz, F. and Lanceros-Mendez, S.: Electromechanical performance of poly(vinylidene fluoride)/carbon nanotube composites for strain sensor applications. Sensor Actuat A-Phys, 178, 10–16 (2012).
- [49] Simoes, R., Silva, J., Vaia, R., Sencadas, V., Costa, P., Gomes, J. *et al.*: Low percolation transitions in carbon nanotube networks dispersed in a polymer matrix: dielectric properties, simulations and experiments. Nanotechnology, 20:035703, (2009).
- [50] Paleo-Vieto, A.J., van Hattum, F.W.J., Pereira, J., Rocha, J.G., Silva, J., Sencadas, V. *et al.*: The piezoresistive effect in polypropylene-carbon nanofibre composites obtained by shear extrusion, Smart Materials and Structures 19:065013, (2010).
- [51] Connor, M.T., Roy, S., Ezquerra, T.A., Balta-Calleja, F.J.: Broadband AC conductivity of conductor-polymer composites. Phys Rev B: Condens Matter Mater Phys, 57, 2286–2294 (1998).
- [52] Böger, L., Wichmann, M.H., Meyer, L.O. and Schulte, K.: Load and health monitoring in glass fibre reinforced composites with an electrically conductive nanocomposite epoxy matrix, Compos Sci Technol, 68, 1886–1894 (2008).
- [53] Costa, P., Ferreira, A., Sencadas, V., Viana, J.C. and Lanceros-Méndez S.: Electro-mechanical properties of triblock copolymer styrene-butadiene-styrene/carbon nanotube composites for large deformation sensor applications. Sensor Actuat A-Phys, 201, 458–467 (2013).
- [54] de Saint-Venant, A.J.C.B.: Mémoire sur la flexion des prismes, J. Math. Liouville 1, 89–189 (1856).
- [55] Guadagno, L., Vietri, U., Raimondo, M., Vertuccio, L., Barra, G., De Vivo, B. *et al.*: Correlation between electrical conductivity and manufacturing processes of nanofilled carbon fiber reinforced composites, Composites Part B, 80, 7–14 (2015).

- [56]Thostenson, E.T., Ren, Z. and Chou, T-W.: Advances in the science and technology of carbon nanotubes and their composites: a review, *Compos Sci Technol*, 61(13), 1899–912 (2001).
- [57]Hu, N., Itoi, T., Akagi, T., Kojima, T., Xue, J., Yan, C. *et al.*: Ultrasensitive strain sensors made from metal-coated carbon nanofiller/epoxy composites, *Carbon*, 51, 202–12 (2013).

Afterword

Morphing aircraft can change their external shape substantially to adapt to a changing mission environment during flight. The challenge of adaptive systems in the future will mainly be to convince industry that this kind of technology can bring real advantages in terms of enhanced aerodynamic performance, lower installation impact respect to traditional control surface systems, reduced weight, and equivalent safety level. H2020 represents of course the most ambitious research and innovation programme ever undertaken by EU which may stimulate closer relations among leading industries, research centres and universities. Nowadays, the academia has to reply a new much more challenging task: to keep producing new concepts for the technology of the future. The research projects in which the author was involved since his first year of Ph.D. programme were an excellent source of training and study of innovative systems. The collaboration with international academia and leading industries (Leonardo Finmeccanica, CIRA, L'École de Technologie Supérieure, Canadian National Research Council, University of Bath, University of Salerno) has also allowed a fruitful exchange of ideas on the most ambitious research challenges. The thesis activity offers a modern overview at morphing wings technologies for large commercial aircraft facing issues on the industry design, real manufactured prototypes and certification. Practical applications of morphing devices are presented, from the challenge of conceptual design incorporating both actuation and sensing systems studies, to the most promising and potentially flyable solutions aimed at improving the aircraft performance. In the current context increasingly oriented towards the implementation of electro-mechanical actuators and integrated sensing methodologies as well, the manuscript addresses these aspects with focus on the adaptive systems. The work consists of five sections which contains current results on electro-mechanical systems evolution for morphing flap and a survey on the most significant achievements of distributed sensing systems for large strain monitoring in case of compliant segments.